

A CALCIUM PHOSPHATE IMPLANT WITH CONTROLLED MACROPOROSITY FOR ANTERIOR L5-S1 INTERBODY FUSION

THÈSE N° 2507 (2002)

PRÉSENTÉE À LA FACULTÉ STI SECTION DE GÉNIE MÉCANIQUE

ÉCOLE POLYTECHNIQUE FÉDÉRALE DE LAUSANNE

POUR L'OBTENTION DU GRADE DE DOCTEUR ÈS SCIENCES TECHNIQUES

PAR

Eric CHARRIÈRE

ingénieur en science des matériaux diplômé EPF
de nationalité suisse et originaire de Cerniat (FR)

acceptée sur proposition du jury:

Prof. Ph. Zysset, directeur de thèse
Prof. R. Giarodon, rapporteur
Prof. F. Lavaste, rapporteur
Dr J. Lemaître, rapporteur
Prof. P.-F. Leyvraz, rapporteur

Lausanne, EPFL
2002

REMERCIEMENTS

Une thèse est l'aboutissement d'un long chemin traversé de rencontres, de conseils et de collaborations. Mes pensées vont donc bien naturellement à toutes les personnes qui à un moment ou un autre m'ont incité à poursuivre dans cette voie, que ce soit des membres de ma famille, des amis, des professeurs, ou des collègues de travail.

Je tiens tout d'abord à remercier chaleureusement mon directeur de thèse, le Prof. Philippe Zysset, qui m'a dirigé avec brio, intelligence et persévérance durant quatre années. Ses connaissances scientifiques, sa faculté de synthèse, sa volonté d'aller toujours plus loin et son désir de plonger son esprit au fond des problèmes, m'ont permis de réaliser ce travail dans d'excellentes conditions, et m'ont évité de nombreux pièges auxquels je n'aurais peut-être pas pu faire face sans son soutien continu.

Au moment de rendre la version finale du présent mémoire, je tiens aussi à remercier mes rapporteurs, le Prof. François Lavaste de l'ENSAM à Paris, le Prof. Rémy Glardon de l'ICAP à l'EPFL, le Prof. Pierre-François Leyvraz de l'HOSR, ainsi que le Dr Jacques Lemaître du LTP à l'EPFL. Je tiens aussi à remercier le Prof. Jacques Giovanola pour sa tâche de président du jury.

Je voudrais dans ces remerciements rendre aussi hommage à mes *pauvres* étudiants de diplôme, Christian Pichonnat, Miguel Caride et Fabrice Sirey, qui ont tous les trois réalisé un très bon travail. Merci à vous pour votre intelligence, joie et bonne humeur.

Je tiens bien sûr à remercier mon employeur, l'Hôpital Orthopédique de la Suisse Romande (HOSR), instigateur de ce projet. Mes pensées vont plus particulièrement au Dr Philippe Mordasini qui a été rattaché à ce projet, et qui tout au long de cette thèse m'a aidé à résoudre des problèmes médicaux, allant du prélèvement sur cadavre de rachis lombaires jusqu'à la collection de clichés radiographiques. Je tiens aussi à remercier le Prof. Pierre-François Leyvraz, le Prof. Michel Dutoit, le Dr Pascal Rubin, le Dr Dominique Pioletti ainsi que le service de radiologie pour l'aide qu'ils ont pu m'apporter durant ce travail.

Merci aussi à tous les membres du LMAF de l'EPFL, et plus particulièrement Stefan Hengsberger et Liliana Rincon du *bonegroup* de notre laboratoire, qui ont toujours été disponibles pour m'aider. Je tiens à remercier le Prof. John Botsis pour m'avoir accueilli dans son laboratoire. Un grand merci aussi au personnel de l'ICAP, et plus particulièrement Ian Stroud, Philippe Grize, Nakis Karapatis et Olivier Durussel pour leur aide durant cette thèse. Un grand merci aussi à l'équipe de l'atelier dirigé par Gino Crivellari qui a réalisé un excellent travail.

Mes pensées vont aussi à toutes les personnes extérieures du laboratoire qui m'ont aidé un jour ou l'autre: Christian Pittet, Stéphane Terrazzoni, Carlos Morais, le Dr Jacques Lemaître du LTP à l'EPFL ; Thomas Beutler et la Dr Tracy Orr de l'institut de biomécanique Maurice E. Müller à Berne, et Prof.. S.J. Hollister de l'université de Michigan pour l'utilisation de son logiciel d'homogénéisation.

Merci aussi à Philip Pattis, pour sa relecture d'une partie de ce travail.

Finalement un grand merci à ma famille, mes amis et à Agnès, qui m'ont pleinement soutenu tout au long de ce travail et plus particulièrement durant les derniers mois de rédaction.

Merci à vous tous et à ceux que, par mégarde, j'aurais oubliés.

VERSION ABRÉGÉE

A l'heure actuelle, aux Etats-Unis, environ 50 millions de personnes souffrent de lombalgie. Il s'agit du problème médical le plus important et le plus coûteux pour la santé publique des personnes âgées entre 20 et 50 ans. Les causes de ces douleurs peuvent être nombreuses. Par exemple, une hernie du disque ou une sténose peuvent entraver les fibres nerveuses du rachis. Des processus dégénératifs affectant les facettes articulaires ou une spondylolisthesis peuvent engendrer des instabilités de certains segments du rachis. Bien que la majorité des patients soit soignée à l'aide de traitements conservateurs tels que la médication et la physiothérapie, il en subsiste un certain nombre qui nécessitent une chirurgie rachidienne.

Différentes techniques comme par exemple les fusions postérieure, postérolatérale et intervertébrale permettent de stabiliser les segments affectés. Des vis et tiges en alliage de titane peuvent être utilisées pour les fusions postérieures et postérolatérales, ceci avec ou sans adjonction de greffe osseuse. Des cages métalliques peuvent également être employées pour une fusion intervertébrale lombaire postérieure (PLIF) ou pour une fusion intervertébrale lombaire antérieure (ALIF). En général, des greffes osseuses prélevées sur la crête iliaque sont insérées dans ces cages afin de permettre une recolonisation osseuse à l'intérieur de l'implant. Le défaut majeur de ces cages est leur composition métallique, avec tous les problèmes et risques que cela comporte.

Il semble donc important de palier aux désavantages de ces cages en concevant un nouvel implant de type ALIF. L'objectif principal de cette thèse est de développer un implant qui peut à la fois remplacer la cage métallique et la greffe osseuse. Ce matériau doit être biocompatible, biorésorbable, ostéoinducteur et suffisamment résistant pour supporter les contraintes locales élevées. L'implant conçu avec ce type de biomatériau doit aussi être macroporeux afin de permettre aux cellules osseuses et aux vaisseaux sanguins de le coloniser rapidement. Si un tel implant peut être fabriqué, il ne sera alors plus nécessaire de prélever de greffes osseuses. De plus, cet implant disparaîtra avec le temps, permettant à l'os formé de le remplacer complètement et donc d'assurer une fusion complète entre les deux corps vertébraux. Afin d'adresser ce problème, cinq études ont été réalisées :

- Une étude anthropométrique du segment L5-S1 et de l'espace à disposition pour l'insertion d'un implant de type ALIF (Chapitre 2).
- Une caractérisation mécanique complète de deux ciments phosphocalciques (Chapitre 3).

- Une nouvelle méthode de fabrication de structures d'hydroxyapatite à porosité contrôlée (Chapitre 4).
- Une comparaison entre un système non contraint et semi contraint, permettant la caractérisation *in vitro* de la complaisance de l'unité fonctionnelle du rachis L5-S1 (Chapitre 5).
- Une étude numérique utilisant un modèle par élément fini du segment L5-S1 ainsi que sa validation expérimentale (Chapitre 6).

La première étude a permis de définir et de quantifier tous les paramètres géométriques nécessaires à la conception d'un implant de type ALIF (Chapitre 2). Des essais de traction, compression et torsion, ainsi que l'utilisation d'un modèle d'élasticité linéaire par cône et d'un critère de résistance multiaxiale de Tsai-Wu ont permis de publier une caractérisation mécanique exhaustive de ciments brushite et hydroxyapatite (Chapitre 3). Une nouvelle méthode de fabrication de ciments d'hydroxyapatite à porosité et à élasticité contrôlée a été développée. Comme ce type de ciment est biocompatible, biodégradable et ostéoconducteur, la structure d'hydroxyapatite à macroporosité contrôlée représente un matériau de choix pour la reconstruction osseuse dans des zones à contraintes élevées compressives (Chapitre 4). La mesure et la comparaison de la complaisance (ou souplesse) de segments rachidiens intacts ou instrumentés au moyen de systèmes de caractérisations mécaniques doivent être effectuées avec précaution. Contraindre les segments rachidiens dans certaines directions modifie la complaisance de ceux-ci, particulièrement en rotation axiale et en flexion latérale (Chapitre 5). Un modèle par élément fini de l'unité fonctionnelle L5-S1 a été développé. Pour les trois types de mouvement principaux une grande similitude a été trouvée entre les complaisances obtenues numériquement et expérimentalement (Chapitre 6).

Se basant sur les résultats numériques obtenus sur un segment dans lequel un nouvel implant de type ALIF en ciment phosphocalcique macroporeux est inséré, deux applications sont envisagées (Chapitre 7). Premièrement, la structure d'hydroxyapatite à macroporosité contrôlée peut être utilisée comme implant de type ALIF, mais à condition qu'une stabilisation postérieure soit effectuée. Les avantages principaux obtenus grâce à ce procédé sont qu'il n'est plus nécessaire de prélever de la greffe osseuse et d'insérer antérieurement un composant métallique. Deuxièmement, cette structure macroporeuse peut aussi être utilisée comme greffe osseuse et insérée dans une cage métallique flexible afin de favoriser la fusion du segment et d'éviter le prélèvement d'un greffon.

ABSTRACT

In the United States approximately 50 million people suffer from low back pain. In the 20-50 years age group, this is the most important and expensive health care problem. The causes of low back pain are various. A herniated disk or spinal stenosis may trap nerve roots exiting the spinal column. Spondylolisthesis or degenerative disorders affecting the facet joints may cause some spinal units to become unstable. Although the majority of patients suffering back pain respond well to conservative treatments such as medication and physical therapy, a fraction of them will require spinal surgery.

Different methods of stabilization exist, such as posterior, posterolateral and interbody fusion. Titanium screws and rods can be used for a posterior or posterolateral stabilization, with or without bone graft. Metallic cages or screws can also be used for a posterior lumbar interbody fusion (PLIF) or an anterior lumbar interbody fusion (ALIF), with or without bone graft inside the implant. A common drawback and risks to all of these implants is that they are made out of metal, with all the potential problems engendered by these materials.

The present dissertation work aims at designing an improved anterior lumbar interbody fusion (ALIF) implant for the L5-S1 segment. The global objective of this thesis is to develop an alternative biomaterial that can replace at the same time the metallic cage and the bone graft. It must be biocompatible, bioresorbable, osteoinductive and strong enough to resist the high local stresses. The implant made of this biomaterial should also present an appropriate macroporosity to allow the blood vessels and bone cells to colonize quickly the implant. The implant should then be degraded in a controlled fashion by fragmenting over a defined period of time and releasing non-toxic ions which can be metabolized or excreted by the body. If this could be achieved, then no more graft would be necessary and the synthetic material would disappear with time allowing a complete bone fusion. In order to find an answer to this problem, five studies were defined:

- An anthropometric study of L5-S1 and the available space for insertion of an implant (Chapter 2).
- A complete mechanical characterization of two different phosphocalcic cements (Chapter 3).
- A new method to manufacture hydroxyapatite scaffolds with controlled porosity (Chapter 4).
- A comparison between an unconstrained and a partially constrained system for *in vitro* biomechanical testing of the L5-S1 functional spinal unit (Chapter 5).

- A numerical study using a finite element model of the L5-S1 functional spinal unit, validated with experimental data (Chapter 6).

Our study provides the necessary geometrical parameters for the design of an ALIF cage to treat patients with low back pain (Chapter 2). Compression, tension and torsion tests together with the use of a conewise linear elasticity model and a Tsai-Wu failure criterion provide an exhaustive characterization of both elastic and failure properties of a brushite and a hydroxyapatite cement (Chapter 3). A new method to manufacture hydroxyapatite scaffolds with controlled porosity and predictable elastic properties is developed. Since precipitated hydroxyapatite cements are biocompatible, biodegradable and osteoconductive, the manufactured scaffold represents a biomaterial of choice for bone reconstruction in weight bearing areas dominated by compressive stresses (Chapter 4). According to our findings, particular care should be given when quantifying and comparing the kinematics and the flexibility curves of the intact or instrumented spine with experimental set-ups of various degrees of constraints for axial rotation and to an even larger extent for lateral bending (Chapter 5). A three-dimensional finite element model of the L5-S1 FSU is presented. The kinematics of the segment is found to be similar between numerical and experimental results for all major motions (Chapter 6).

Following the application of the numerical model to the developed ALIF implant with or without posterior stabilisation, two applications for lumbar fusion are envisaged (Chapter 7). First, this macroporous scaffold can be used as an ALIF implant in conjunction with a posterior stabilization. Main advantages compared to current solutions are that no more bone graft is necessary and that no more metal is inserted anteriorly. Second, this macroporous scaffold can be used as a bone graft material, which can be inserted in a metallic cage of sufficient elasticity.

TABLE OF CONTENTS

CHAPTER 1 : GENERAL INTRODUCTION	1
LOW BACK PAIN	2
DIAGNOSIS AND SURGICAL TREATMENT FROM POSTERIOR TO ANTERIOR FUSION.....	3
CURRENT ALIF IMPLANTS AND BIODEGRADABLE MATERIALS	6
OBJECTIVES AND ORGANIZATION OF CHAPTERS.....	8
REFERENCES	11
CHAPTER 2 : ANATOMY AND ANTHROPOMETRY OF THE LUMBO-SACRAL SEGMENT: AN ESTIMATION OF THE AVAILABLE SPACE FOR THE INSERTION OF A FUSION CAGE	13
ANATOMY OF THE LUMBO-SACRAL SPINE	14
<i>The lumbar vertebrae</i>	15
<i>The sacrum</i>	16
<i>The intervertebral joints</i>	17
<i>The intervertebral disk</i>	18
<i>The ligaments</i>	19
INTRODUCTION OF THE ANTHROPOMETRY STUDY	21
MATERIAL AND METHODS.....	21
<i>Study population</i>	21
<i>Measuring methods</i>	22
<i>Statistical analysis</i>	25
RESULTS	25
DISCUSSION	27
REFERENCES	31
CHAPTER 3 : EXHAUSTIVE MECHANICAL CHARACTERIZATION OF BRUSHITE AND HYDROXYAPATITE CEMENTS.....	33
INTRODUCTION	34
<i>Elasticity</i>	34
<i>Failure models</i>	35
MATERIALS AND METHODS.....	36
<i>Brushite</i>	36
<i>Hydroxyapatite</i>	37
<i>Mechanical tests</i>	39
RESULTS	39
<i>Elasticity</i>	39
<i>Failure</i>	42
DISCUSSION	42
<i>Elasticity</i>	42

<i>Failure</i>	44
CONCLUSIONS.....	47
REFERENCES.....	48
CHAPTER 4 : HYDROXYAPATITE CEMENT SCAFFOLDS WITH CONTROLLED MACROPOROSITY: FABRICATION PROTOCOL AND MECHANICAL PROPERTIES.....	51
INTRODUCTION.....	52
MATERIALS AND METHODS.....	53
<i>Design of the negative macroporosity</i>	53
<i>Manufacturing</i>	54
<i>Mechanical tests</i>	56
<i>Homogenization</i>	57
RESULTS.....	59
<i>Manufacturing</i>	59
<i>Mechanical tests</i>	59
<i>Homogenization</i>	60
DISCUSSION.....	62
REFERENCES.....	66
CHAPTER 5 : COMPLIANCE OF THE L5-S1 SPINAL UNIT: A COMPARATIVE STUDY BETWEEN AN UNCONSTRAINED AND A SEMI-CONSTRAINED SYSTEM.....	69
INTRODUCTION.....	70
MATERIALS AND METHODS.....	71
<i>Angle decomposition</i>	72
<i>Instantaneous axis of rotation</i>	73
<i>Statistical analysis</i>	74
RESULTS.....	74
DISCUSSION.....	78
REFERENCES.....	81
CHAPTER 6 : A FINITE ELEMENT MODEL OF THE L5-S1 FUNCTIONAL SPINAL UNIT: DEVELOPMENT AND COMPARISON WITH BIOMECHANICAL TESTS <i>IN VITRO</i>.....	83
INTRODUCTION.....	84
MATERIALS AND METHODS.....	85
RESULTS.....	93
DISCUSSION.....	101
REFERENCES.....	105
CHAPTER 7 : GENERAL CONCLUSION.....	107
CURRICULUM VITAE.....	117

ABSTRACT

This chapter introduces the clinical problem of low back pain, the current treatments and an alternative to these treatments that will be studied in this thesis. First, the history and epidemiology of low back pain is recalled. One of the surgical treatments to this increasingly important health problem is lumbar fusion. Clinical diagnosis and choice of the appropriate procedure are reviewed with a special emphasis on anterior lumbar interbody fusion (ALIF). Titanium alloys or stainless steels are the current materials for ALIF cages. As these metallic implants present numerous drawbacks, new degradable biomaterials developed to overcome these limitations are presented. Finally, the potential of a new macroporous hydroxyapatite scaffold for ALIF at the L5-S1 level is motivated and the objectives of the present work are stated.

LOW BACK PAIN

Back pain was first identified and described in an Egyptian manuscript, dated about 2500 BC¹. Later, Hippocrates introduced the term “sciatica”, but it was only later in the Roman age that authors, like Soranus and Caelius Aurelianus, defined sciatica¹. Although they described different types of back pain, no anatomical explanation and contributions to the pathogenesis of low back pain were made until the work of Cotugno, Von Luschka, Lasègue, Oppenheim, Babinski, Virchow and Kocher in the 18th and 19th century¹. The first reasonable explanation of low back pain appeared only at the beginning of the 20th century, when Mixter and Barr assigned prolapse of the intervertebral disk as the etiologic factor of the symptoms². In the late forties, Steinler³ highlighted the relation between degeneration of the intervertebral disk and low back pain. Since that observation, the effect of disk degeneration on low back pain was studied extensively, but it is quite remarkable that until today, no single factor could be identified.

In the United States approximately 50 million people suffer from back pain. In the 20-50 years age group, this is the most important and expensive health care problem^{4,5}. The major costs of low back pain are associated with chronic disabling low back pain. Approximately 5.2 million persons are disabled by low back pain, 50% of them permanently^{6,7}. The total estimated costs attributed to low back pain in the United States are between \$16-\$50 billion and at least 85 % of these costs are related to recurrent or chronic disability (1986)^{8,9,10,11}. Compared with other health conditions, low back pain is also costly in terms of earning losses and productivity losses¹². Van Tulder et al.¹³ estimated the costs of back pain to society in The Netherlands to be 1.7 % of the gross national product (GNP) in 1991. The total direct medical costs were estimated at \$367.6 million and the total indirect costs (result from productivity losses) for the entire labor force at \$4.6 billion.

The major causes of low back pain are various. A herniated disk or spinal stenosis may trap nerve roots exiting the spinal column. Spondylolisthesis or degenerative disorders affecting the facet joints may cause the spine to become unstable. To help diagnose these disorders, X-rays, computed tomography (CT) and magnetic resonance imaging (MRI) are commonly performed. Most low back pain can be effectively managed with a variety of interventions. Exercise, physical therapy, weight loss, smoking cessation, chiropractic treatment, steroid injections and traction are just a few examples of conventional treatment that may improve back pain. Although the majority of patients suffering back pain respond well to conservative treatment such as medication and physical therapy, a small fraction of

them will require spine surgery. If a patient with serious, long-term low back pain is not relieved by conservative programs, a surgical procedure may be considered.

It is believed that pain originates in levels of the spine where the vertebrae are slipped (spondylolisthesis) or the disks or joints are damaged. This may be due to irritated nerve endings around the disk, bone or joints themselves or due to actual entrapment of the spinal nerves in that region. Other circumstances such as a recurrent disk herniation, scoliosis, or severe disk degeneration exist in which a fusion may best treat the source of back and leg pain. By eliminating motion across the damaged level, pain can be attenuated. A solid bridge of mature bone eliminates motion that normally would take place at the disk space and in the joints of the spine. This bridge is called *fusion* and will be described further in the next section.

DIAGNOSIS AND SURGICAL TREATMENT FROM POSTERIOR TO ANTERIOR FUSION

Before considering a surgical intervention, the radiological assessment is composed of a face and profile radiography of the lumbar column carried out in an upright position. Radiographies of the profile lumbar column in hyperflexion and hyperextension also inform about the relative mobility of the various articulations. Sometimes a CT is also performed to look at the bone density and to have precise measurements of the bony structures. Finally, MRI may be done, the images of which allowing an estimation of the disk and adjacent endplate conditions, the level of the vascular junction and dimensions of the vertebrae.

Different methods of stabilization exist, such as posterior, posterolateral and interbody fusion. Titanium screws and rods can be used for a posterior or posterolateral stabilization, with or without bone graft. Metallic cages or screws can also be used for a posterior lumbar interbody fusion (PLIF) or an anterior lumbar interbody fusion (ALIF), with or without bone graft inside the implant.

The **posterior stabilization** uses titanium alloys or stainless steel screws and rods. These screws are typically placed through the "pedicles" of the vertebrae. They are attached to a rod or plate that is contoured to the spine (Figure 1). This type of spinal "instrumentation" provides immediate stability and strength to the spine.

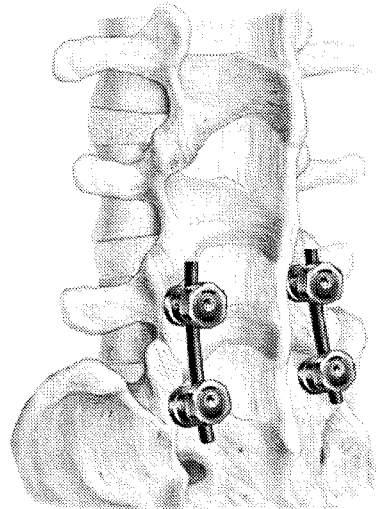


Figure 1 : L5-S1 posterior fixation using rods and pedicular screws (from www.spineuniversity.com).

Other techniques involve placement of bone marrow or "graft" along the sides of the spine (with or without screws). This is called a **posterolateral fusion** and is another way to fuse a level of the lumbar spine. The source of the bone graft material in the pelvis (ilium) can remain painful for weeks or months following surgery.

In other situations, fibula and iliac struts, femoral rings and dowel, as well as synthetic metallic devices have been applied as fixation implements to aid in lumbar interbody fusion. This is called an **interbody fusion** because the device is located between the "bodies" of the vertebral bones and is across the diseased disk space. This can be done from the front (anterior) or from the back (posterior). An anterior lumbar interbody fusion (ALIF) implant is inserted anteriorly, whereas a posterior lumbar interbody fusion (PLIF) device is inserted posteriorly.

The **PLIF approach** is invasive and muscles are scarred during this surgical procedure. After the spine is apparent, the lamina is removed (laminectomy) which allows visualization of the nerve roots. The facet joints, which are directly over the nerve roots, may then be undercut (trimmed) to give the nerve roots more room. The nerve roots are then retracted to one side and the disk space is cleaned of the disk material. A bone graft, or interbody cages with bone, is then inserted into the disk space. The PLIF approach has an advantage over the posterolateral fusion in that the large spinal muscles do not need to be dissected off the transverse processes, so there is less scarring of the muscle and associated pain for the patient. However, the PLIF also has a couple of disadvantages:

- Substantial retraction of the nerve roots is necessary for the surgeon to gain access to the disk space. Significant traction can injure the nerve root and has the potential to result in

chronic leg pain and back pain. The pain associated with this type of nerve root injury can be severe, and there are no effective options for treatment.

- There are numerous veins (epidural veins) over the disk space, and surgery in this area creates the potential for excessive blood loss during the surgery.

To overcome these drawbacks, an **ALIF approach** may be preferable. The anterior approach through the abdomen may be done "laparoscopically" with several small incisions (minimally-invasive) or "open" through a single incision (less-invasive). The bone graft serves as a source of bone cells to help initiate the fusion process at the surgical site. Bone grafts are often used in conjunction with a metallic device that provides initial strength and rigidity of the segment. In some circumstances, cages may be used with pedicle screws and rods to obtain a better stabilization (Figure 2).

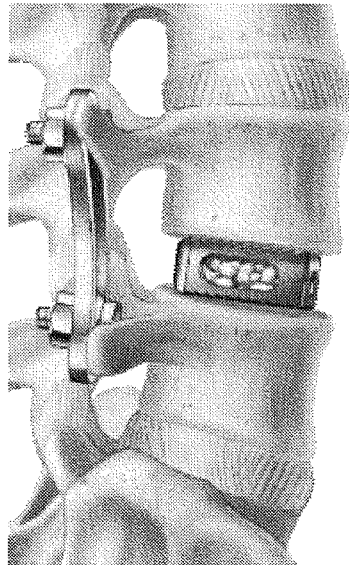


Figure 2 : Anterior and posterior stabilization with pedicle screws, rods and a cage (from www.spineuniversity.com).

Anterior Lumbar Interbody Fusion (ALIF) is a valuable surgical tool for enlarging the disk space and neural foramen, to open the space for the nerves, and to reduce spinal deformities. This technique has the advantage of preserving the posterior supporting elements of the spine, keeping intact the thick paraspinal muscles, the posterior bone and ligaments that stabilize the spine, and avoids retraction of the nerves. Transperitoneal exposures (i.e., through the peritoneum) require incision of both the anterior and posterior peritoneum. In contrast, retroperitoneal exposures maintain the integrity of the peritoneum and approach the spinal column laterally behind the bowel and peritoneal contents. This has the advantage of producing less post-operative bowel problems.

ALIF works well for degenerative disk disease without spondylolisthesis. It acts by opening up the narrowed neural foramen (bony openings for the nerve roots), and stabilizing

the vertebrae adjacent to the disk space. However, if spinal instability (spondylolisthesis or slippage of the vertebrae) or spinal deformity (scoliosis) are present, then supplemental spinal instrumentation with screws or hooks and rods may be needed to rigidly immobilize the loose vertebrae.

ALIF should not be used as a stand-alone technique if the patient's bone is very soft (osteoporosis) because the spacers may sink into the softened adjacent bone or the spacers will loosen and not maintain adequate height. Additionally, if the ligaments are torn or loose between two vertebrae (as is seen with spondylolisthesis) then shearing forces may be generated that cause displacement and failure of the interbody spacers. These cases may require pedicle screws or other spinal instrumentation to reinforce the fixation to allow the fusion to heal properly without complications.

The process of healing a fusion can take many months or well a year to be complete. A fusion is not a quick fix; it is rather a commitment of patient and surgeon to a long process of improving back and leg pain. Hundred percent cures are rare. Realistically, patients can expect a dramatic and lasting improvement in their back and leg pain. The success rates of lumbar fusion can be lower in patients who smoke, are overweight, suffer from diabetes, have osteoporosis, or who have had radiation treatment that included the lower back. Good nutrition and slowly increasing activity in the healing period can help achieve successful recovery.

CURRENT ALIF IMPLANTS AND BIODEGRADABLE MATERIALS

Nowadays, a lot of different designs of commercialized ALIF cages exist. Some look like hollow screws (ScrewCage™, BAK™, ...) whilst others look like cages (SynCage™, Stabilis™ ...). They are all made out of titanium or stainless steel alloys. All of these implants can restore the height of the intervertebral disk, stabilize the functional unit of the spine and integrate bone graft inside their metallic structure. This bone graft, often harvested from the iliac crest, should allow a recolonization of the implant with vessels and bone cells. New bone can therefore be formed inside the implant. These implants stabilize well the motion of the functional spinal unit in flexion and lateral bending. Without a posterior stabilization, the extension is not significantly reduced¹⁴.

A common drawback to all of these implants is that they are made of metal. These metallic implants are very rigid and support the entire applied load. The bone graft is thus protected and does not "feel" so much stress. This is called the "stress-shielding" effect. The bone graft is resorbed and only some fibrous tissue replaces it. Thus, the long-term

stabilization of the implant may not be achieved and fusion may not occur. The rigidity of these structures is so high compared with bone, that the implants may also break the endplates, penetrate into the vertebral body and crush the cancellous bone. Another problem is that stand-alone cage constructions reduce range of motion (ROM) effectively, but the residual ROM indicates the presence of micromotion at the cage-endplate interface¹⁵. This micromotion can produce small metallic particles, which are suspected to provoke an inflammatory reaction in some patients.

The numerous problems encountered with metallic cages are a motivation to change the materials from which these implants are made and to try optimizing the contact surface between the two endplates and the implant. The design of metallic interbody implants has already changed from screw cages to larger cages that maximize the contact area (e.g. SyncageTM, Figure 3). A recent option is to replace the inserted bone graft with a macroporous synthetic degradable scaffold.

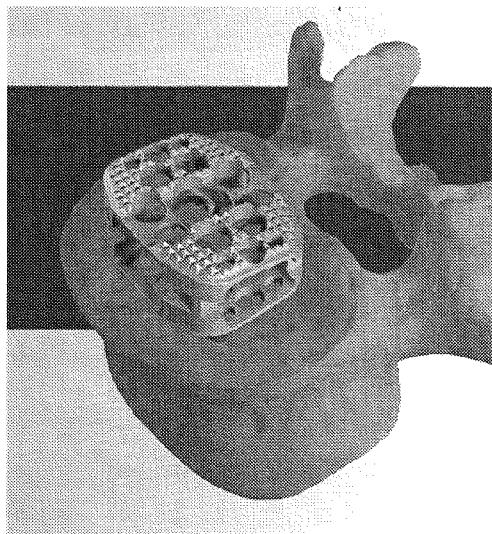


Figure 3 : This new implant, called SyncageTM, possesses a greater contact zone with the endplate than other systems (from Mathys AG).

Currently, knowledge in the fields of biomechanics, materials science and medicine provide a number of principles aimed at understanding in a more scientific manner, the mechanical and physiological interactions of an implant with its environment.

Calcium phosphate ceramics represent without a doubt a group of biomaterials suited to intraosseous implantation. Indeed, over the last ten years, many *in vivo* and *in vitro* studies were conducted and no toxicity problem was ever been reported with implants in hydroxyapatite (Hap) or β -tricalcium phosphate (β -TCP). This excellent biocompatibility is most probably due to the great similarity between the chemical composition of the mineral

part of bone and that of the implant; a compact bone presents a Ca/P ratio of 1.61; it is 1.67 for HAP and 1.50 for TCP^{16,17}.

Hydroxyapatite and some calcium phosphates are known to be intrinsically osteoinductive. They could induce bone formation in an extraskelatal site without the "artificial" presence of osteogenic cells or bone morphogenic proteins (BMP)¹⁸. Moreover, a remarkable property of these materials is that the tissue thus formed is directly bonded to the implant without the presence a fibrous fabric layer. Macropores are also essential in these cements and their interconnections allow for an early vascularization. This stage is essential to the osseous reformation and is only possible if some blood vessels can penetrate the implant, in order to bring the necessary nutriments for cell function.

Towards the end of the Eighties, the majority of the research conducted in this field was related to a synergy between different parameters, that are to be taken into account¹⁹: 1) Size of the powder particles 2) Shape of the particles 3) Size of the pores 4) Shape of the pores 5) Pore size distribution + interconnections 6) Specific surface area 7) Phases 8) Crystal structure 9) Crystals size 10) Grains size 11) Density 12) "Coating" thickness if on metal substrate 14) Hardness 15) Surface roughness 16) Sintering temperature, if sintered (it influences part of the parameters above) 17) Animal model 18) Implantation site.

All these properties will not be discussed here, but they show however the difficulty of determining the optimal characteristics of an implant. Indeed, it is almost impossible to univocally relate a specific effect to a given parameter. Nevertheless, the studies carried out until this day give a certain number of guidelines; let us quote for example the pores size: it should not be under 100µm if osteogenesis is to be expected²⁰.

OBJECTIVES AND ORGANIZATION OF CHAPTERS

The objective of this thesis is to develop and evaluate an alternative to metallic ALIF cages and bone graft. The implant should be biocompatible, bioresorbable, osteoinductive and strong enough to support the high local stresses. The implant should also present an appropriate macroporosity to allow the blood vessels and bone cells to colonize quickly the implant. During this bone formation inside the macroporosity, the implant should degrade in a controlled fashion by fragmenting over a defined period of time and releasing non-toxic ions which can be metabolized or excreted by the body. If this could be achieved, the macroporous implant will be completely replaced by mature bone, fusing the two vertebrae together. The development and evaluation of such an implant has led us to divide the global work into five different studies. Figure 4 summarizes the organization of the chapters of this thesis.

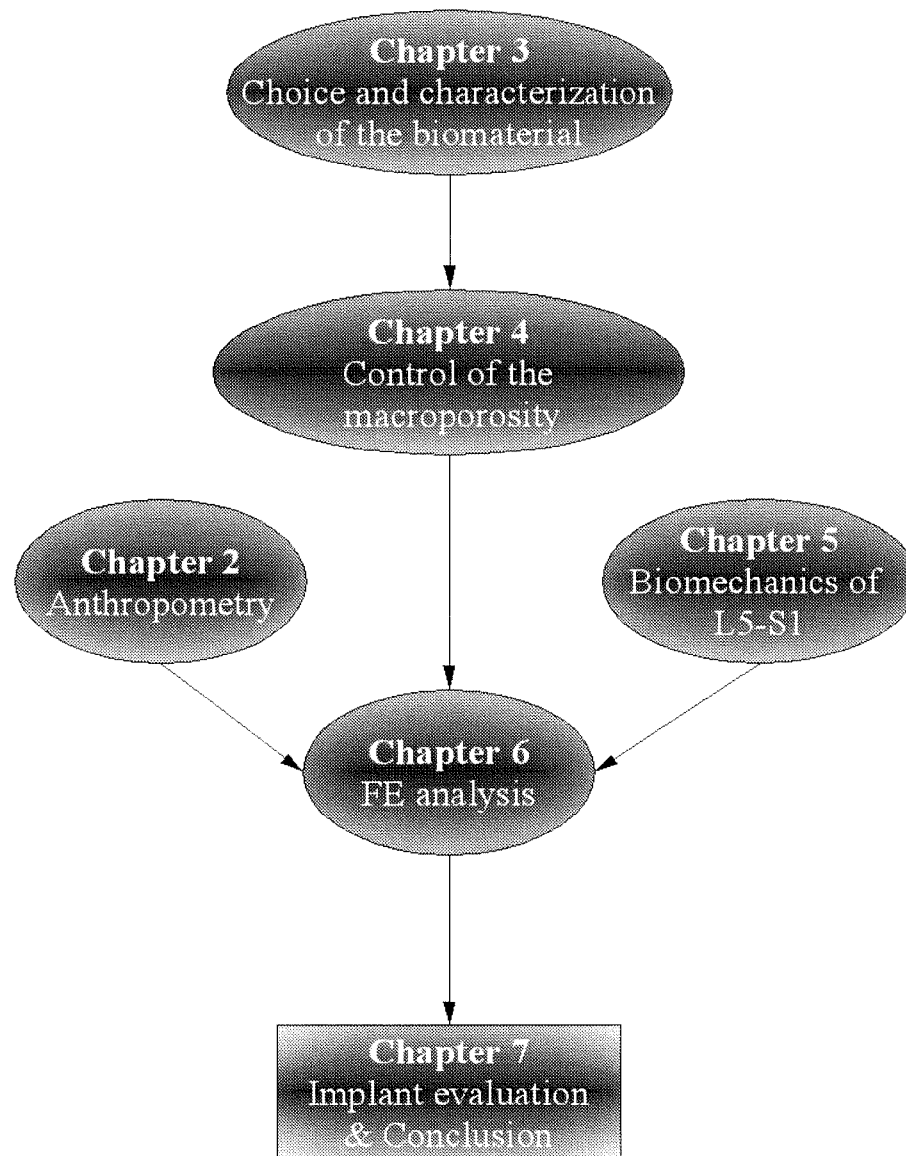


Figure 4 : Organizational chart of this thesis.

In order to design an improved anterior lumbar interbody fusion (ALIF) cage for the L5-S1 segment, detailed anatomy, accurate shape and dimensions of the vertebral body and intervertebral disk are needed. No previous study has reported all the required parameters. Thus, **Chapter 2** will describe the anatomy of the L5-S1 spinal segment and present a limited anthropometric study.

Two calcium phosphate cements, brushite and hydroxyapatite, were recently developed as bone substitution materials in orthopedic surgery. The brushite cement is biocompatible, resorbable, osteoconductive and injectable since it hardens in physiological conditions. In contrast, hydroxyapatite cement is less resorbable and not injectable. However, hydroxyapatite seems to offer a higher strength, which may open the perspective for its use in weight-bearing regions of the skeleton subjected to high multiaxial stresses. **Chapter 3**

reports an extended characterization of the elastic and failure properties of these two cements in moist condition.

Macroscopic porosity in bone substitution materials allows for early colonization of osteoprogenitor cells and diffusion of nutrients. In previous investigations, a few methods were proposed to induce large pores in bone substitution materials, such as solvent casting and particulate leaching techniques. However, these methods do not allow an accurate control of pore shape and orientation and are therefore deleterious to the implant mechanical properties. In order to overcome these limitations, a combined solid freeform fabrication and molding technique is proposed to manufacture macroporous calcium phosphate cements with controlled elastic properties. In **Chapter 4**, this method and an extended characterization of the elastic and failure properties of these samples in moist condition are presented. Furthermore, a homogenization model is used to predict the effective elastic constants of these scaffolds.

Biomechanical testing of functional spinal units (FSUs) is used extensively to quantify the compliance of the intact and instrumented human spines. Although a fully unconstrained system is considered as the “gold standard”, it remains unclear how the mechanical behavior is affected by the introduction of the limited number of constraints associated with multiple degrees of freedom (DOF) servohydraulic testing systems. There is also a long lasting controversy regarding the choice of the system to reproduce the physiological behavior of an FSU for biomechanical tests. Two different ways of characterizing the compliance of the L5-S1 were analyzed and are presented in **Chapter 5**.

The main objective of **Chapter 6** is to develop a new three-dimensional model of a L5-S1 segment able to simulate its passive mobility measured *in vitro*. The partial objectives are creation of a three-dimensional model of the L5-S1 FSU based on images obtained by quantitative computed tomography. A straight comparison with the experimental results for the three major movements is conducted. Evaluation of the local contact zone position at the facet joints is evaluated for different motions. The compliance of these segments (obtained in chapter 5) is used to validate the finite element model of the L5-S1 segment.

A general conclusion (**Chapter 7**) summarizes the major results of the thesis. Furthermore, a finite element analysis is presented which computes the stresses in an interbody L5-S1 cage, made of the developed macroporous calcium phosphate cement.

REFERENCES

- 1 Latchaw JP jr. A historical note on sciatica. Ch 1 In: Hardy RW, ed. Lumbar Disk Disease. New York: Raven Press, 1982.
- 2 Mixter W, Barr J. Rupture of the intervertebral disk with involvement of the spinal canal. N Eng J Med 1934;211:210-214.
- 3 Steinler A. Analysis and differentiation of low back pain in relation to the disk factor. J Bone Joint Surg 1947;29:455.
- 4 Frymoyer JW. Epidemiology. Ch 3 In: Frymoyer JW, Gordon SL, eds. New Perspectives on Low Back Pain. Chicago, American Academy of Orthopaedic Surgeons, 1989.
- 5 Haber LD. Disabling effects of chronic disease and impairment. J Chronic Dis 1971;24:469-487.
- 6 Grazier KL, Holbrook TL, Kelsey JL, et al.. The Frequency of Occurrence, Impact, and Costs of Musculoskeletal Conditions in the United States. Chicago, American Academy of Orthopaedic Surgeons, 1984.
- 7 Snook SH, Jensen RC. Costs. In: Pope MH, Frymoyer JW, Andersson G, eds. Occupational Low Back Pain. New York: Praeger, 1984:115-121.
- 8 Andersson GBJ, Pope MH, Frymoyer JW. Epidemiology. In: Pope MH, Frymoyer JW, Andersson G, eds. Occupational Low Back Pain. New York: Praeger, 1984:101-114.
- 9 Frymoyer JW, Pope MH, Clements JH, et al. Risk factors in low back pain. An epidemiological survey. J Bone Joint Surg 1983;65A:213-218.
- 10 Spengler DM, Bigos SJ, Martin NA, et al. Back injuries in industry. A retrospective study. I. Overview and cost analysis. Spine 1986;11:241-245.
- 11 Sullivan JGB. Chronic pain management. In: Rothman RH, Simeone FA, eds. The Spine, Third Edition. Philadelphia: Saunders, 1992:1945-1998.
- 12 Deyo RA. Reducing work absenteeism and diagnostic costs for backache. In: Hadler NM, ed. Clinical Concepts in Regional Musculoskeletal Illness. Orlando: Grune & Stratton, 1987:22-50.
- 13 Tulder MW van, Koes BW, Bouter LM. A cost-of-illness study of back pain in The Netherlands. Pain 1995;62(2):233-40.
- 14 Oxland TR, Hoffer Z, Nydegger T, Rathonyi GC, Nolte LP. A comparative biomechanical investigation of anterior lumbar interbody cages: central and bilateral approaches. J Bone Joint Surg Am 2000;82(3):383-93.
- 15 Tsantrizos A, Andreou A, Aebi M, Steffen T. Biomechanical stability of five stand-alone anterior lumbar interbody fusion constructs. Eur Spine J 2000 Feb;9(1):14-22
- 16 Bühler DW. Biomechanical Aspects of Bone-Implant Interfaces in Orthopaedics. Diss. ETH N° 12412. 1997 ; 12.
- 17 Engin NO and Tas AC. Manufacture of Macroporous Calcium Hydroxyapatite Bioceramics. Journal of the European Ceramic Society 19 (1999). Elsevier Science Ltd ; 2569.
- 18 Yuan H et al. A preliminary study on osteoinduction of two kinds of calcium phosphate ceramics. Biomaterials 20 (1999). Elsevier Science Ltd ; 1799.
- 19 Ducheyne P, Beight J, Cuckler J, Evans B, Radin S. Effect of calcium phosphate coating characteristics on early post-operative bone tissue ingrowth. Biomaterials 1990;11(8):531-40.

-
- 20 Hulbert SF, Morrison SJ, Klawitter JJ. Tissue reaction to three ceramics of porous and non-porous structures. *J Biomed Mater Res* 1972;6(5):347-74.

**ANATOMY AND ANTHROPOMETRY OF THE
LUMBO-SACRAL SEGMENT: AN ESTIMATION
OF THE AVAILABLE SPACE FOR THE
INSERTION OF A FUSION CAGE****ABSTRACT**

In order to design an anterior lumbar interbody fusion (ALIF) cage for the lumbo-sacral segment (L5-S1), accurate and complete geometrical parameters of the vertebral body and of the intervertebral disk are necessary. No exhaustive study was found that provide all the required informations.

In the first section, the anatomy of the L5-S1 segment is described, including bones, intervertebral joints and ligaments. In the second section, an anthropometrical study is presented, where the objective is to determine all parameters that are needed to design ALIF cages inserted with a less-invasive technique. Measured parameters included the posterior intervertebral disk height, the middle intervertebral disk height, the anterior intervertebral disk height, the lower vertebral depth, the lower vertebral width, the upper vertebral depth, the upper vertebral width and the disk angle. This study was carried out on 30 patients and on 10 cadaveric specimens. Standard face and profile X-rays as well as CT scans were performed on both cadaveric and “living” spines. Four experimented spinal surgeons analyzed the X-ray films and draw on them the maximum available intervertebral disk volume that can be removed with a “less-invasive” technique.

Our study provides the necessary values for the design of an ALIF cage to treat patients with low back pain. Although the number of specimens is low compared to other studies, our data are representative of those found in other studies.

According to the surgeons, the largest possible cage (for its insertion with a “less-invasive” surgical procedure) should have a relative width compared to the endplate width of 66% and a relative depth of 73%, no matter what the sex of the patient is. The implant area which is in contact with the endplate should cover 60% of the total endplate area.

ANATOMY OF THE LUMBO-SACRAL SPINE

The lumbo-sacral functional unit is a part of the spine global structure and is the junction between the lumbar and sacral part of the spine (Figure 1). It is composed of the fifth lumbar vertebra (L5), the first sacral vertebra (S1), an intervertebral disk, two zygapophysial joints and a number of ligaments.

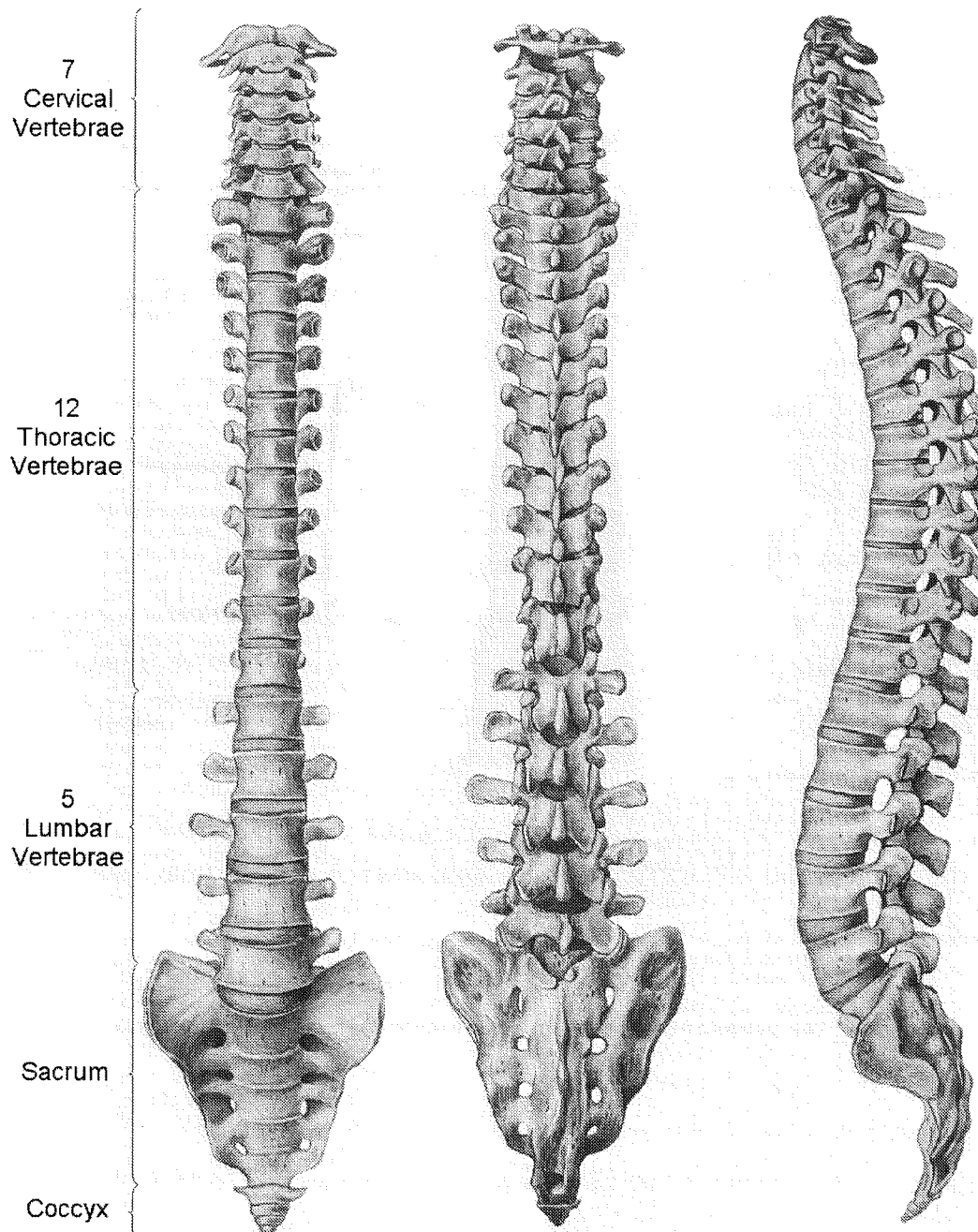


Figure 1 : Spine anatomy (anterior, posterior and left view). From Sobotta¹.

The lumbar vertebrae

The lumbar vertebra can be divided into three functional parts:

- the vertebral body
- the pedicles
- the posterior elements (spinous process, lamina, articular process, transverse process)

These different parts have unique functions but they act together in the integrated function of the whole vertebra (Figure 2).

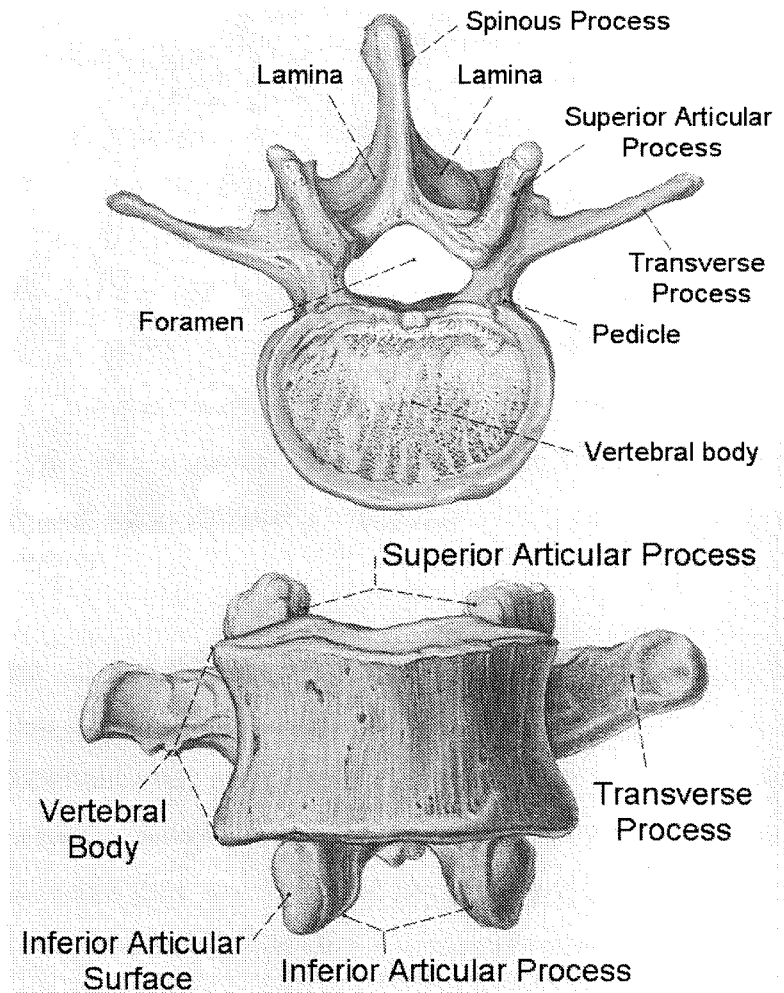


Figure 2 : Lumbar vertebrae: anatomy of the different parts (top and anterior view). From Sobotta¹..

The lumbar vertebral body

The vertebral body is a block of bone, designed for its axial weight-bearing purpose. Its internal structure consists of a cancellous bone with vertical and transverse trabeculae surrounded by a layer of cortical bone. The main advantages of having the trabecular internal structure over a solid bone block is the reduced weight of the vertebra, the ability of sustaining static as well as dynamic loads, and the possibility of being well supplied by the arteries and veins running through the intertrabecular space. The trabecular cavity of the

vertebral body filled with blood appears as a sponge. Although the weight-bearing capacity of the vertebral bodies is considerable, the vertebral bodies do not resist well to antero-posterior shear².

The pedicles

The pedicles function as a bridge between the vertebral body and the posterior elements. They transmit both tension and bending forces acting on the posterior elements of the vertebra to the vertebral body.

The posterior elements

The posterior elements of the vertebra consist of the articular processes, the spinous processes, and the laminae. The posterior elements are submitted to various forces acting on the vertebra. The inferior and superior articular processes, for example, resist forward sliding and twisting of the vertebral bodies. The spinous and transverse processes are also muscle-attachments and are therefore submitted to muscular forces acting on the vertebra. The laminae conduct forces from the spinous and articular processes to the vertebral body resulting in movement and providing stability. The laminae have, in addition to the conduction of forces, a protective function of the neural contents of the vertebral canal.

The sacrum

The sacrum (Figure 3) is a wedge-shaped triangular bone at the base of the spinal column, above the caudal (tail) vertebrae, or coccyx, that articulates with the pelvic girdle. In humans it is usually composed of five vertebrae, which fuse in early adulthood. The top of the first (uppermost) sacral vertebra articulates with the fifth lumbar vertebra. The transverse processes of the first three sacral vertebrae are fused to form wide lateral *ala*. Between the fused transverse processes of the lower sacral vertebrae, on each side, are a series of four openings (sacral foramina); the sacral nerves and blood vessels pass through these openings. A sacral canal running down through the centre of the sacrum represents the end of the vertebral canal: the functional spinal cord ends at about the level of the first sacral vertebra but its continuation can be traced through the sacrum to the first coccygeal vertebra.

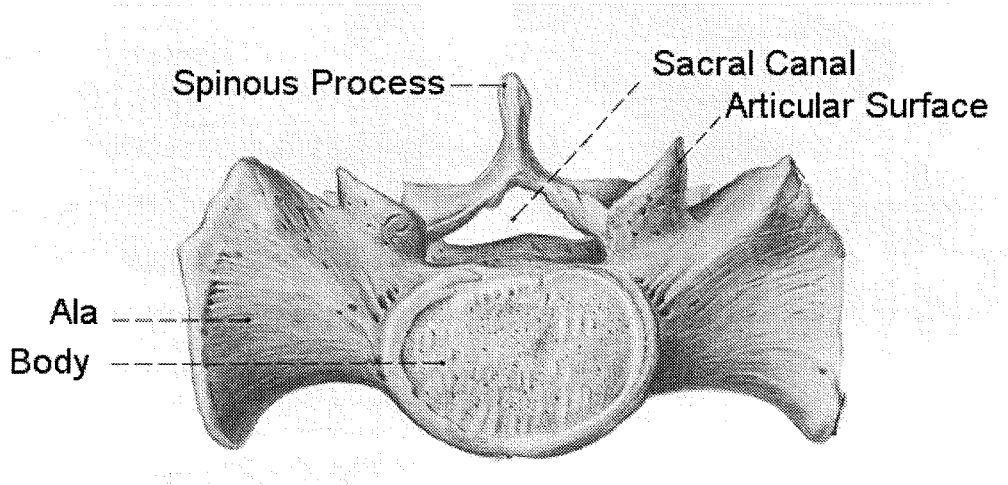


Figure 3 : Upper sacrum anatomy (top view). From Sobotta¹.

The intervertebral joints

Between two consecutive lumbar vertebrae, there are three joints: a joint between the vertebral bodies, and two joints between the articular processes (zygapophyseal joints or facet joints). Part of the interbody joint is the intervertebral disk, a layer of strong, deformable, soft tissue allowing load transfer and movement of the vertebrae in all directions. The structural and functional properties of the intervertebral disk will be discussed in detail below. The zygapophyseal joints are synovial joints, covered by articular cartilage, filled with synovium, and enclosed by a fibrous capsule (Figure 4). The facet joints prevent anterior displacement and rotary dislocation of the L5 vertebra. The extent to which a facet joint can prevent movement strongly depends on the shape and position of the articular processes.

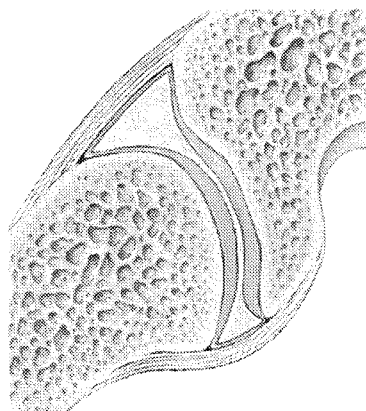


Figure 4 : Facet joint (from www.spineuniversity.com).

The intervertebral disk

The lumbar intervertebral disk consists of a central nucleus (*nucleus pulposus*) surrounded by a fibrous ring (*annulus fibrosus*) (Figure 5). A third component of the disk is the vertebral endplate, which covers the top and bottom of the disk. The central fibers of the inner two-third of the annulus fibrosus attach directly to the cartilaginous endplates and the peripheral fibers insert along the bony vertebral body margin (ring apophysis) as the so-called Sharpey's fibers.

The nucleus pulposus is an acellular meshwork of proteoglycan units, aggregates, and collagen fibers collectively called the nucleus matrix. The proteoglycans make up 65% of the dry weight of the nucleus, the collagen (predominantly type II) 15-20%. The proteoglycan units are formed by many glycosaminoglycans linked to a core protein. These proteoglycans contain water, the main component of the nucleus pulposus. The high water content of the nucleus pulposus (70-90%) is essential for maintaining its principle function: sustaining and transmitting compressive weight. When the intervertebral disk is compressed, the pressure in the nucleus pulposus will increase resulting in deformation of the nucleus pulposus. The pressure is then exerted radially onto the annulus fibrosus. Subsequently, the tension in the annulus fibrosus will rise and this will prevent further radial expansion of the nucleus pulposus.

Water is also the main component of the annulus fibrosus (60-70%) but collagen (mainly type I) makes up 50-60% of the dry weight and only 20% of the dry annulus is proteoglycan. This high concentration of collagen thickens the annulus. Another difference between the nucleus and the annulus is the high concentration of elastic fibers in the annulus (10% of the dry weight). These elastic fibers are arranged circularly, obliquely and vertically in the lamellae of the annulus and are predominantly located towards the attachment sites of the annulus on the vertebral endplate.

The vertebral endplates are also composed of water, proteoglycans, and collagen. The relative concentrations of the components in the endplate are similar to that in the disk: high water and proteoglycan concentrations in the part of the endplate adjacent to the nucleus; high water and high collagen concentrations in parts of the endplate in contact with the annulus. Small molecules can therefore freely diffuse from the vertebrae to the avascular disk elements, important for nutritional needs.

The ligaments

In general, ligaments provide joint-stability and limitation to the range of motion. The ligaments of the lumbar spine may be divided in those connecting:

- the 5th lumbar vertebral body to the sacrum
- the laminae
- the spinous processes
- the articular processes

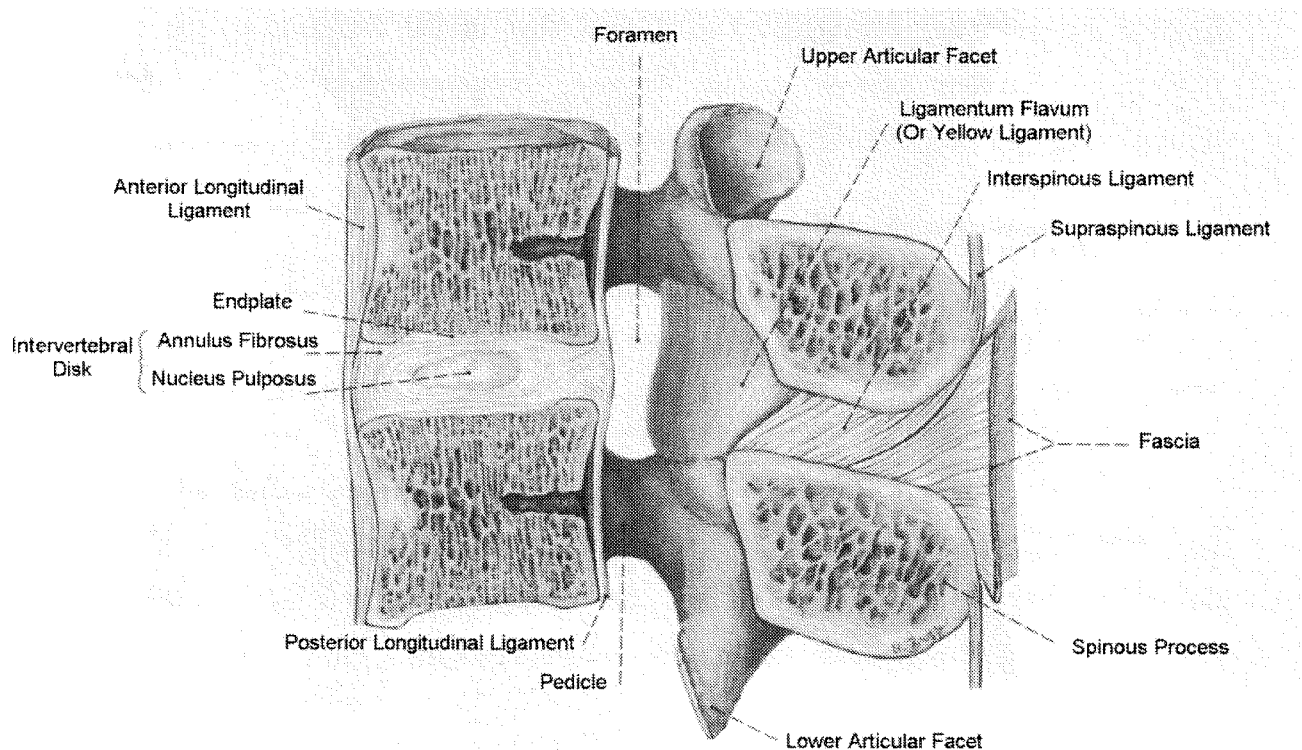


Figure 5 : Ligaments of a lumbar segment. From Sobotta¹.

Ligaments connecting the 5th lumbar vertebral body to the sacrum

The ligaments that interconnect L5 vertebral body to the sacrum are the *anterior longitudinal ligament* and the *posterior longitudinal ligament*. The two ligaments are strongly related with the *annulus fibrosus* of the intervertebral disks. During extension, the anterior longitudinal ligament resists anterior separation of the vertebrae, while the posterior longitudinal ligament prevents posterior separation during flexion. The annulus fibrosus resists distraction, bending, sliding, and twisting of the intervertebral joint during all kinds of motion.

Ligaments connecting the laminae

The *ligamentum flavum* is a short, thick ligament interposed between the laminae of two consecutive vertebrae. This ligament consists of yellow elastic tissue and is therefore often called the yellow ligament. Its unique elastic properties are thought to be necessary for returning the flexed lumbar spine into the extended position and for preserving the upright posture.

Ligaments connecting the spinous processes

The *interspinous ligaments* connect two spinous processes. They limit forward bending by preventing supraphysiological separation of the two spinous processes. The supraspinous ligament interconnects the apices of the spinous processes. The supraspinous ligament is closely blended with the aponeurosis of the back muscles.

Ligaments connecting the articular processes

The *capsular ligaments* form the capsules of the zygapophyseal joints. They function as membranes by preventing excessive motion of these joints.

The lumbo-sacral and ilio-lumbar ligaments

The *lumbo-sacral ligament* is short, thick, and triangular and connects the lower and front part of the transverse process of the fifth lumbar vertebra to the lateral part of the base of the sacrum. The *ilio-lumbar ligament* binds the transverse process of the fifth lumbar to the ilium. The ilio-lumbar ligament consists of five parts: anterior, superior, posterior, inferior, and vertical.

INTRODUCTION OF THE ANTHROPOMETRY STUDY

When designing an anterior lumbar interbody fusion (ALIF) cage for the lumbo-sacral segment (L5-S1), accurate and complete geometrical parameters of the vertebral body and of the intervertebral disk are needed. Many studies were carried out on geometry of the lumbar vertebrae, but very few of those on the L5-S1 segment. Moreover, the morphometric description of these structures is often incomplete.

Previous studies focused on the lumbar region and were done using plain X-ray films^{3,4,5,6}, or Computed Tomography (CT) scans^{7,8,9,10,11,12}. The value of the results depends on the number of tested samples and the precision of the used method. The precision and the number of tested samples vary enormously when comparing a study to another one. Moreover, certain studies were carried out *in vivo* with a great number of samples, while others were conducted on cadaveric samples with a number of samples often lower than ten.

Concerning the measurements made in these studies, they are unfortunately not complete and give only limited information on the morphometric characteristics of the studied segments. No study gives at the same time the posterior and anterior height of the intervertebral disk, its depth, the angle formed between the two vertebrae, the surface of each vertebral endplate, as well as complete dimensions of each vertebral body.

The X-ray films provide relative measurements of anthropometric data (except when magnification is known) and CT scans provide a direct measurement of their absolute value. As a result, it is possible to measure the circumference and surface area of the endplate, an important parameter when designing implants for lumbo-sacral fusion.

The purpose of this study is to collect accurate anthropometric data of normal lumbo-sacral segments, using X-ray and CT, in a series of 10 cadaveric specimens and 30 patients. Another goal is to estimate, with the aid of surgeons, the maximum available space for the insertion of a cage in the intervertebral disk using a “less-invasive” surgical procedure.

MATERIAL AND METHODS

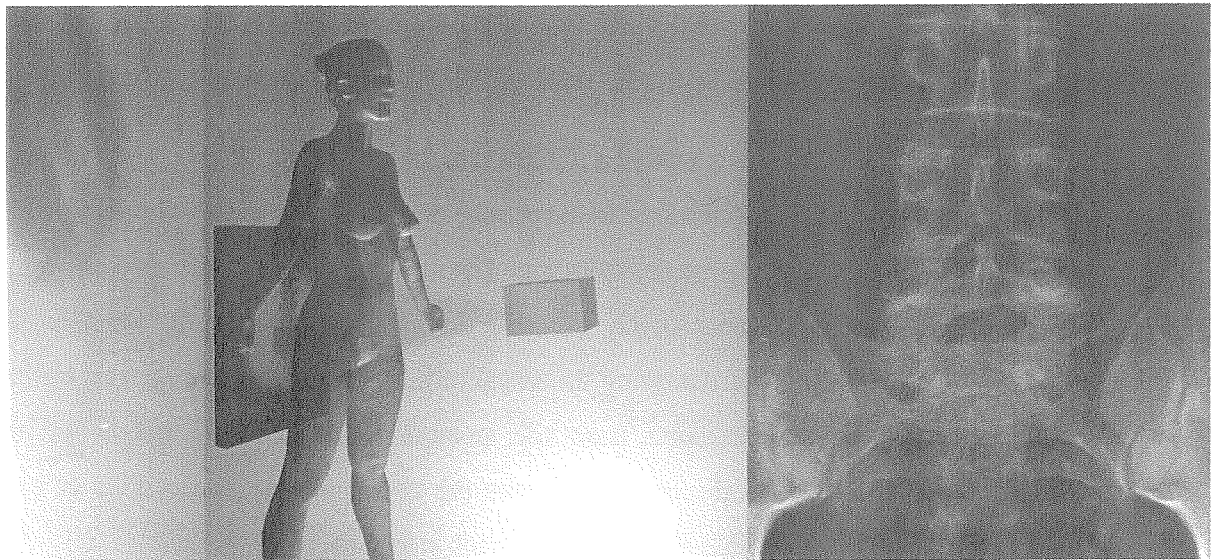
Study population

This study was carried out on 10 cadaveric specimens and on 30 patients with low back pain and varying degrees of disk degeneration on adjacent segments (i.e. segments upper than the L5-S1 studied segment). There were 24 males, mean age 47.3±18.8, and 16 females, mean age 49.9±15.4, with an age range of 16-86 years. L5-S1 segments with vertebral body abnormalities, gross spinal pathology (including spondylolisthesis, and disk space collapse)

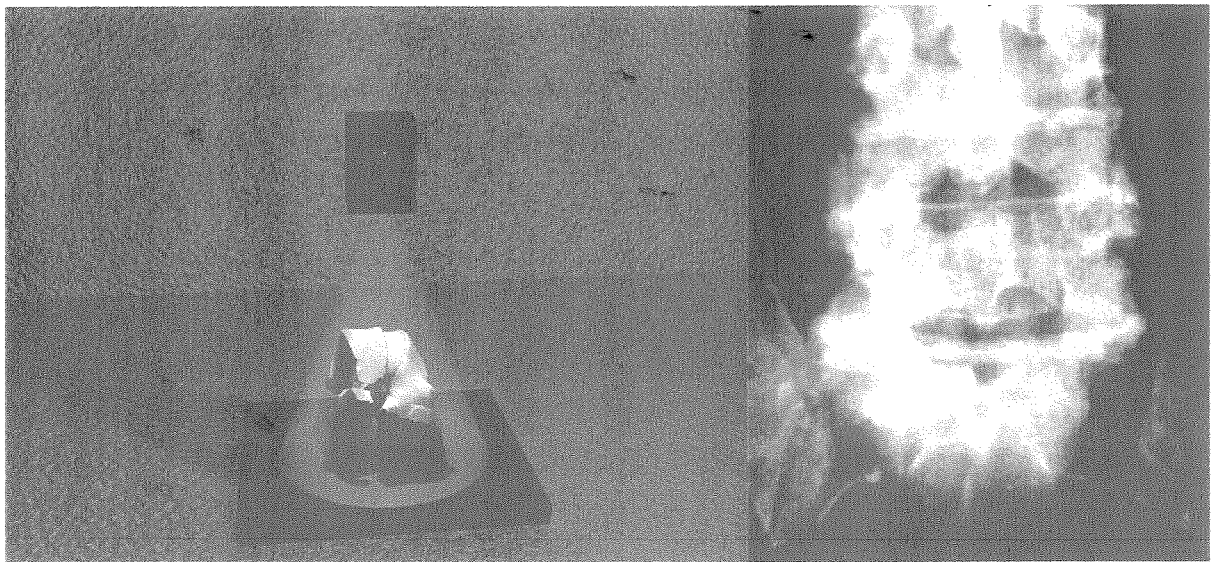
and those who had undergone spinal surgery were excluded. The inserted implant aims at stabilizing the spinal unit and at restoring the original height of the intervertebral disk.

Measuring methods

Face and profile X-rays were performed on both cadaveric or patients' spine (Figure 6). They were centered on the lumbar region. Patients are standing during the X-ray exposure. CT was performed on the same specimens and patients, which were laying down horizontally (Figure 7). Small errors could be associated to the difference in the position of the patients.

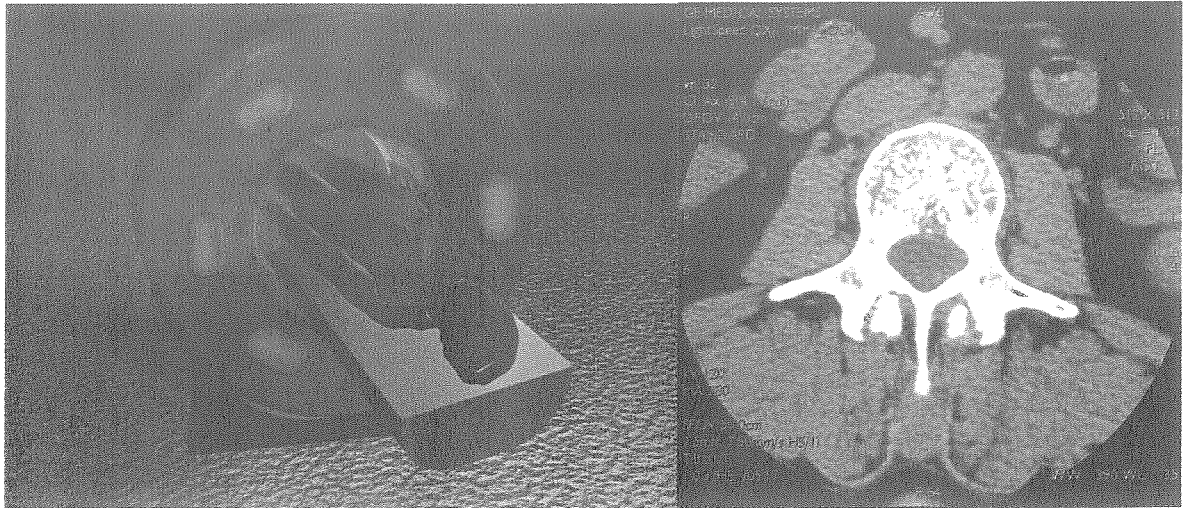


Frontal X-rays performed on a patient. The spine is not in contact with the film plate.

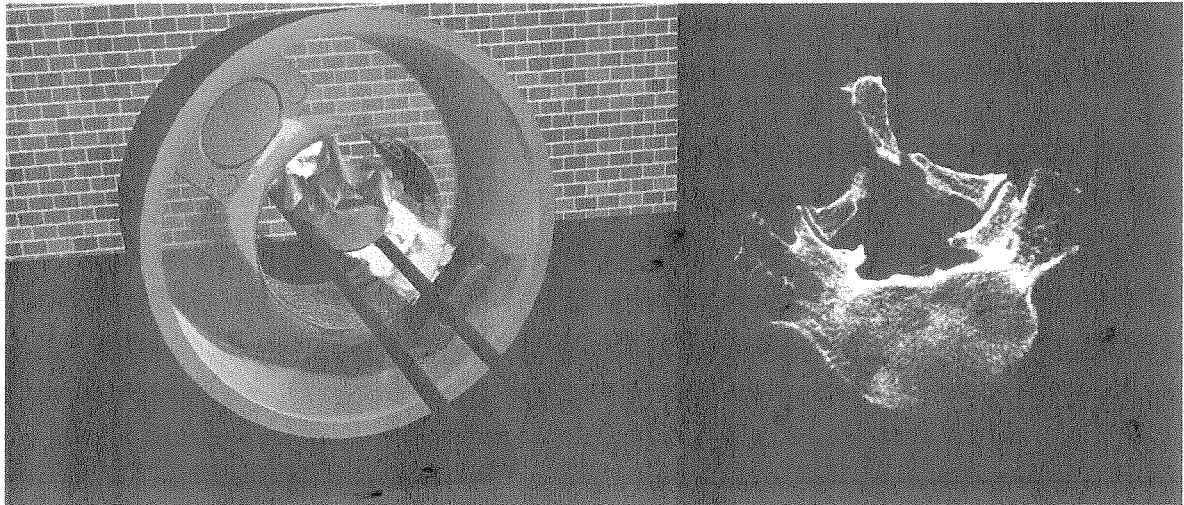


Frontal X-rays performed on a specimen. The specimen is in contact with the film plate.

Figure 6 : Face X-rays performed on patients and cadaveric specimens. The pictures to the right are examples of the obtained contrast.



Computed tomograph used for patients.



Peripheral quantitative computed tomograph used for cadaveric specimens (pQCT).

Figure 7 : CT performed on patients and specimens. The pictures to the right are an example of the obtained contrast.

Measured parameters included the posterior intervertebral disk height (PIDH), the middle intervertebral disk height (MIDH), the anterior intervertebral disk height (AIDH), the lower vertebra depth (LVD), the lower vertebra width (LVW), the upper vertebra depth (UVD), and the upper vertebra width (UVW). They are all represented on Figure 8, but were measured on the CT scans in order to obtain accurate data. Surface of the lower endplate (LES) and of the upper endplate (UES) was estimated using an ellipse model of the endplate. Therefore the endplate surface (ES) can be calculated as:

$$ES = \pi \cdot UVD \cdot UVW / 4$$

L5-S1 angle (θ) was measured as the angle between the upper endplate and the lower endplate using lateral X-ray films.

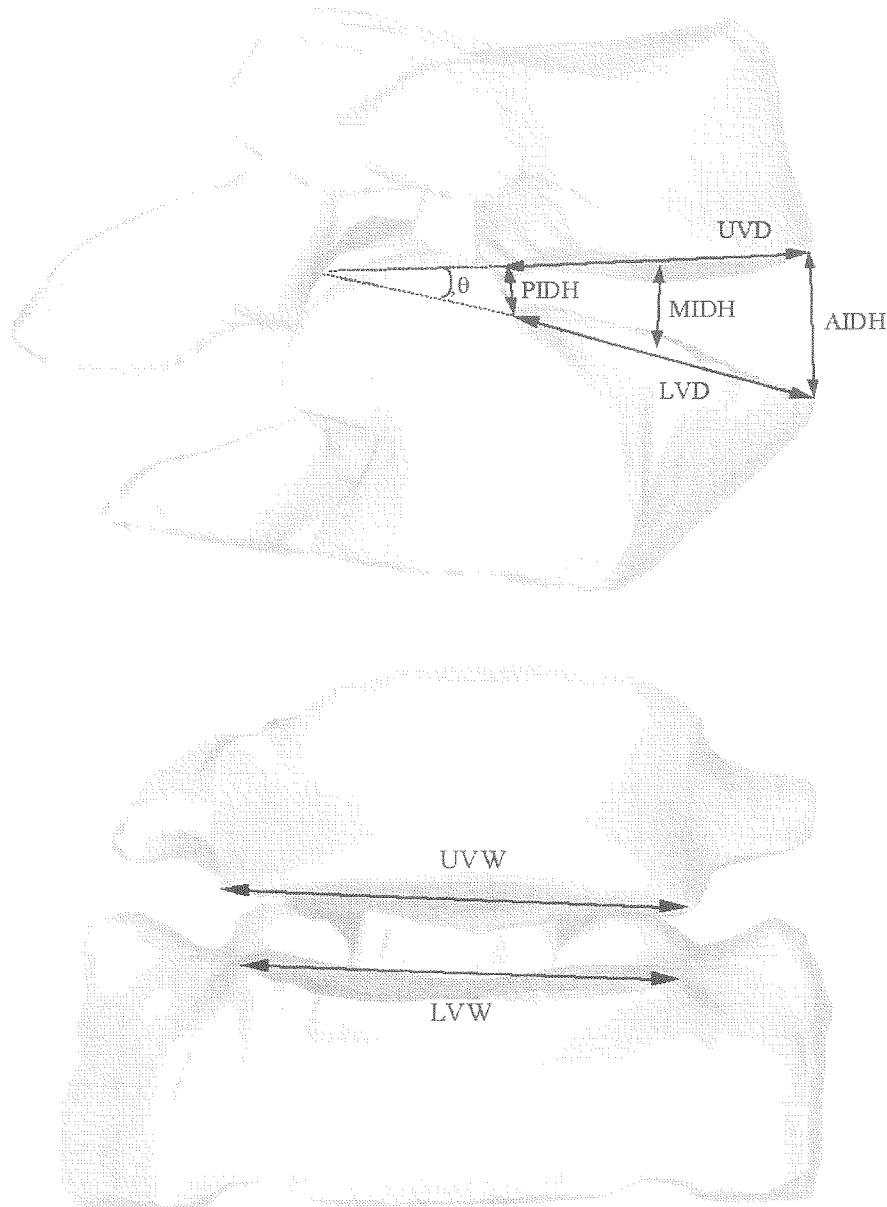


Figure 8 : Lateral (a) and frontal (b) view of a L5-S1 segment. Definition of the different measured parameters.

Four experimented spinal surgeons analyzed the X-ray films and drew on them the maximum available intervertebral disk volume that can be removed with a less-invasive technique. Absolute measured values were corrected with the enlargement factor associated with any standard X-ray measurement. Measurement of the same parameter on both X-ray films and CT scans allowed determination of these parameters.

Comparing the results obtained with the CT and with the X-ray allowed calculation of the enlargement factor to apply to the X-ray films in order to obtain the real dimensions. On a front X-ray film of patients, the measured values had to be corrected by a factor of 1.183 ± 0.128 , whereas, on the lateral X-ray film, the measured values had to be corrected by a factor

of 1.299 ± 0.129 . The fact that the value measured on X-ray films were not exact values is simply due to the distance separating the spine to the film (Figure 6). It is also obvious that on a lateral view of the spine, the patient' spine is more distant to the film than in a frontal view. That is why the correction factor is higher on lateral views. Obviously there were few corrections to apply for the cadaveric samples (1.032 ± 0.012 for the front view and 1.051 ± 0.020 for the lateral view). This is explained by the fact that specimens were in direct contact with the X-ray film.

Statistical analysis

The statistical analysis was performed using the S-PLUS software package (MathSoft Inc. USA). All results are presented with their mean, standard deviation and min-max values. A Wilcoxon rank-sum test was used to compare the data between male and female with a significance level $P < 0.05$.

RESULTS

Table 1 summarizes the mean value, standard deviations and range of data for the L5-S1 segment obtained from measurements of lateral and frontal X-ray films and of cross-sectional and lateral CT images in 40 patients.

There is no significant difference between male and female posterior ($p=0.437$), middle ($p=0.623$) and anterior ($p=0.840$) intervertebral disk height. However, the variation of the disk height is high. Indeed, the middle intervertebral disk height varies from 6.0 to 16.2mm. Considering the disk angle, there is also no significant difference between male and female values ($p=0.904$). The range of data is large and varies from 3.0 to 31.0 degrees. Significant differences were observed between male and female UVW ($p=0.0012$), LVW ($p=0.002$), LVD ($p=0.0131$), UVD ($p=0.0202$), UES ($p=0.0025$) and LES ($p=0.001$). For these parameters, male values are greater than the female ones.

The upper and lower endplate are similar in width and depth. Indeed, no significant differences were seen between both endplates dimensions ($p > 0.17$). Furthermore, the upper endplate surface is not significantly different than the lower endplate surface ($p=0.248$).

Dimensions for the space available for ALIF are represented in Table 2 and their relative values in Table 3. Their relative values are the estimated available space dimensions divided by their mean corresponding dimensions of the endplate (e.g. relative cage width = cage width / $((UVW+LVW)/2)$). There are no significant differences between male and female cage depth ($p=0.2199$), whereas cage width is significantly larger for male

($p=0.0396$). All significant difference disappear when comparing male and female relative cage depth ($p=0.621$) and relative cage width ($p=0.909$).

Table 1: L5-S1 intervertebral disk dimensions for 40 samples (mean \pm standard deviation and (min-max)). PIDH posterior intervertebral disk height, MIDH middle intervertebral disk height, AIDH anterior intervertebral disk height, LVD lower vertebral depth, LVW lower vertebral width, UVD upper vertebral depth, UVW upper vertebral width, LES lower endplate surface, UES upper endplate surface. A star indicates a significant difference between male and female.

Dimension	Sex	L5-S1 disk
PIDH [mm]	M+F	5.1 \pm 2.0 (1.8-11.6)
	F	5.7 \pm 2.3 (3.3-11.6)
	M	4.7 \pm 1.8 (1.8-8.3)
MIDH [mm]	M+F	10.9 \pm 2.6 (6.0-16.2)
	F	11.4 \pm 2.2 (7.2-15.2)
	M	10.7 \pm 2.5 (6.0-16.2)
AIDH [mm]	M+F	14.9 \pm 3.2 (9.2-21.6)
	F	15.0 \pm 2.1 (11.6-19.2)
	M	14.8 \pm 3.8 (9.2-21.6)
LVD * [mm]	M+F	33.3 \pm 3.4 (26.6-41.7)
	F	31.3 \pm 2.7 (26.6-36.7)
	M	34.4 \pm 3.2 (30.0-41.7)
LVW * [mm]	M+F	49.6 \pm 5.0 (41.7-60.0)
	F	45.5 \pm 2.2 (41.7-48.3)
	M	51.9 \pm 4.6 (44.2-60.0)
UVD * [mm]	M+F	33.8 \pm 3.2 (27.5-41.7)
	F	31.8 \pm 2.7 (27.5-35.8)
	M	35.0 \pm 3.0 (30.8-41.7)
UVW * [mm]	M+F	51.1 \pm 4.7 (40.8-60.0)
	F	47.4 \pm 3.4 (40.8-50.4)
	M	53.1 \pm 4.2 (44.2-60.0)
LES * [cm ²]	M+F	13.1 \pm 0.2 (0.9-2.0)
	F	11.1 \pm 0.1 (0.9-1.4)
	M	14.1 \pm 0.2 (1.1-2.0)
UES * [cm ²]	M+F	13.6 \pm 0.2 (0.9-2.0)
	F	11.9 \pm 0.2 (0.9-1.4)
	M	14.6 \pm 0.2 (1.2-2.0)
L5-S1 Angle [deg]	M+F	19.1 \pm 5.9 (3.0-31.0)
	F	19.2 \pm 4.8 (13.0-27.0)
	M	19.1 \pm 6.6 (3.0-31.0)

Table 2 : Surgeons evaluation of the available space for the insertion of a fusion cage. A star indicates a significant difference between male and female.

Dimension [mm]	Sex	L5-S1 disk
Cage width *	M+F	33.3 ± 5.2 (25.0-41.7)
	F	30.8 ± 4.9 (25.0-38.3)
	M	35.3 ± 4.8 (28.3-41.7)
Cage depth	M+F	23.6 ± 2.7 (19.2-29.2)
	F	22.7 ± 1.9 (19.2-25.0)
	M	24.4 ± 3.1 (20.8-29.2)

Table 3 : Surgeons evaluation of the relative available space for the insertion of a fusion cage. This is the absolute dimension of the cage divided by the corresponding absolute dimension of the endplate.

Dimension [-]	Sex	L5-S1 disk
Relative Cage width	M+F	0.66 ± 0.07 (0.55-0.78)
	F	0.65 ± 0.07 (0.57-0.78)
	M	0.66 ± 0.08 (0.55-0.77)
RelativeCage depth	M+F	0.73 ± 0.05 (0.65-0.79)
	F	0.74 ± 0.04 (0.65-0.79)
	M	0.73 ± 0.05 (0.65-0.79)

DISCUSSION

Many anthropometric studies were performed on human vertebrae^{4,5,6,7,8,9,10,13,14,15,16,17}. The value of their data depends extensively on the number of the samples and on the accuracy of the chosen methods. Among all of these studies, only the one by Zhou et al.¹² used an accurate methodology, analyzed enough samples (126) and indicated value for the lumbo-sacral intervertebral dimensions. However, no study estimated the available space for an anterior lumbar interbody fusion (ALIF). A comparison of our results with those obtained by Zhou et al.¹² is presented in Figure 9.

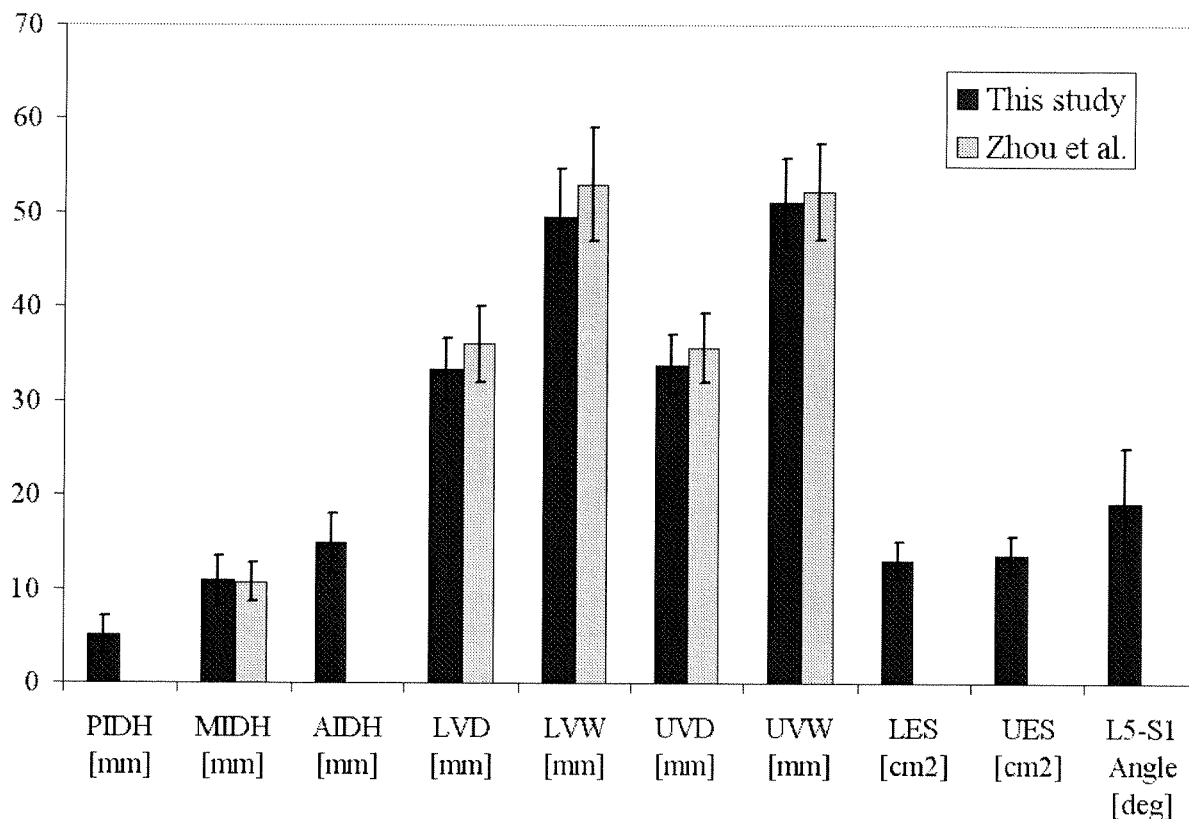


Figure 9: Comparison between results obtained for the L5-S1 segment in this study and those obtained by Zhou et al.¹² The mean value and its associated standard deviation are presented for the “male+female” group.

Our data are close to those obtained by Zhou et al.¹² and indicates that our population of 40 specimens is representative. Unfortunately, there were only a few previous reports on disk height in the lower vertebral column, either from normal population or from patients with low back pain. Although the study by Zhou et al. was carried out in patients with low back pain, the mean measured intervertebral disk height in this study on normal L5-S1 segment is similar. However, the somehow higher value of the vertebral body dimensions obtained by Zhou et al. probably indicates some degeneration of the intervertebral disks. Saraste et al.¹⁴ reported the measurement of disk height on plain X-ray films, but it was confirmed in the study of Zhou et al. that such techniques are too inaccurate for precise conclusions. Nevertheless, accurate knowledge of the dimensions of the disk space is crucial for studying low back pain and its causes, and also for designing ALIF cages. This information is important not only for research but also for clinical practice. Our study provides dimensions, such as the posterior and anterior intervertebral disk height and the disk angle, that were not measured elsewhere with an accurate method.

Techniques for anterior interbody lumbar fusion have now been adapted to restore and preserve disk height, and a choice of types of graft materials and implant have been used for this purpose^{18,19,20,21,22,23}. A critical part of the design is the size of the implant. If an implant is too small, it does not restore the height, it could collapse in the center of the vertebral body and could move on the endplates. Furthermore, the smaller the implant, the larger is the stress that it will experience. If the implant is too large, the surgical procedure will be more challenging and more invasive, and may lead to serious damage of the surrounding tissues.

In the perspective of using phosphocalcic cement as material of the implant, precise knowledge of the intervertebral disk dimensions is necessary. Since such materials have low mechanical strength compared to metals, it is worthwhile to use the maximum available space for its insertion. Therefore, stresses will be lowered at the cost of a more challenging surgical procedure. The largest possible cage (for its insertion with a “less-invasive” surgical procedure) should have a relative width compared to the endplate width of 66% and a relative depth of 73% (Table 3), no matter what the sex of the patient is. The implant area which is in contact with the endplate should cover 60% of the total endplate area. Closkey et al.²⁴ reported that the area covered with the bone graft should be at least 30% of the total endplate in order to provide a margin of safety, whilst Pearcy et al.²⁵ concluded that at least 40% of the cross-sectional area should be covered by the graft. Our carefully dimensioned ALIF cage inserted in the L5-S1 intervertebral disk is shown in Figure 10.

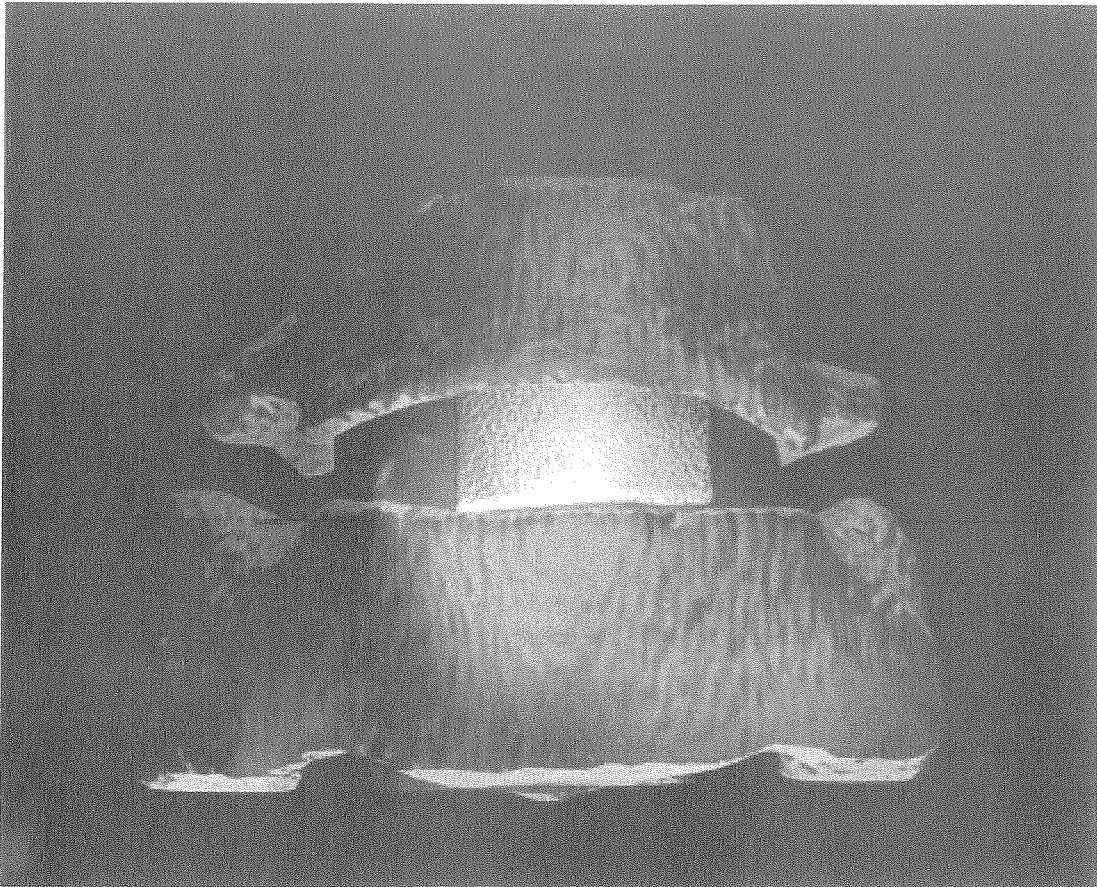


Figure 10 : The ideal implant inserted in the L5-S1 intervertebral disk.

Our study provides the necessary values for the design of an ALIF cage to treat patients with low back pain. Although the number of specimens is low compared to other studies, our data are representative of those obtained by Zhou et al.¹² It would be useful in the future to complete these series in order to improve the statistical analysis. In this study, estimated dimensions of an ALIF cage are related to surgeons' know-how. These dimensions are upper limits for a "less-invasive" anterior approach of the L5-S1 segment

REFERENCES

- 1 Putz R, Pabst R. Sobotta, Atlas d'anatomie humaine, tome 2. 20ème édition remaniée. Editions médicales internationales, France.
- 2 Smit, Th.H. The mechanical significance of the trabecular bone architecture in a human vertebra. 1996. Thesis Technical University Hamburg-Harburg, Shaker Verlag, Aachen.
- 3 Elsberg CA, Dyke CC. Diagnosis and localization of tumours of spinal cord by means of measurements made on X-ray films of vertebrae and the correlations of clinical and X-ray findings. Bull Neurol Inst New York 1934(3):359–394.
- 4 Gilad I, Nissan M. Sagittal evaluation of elemental geometrical dimensions of human vertebrae. J Anat 1985(143): 115–120.
- 5 Gilad I, Nissan M. Sagittal radiographic measurements of the cervical and lumbar vertebrae in normal adults. Br J Radiol 1985(58):1031–1034 (12):183–184.
- 6 Nissan M, Gilad I. The cervical and lumbar vertebrae – an anthropometric model. Eng Med 1984(13):111–114 (145):327–335.
- 7 Eisenstein S. Lumbar vertebral canal morphometry for computerised tomography in spinal stenosis. Spine 1983(8):187–191.
- 8 Fang D, Cheung K, Ruan D, Chan F. Computed tomographic osteometry of the Asian lumbar spine. J Spinal Disord 1994(7):307–316.
- 9 Postacchini F, Pezzeri G, Montanaro. A, Natali G. Computerised tomography in lumbar stenosis – a preliminary report. J Bone Joint Surg Br 1980(62):78–82.
- 10 Van Schaik JJ, Verbiest H, Van Schaik FD. Morphometry of lower lumbar vertebrae as seen on CT scans: newly recognized characteristics. AJR 1985(145):327–335.
- 11 Zindrick M, Wilts L, Doornik A, Widell E, Knight G. Analysis of the morphometric characteristics of the thoracic and lumbar pedicles. Spine 1987(12):160–166.
- 12 Zhou SH, McCarthy ID, McGregor AH, Coombs RRH, Hughes SPF. Geometrical dimensions of the lower lumbar vertebrae – analysis of the data from digitised CT images. Eur Spine J 2000(9) :242-248.
- 13 Larsen JL, Smith D. Vertebral body size in lumbar spinal canal stenosis. Acta Radiol Diagn 1980(21):785–788.
- 14 Saraste H, Brostrom LA, Aparisi T, Axdorph G. Radiographic measurement of the lumbar spine – a clinical and experimental study on man. Spine 1985(10):236–241.
- 15 Berry JL, Moran JM, Berg WS, Steffee AD. A morphometric study of human lumbar and selected thoracic vertebrae. Spine 1987(12): 362–367.
- 16 Eisenstein S. The morphometry and pathological anatomy of the lumbar spine in South African negroes and caucasoids with specific reference to spinal stenosis. J Bone Joint Surg Br 1977(59):173–180.
- 17 Twomey LT, Taylor R. Age changes in lumbar vertebrae and intervertebral discs. Clinical Orthop 1987(224):97–104
- 18 Brantigan JW, Steffee AD. A carbon fiber implant to aid interbody lumbar fusion. Spine 1993(18): 2106–2117.
- 19 Calandruccio R A, Benton B F. Anterior lumbar fusion. Clin Orthop 1964(35): 63–68.

- 20 Kozak JA, Heilman AE, O'Brien JP. Anterior lumbar fusion options. *Clin Orthop* 1994(300):45–51.
- 21 Leong JC, Chow SP, Yau AC. Titanium-mesh block replacement of the intervertebral disk. *Clinical Orthop* 1994(300):52–63.
- 22 Loguidice VA, Johnson RG, Guyer RD, Stith WJ. Anterior lumbar interbody fusion. *Spine* 1988(13):366–369.
- 23 Newman M, Grinstead G. Anterior lumbar interbody fusion for internal disc disruption. *Spine* 1992(17):831–833.
- 24 Closkey RF, Parsons JR, Lee CK, Blacksin MF, Zimmerman MC. Mechanics of interbody spinal fusion – analysis of critical bone graft area. *Spine* 1993(18):1011–1015.
- 25 Percy MJ, Evans JH, O'Brien JP- The load bearing capacity of vertebral cancellous bone in interbody fusion of the lumbar spine. *Eng Med* 1983(12):183–184

**EXHAUSTIVE MECHANICAL
CHARACTERIZATION OF BRUSHITE AND
HYDROXYAPATITE CEMENTS¹****ABSTRACT**

Compression, tension and torsion tests were designed and completed successfully on a brushite and a precipitated hydroxyapatite cement in moist condition. Elastic and strength properties were measured for these three loading cases.

For each cement, the full set of strength data was fitted to an isotropic Tsai-Wu criterion and the associated coefficients identified. Since the compressive Young's moduli were about 10% larger than the tensile moduli, the full set of elastic data of each cement was fitted to a conewise linear elastic model. Hysteresis of the stress-strain curves was also observed, indicating dissipation mechanisms within these cement microstructures.

A comparison of the measured mechanical properties with human cancellous bone confirmed the indication of brushite as a bone filling material and the potential of the hydroxyapatite cement as a structural biomaterial.

¹ This chapter has been published in *Biomaterials* 2001;22(21):2937-2945 with the title :” Exhaustive mechanical characterization of brushite and hydroxyapatite cements”. †Charrière E, *Terrazoni S, *Pittet C, *Lemaitre J, †Mordasini P, †Dutoit M, Zysset PK. Department of Mechanical Engineering, EPFL; †Hôpital Orthopédique de la Suisse Romande ; *Department of Material Sciences, EPFL

Introduction

In weight bearing structures such as the human skeleton, each newly developed biomaterial needs to be mechanically tested to ensure its functionality and reliability. For metals, the test protocols are well known and standardized. For biocements, measurement of their multiaxial mechanical properties is more difficult, since their behavior depends heavily on the microstructural defects associated with the manufacturing process.

Two calcium phosphate cements, brushite and hydroxyapatite, were recently developed as bone substitution materials in orthopaedic surgery (e.g. vertebroplasty and lumbar fusion). The brushite cement is biocompatible, resorbable, osteoconductive and injectable since it hardens in physiological conditions. In contrast, hydroxyapatite cement is less resorbable and is not injectable. However, hydroxyapatite seems to present a higher strength, which may open the perspective for its use in weight-bearing regions of the skeleton subjected to high multiaxial stresses. The purpose of this work is an extended characterization of the multiaxial elastic and failure properties of these two cements in moist condition.

Elasticity

Cement materials in a moist environment may exhibit different tensile and compressive elastic properties. Similar behaviors were found for concrete and ceramics [1,2,3,4]. In general, the compressive Young's modulus is higher than the tensile one. The difference between both moduli is often explained by the microcrack opening process in tension and by its closure in compression. Two parameters are required (Young's modulus and Poisson's ratio) to describe the elastic properties of an isotropic material. However, the elastic behavior of materials with different compressive and tensile elastic moduli cannot be described accurately with only two parameters.

A piecewise linear elasticity model was proposed by Curnier et al. [5] in order to overcome this limitation. This approach divides stress space in convex domains separated by hyperplanes. A simple division consists in choosing compression and a tension halfspace separated by the hyperplane where the first invariant of the stress tensor equals zero ($\text{tr}\boldsymbol{\sigma}=0$). In stress space, the complementary free energy W and the resulting strain tensor $\boldsymbol{\varepsilon}$ are expressed by:

$$W(\boldsymbol{\sigma}) = -\frac{\nu[\text{tr}\boldsymbol{\sigma}]}{2E[\text{tr}\boldsymbol{\sigma}]} \text{tr}^2(\boldsymbol{\sigma}) + \frac{1 + \nu[\text{tr}\boldsymbol{\sigma}]}{2E[\text{tr}\boldsymbol{\sigma}]} \text{tr}(\boldsymbol{\sigma}^2) \quad \text{Equation 1}$$

$$\boldsymbol{\varepsilon}(\boldsymbol{\sigma}) = \frac{-\nu[\text{tr}\boldsymbol{\sigma}]}{E[\text{tr}\boldsymbol{\sigma}]} \text{tr}(\boldsymbol{\sigma}) \mathbf{I} + \frac{1+\nu[\text{tr}\boldsymbol{\sigma}]}{E[\text{tr}\boldsymbol{\sigma}]} \boldsymbol{\sigma} \quad \text{Equation 2}$$

where

$$E[\text{tr}\boldsymbol{\sigma}] := \begin{cases} E_- & \text{if } \text{tr}\boldsymbol{\sigma} < 0 \\ E_+ & \text{if } \text{tr}\boldsymbol{\sigma} > 0 \end{cases}, \quad \nu[\text{tr}\boldsymbol{\sigma}] := \begin{cases} \nu_- & \text{if } \text{tr}\boldsymbol{\sigma} < 0 \\ \nu_+ & \text{if } \text{tr}\boldsymbol{\sigma} > 0 \end{cases}$$

E_- is the compressive Young's elastic modulus

E_+ is the tensile Young's elastic modulus

ν_- is the compressive Poisson's ratio

ν_+ is the tensile Poisson's ratio

Continuity of the elastic law at the hyperplane requires

$$2\mu = \frac{E_-}{1+\nu_-} = \frac{E_+}{1+\nu_+} \quad \text{Equation 3}$$

where μ is the Lamé shear constant. This constraint limits the number of independent parameters to 3. In this study, the three experimentally determined parameters are the compressive and tensile Young's moduli (E_- and E_+) and the Lamé shear constant μ .

Failure models

Classical failure criteria used for metals such as Tresca or Von Mises do not describe accurately the strength behavior of biocements. In particular, these criteria predict the same strength in tension and compression and an infinite resistance towards hydrostatic tension, which are both incompatible with the experimentally observed properties of porous cements. A number of failure criteria attempted to overcome these limitations [6,7,8,9,10,11] among which the smooth envelope of Tsai and Wu [8]. This criterion is often used to predict failure for material loaded in a complex state of stress [12,13,14,15]. For isotropic materials, the Tsai-Wu criterion can be expressed as a function of the first two invariants of the stress tensor:

$$\alpha\sigma_I + \beta\sigma_{II} + \gamma\sigma_I^2 = 1 \quad \text{Equation 4}$$

where

$$\sigma_I = \text{tr}[\boldsymbol{\sigma}]$$

$$\sigma_{II} = \frac{1}{2}\text{tr}(\boldsymbol{\sigma}^2)$$

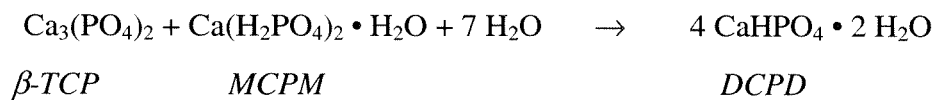
α , β , γ are the three parameters to be experimentally determined.

The 3D geometrical representation of this criterion is an ellipsoid that can be translated along the vector (1,1,1) of the three principal axes σ_1 , σ_2 and σ_3 . A drawback of this criterion leads to the fact that tensile-tensile and compressive-compressive interactions cannot be treated independently. Its main advantage is that it requires only three independent parameters and that it imposes distinct limits in compression and tension. This model will be used in this work to fit the strength data of brushite and hydroxyapatite.

Materials and methods

Brushite

The calcium phosphate cement used in this study is a modification of the brushite cement developed by Mirtchi et al. [16,17]. It was prepared by mixing two phosphate powders in presence of water. The starting powders were β -tricalcium phosphate (β -TCP, synthesized in-house) and monocalcium phosphate monohydrate (MCPM, Albright&Wilson), reacting in presence of water to form precipitated brushite (dicalcium phosphate dihydrate, DCPD) according to the reaction presented below. A small amount of sodium pyrophosphate ($\text{Na}_2\text{H}_2\text{P}_2\text{O}_7$, Fluka) was added to the starting powders as a setting regulator. Mixing of the powders was made in a sulfuric acid solution (0.1M).



Proportions of the reactants were not stoichiometric, the β -TCP powder being in excess.

β -TCP : MCPM weight ratio was 3:2, β -TCP : NaHPP was 80:1. Solid/Liquid ratio was 2.5 g/ml.

The cement paste was prepared in a mortar, thoroughly kneaded with a spatula and poured into a mold. Air bubbles entrapped in the paste during mixing were allowed to escape the cement by vibrating the mold on a Reax 2000 machine (Heidolph Elektro GmbH, Germany). Filling of the mold was made sequentially, alternating feeding and vibrating. The external wall of the mold was made of silicone. Two kinds of samples were prepared with the same external shape, but some were hollow while the others were solid pieces. Hollow samples were prepared with a mold containing a metallic core in its center. A thin film of demolding agent was applied on the core to ensure easy removal. A schematic representation of a sample is presented in Figure 1. The cylindrical part of the sample had an external diameter of 18 mm and a length of 40 mm. The hollow samples had a 2 mm wall thickness.

After demolding, the samples were wrapped in "paper" soaked with distilled water, placed in a sealed plastic box and kept for about 24 hours at ambient temperature until mechanical testing.

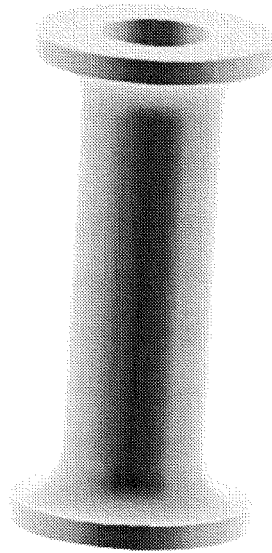


Figure 1: Hollow sample used for mechanical tests

After the mechanical tests, X-ray diffraction was performed on the cement samples to determine the phases in presence. The indexed X-ray spectrum is represented in Figure 2. It shows that a small fraction of non-reacted β -TCP and of non-hydrated brushite (DCP) remains. A typical fracture surface is illustrated in Figure 3 where the precipitated brushite phase is indicated by the needle-shaped crystallites and the residual β -TCP by the small particles. The open porosity, measured on ten samples by Archimede's method, was found to be $37.2 \pm 3.9 \%$.

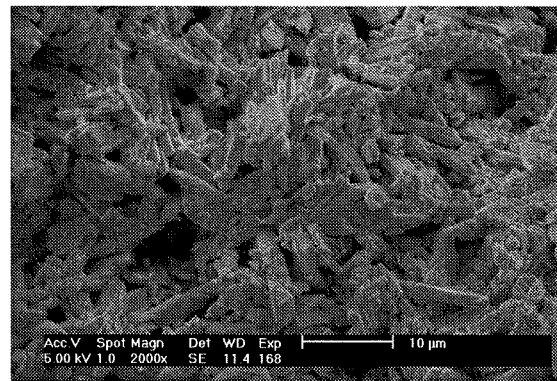
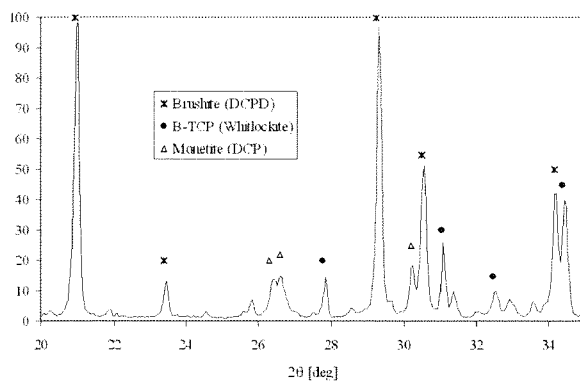
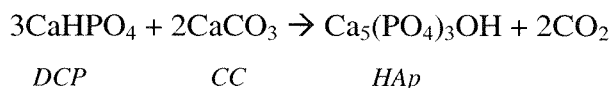


Figure 2 :X-ray diffraction pattern of brushite cement Figure 3 : Needle-shaped brushite crystallites

Hydroxyapatite

A mixture of two calcium phosphate powders in the presence of water was used to obtain a hydroxyapatite cement. The starting powders were monetite (DCP, Merck) and

calcite (CC, Merck) reacting in water to precipitate hydroxyapatite (HAp). The stoichiometric reaction is mentioned below.



Previous internal investigation has shown the importance of using hydroxyapatite seeds (HAp Albright&Wilson, CC:HAp = 2:1, weight basis) and deagglomerating each powder, in order to increase the reaction yield.

A casting process was derived from the traditional "slip casting" process used for shaping ceramic powders. A powder suspension was prepared by means of a dispersing agent. An aqueous polyacrylic acid (PAA) solution was progressively added to the mixture. Residual agglomerates were broken with an ultrasonic horn and bubbles were eliminated under vacuum. Then, the suspension was poured into a plaster mold and the so-called "green body" was obtained after drying. Like for the brushite cement, both hollow and solid samples were prepared. The hollow ones were made with a mold having a flexible silicone core in its center. The cement samples were removed after solidification (a few hours), placed in a sealed plastic box and put in an oven to accelerate the reaction for 48 hours at 75°C in 100% relative humidity.

After the mechanical tests, X-ray diffraction was performed on the cement samples to determine the crystalline phases in presence. The indexed X-ray spectrum is represented in Figure 4. Only the hydroxyapatite phase remains in this cement, which is confirmed by SEM observation. A typical fracture surface is shown on Figure 5 where the fine homogeneous hydroxyapatite structure is visible. The open porosity, measured on ten samples by Archimede's method, was found to be 44.0 % ± 0.6 %.

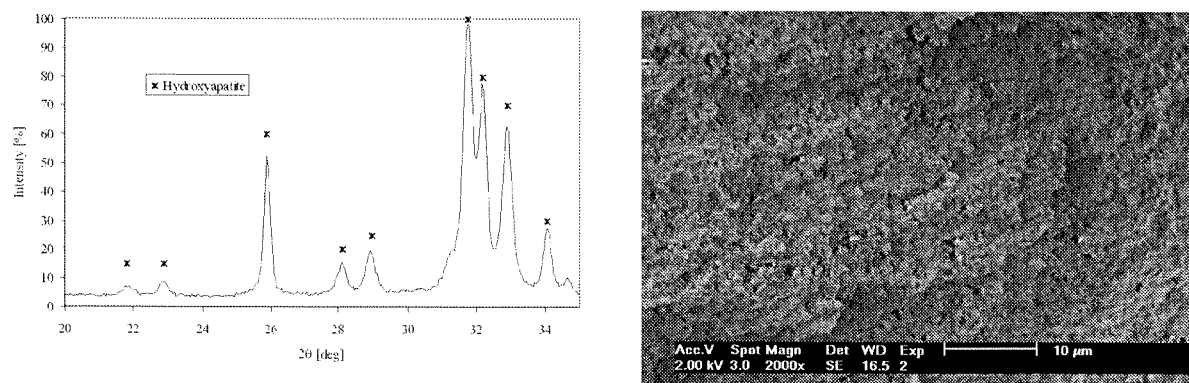


Figure 4 : X-ray diffraction pattern of hydroxyapatite Figure 5 : Smooth and fine hydroxyapatite structure cement

Mechanical tests

An MTS axial-torsional machine was used for all mechanical tests. Compressive, tensile and torsion experiments were performed on the moist brushite and hydroxyapatite samples. A uniaxial extensometer was used for all tensile and compressive tests (Figure 6). A biaxial extensometer was also employed to measure the axial and transverse displacement during axial loading. This transducer allows a direct measurement of Poisson's ratio.

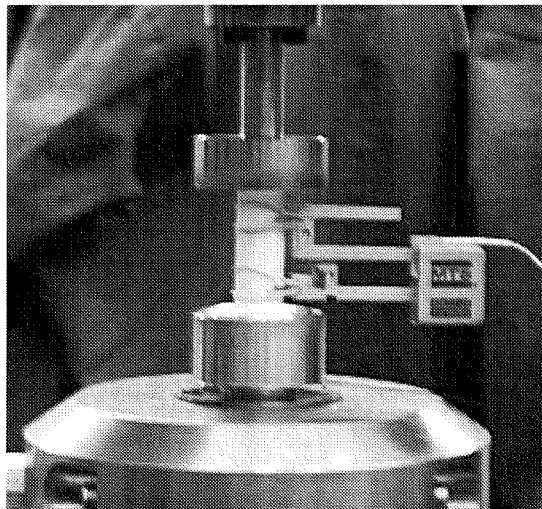


Figure 6 : Gripped sample with ostalloy fixture and uniaxial extensometer

The geometry of revolution of the samples (Figure 1) was selected to permit the combination of different states of stress and reduce stress concentrations at the extremities. To prevent early failure associated with the unavoidable misalignment of standard grips, our samples were aligned along the machine axis using a liquid metal at a temperature of 60°C (Ostalloy 136, Dieco corporate, Ohio, USA) and fixed by cooling the alloy down to room temperature.

If not specified, tests were performed at a $5.5 \cdot 10^{-5} \text{ s}^{-1}$ deformation rate. Each test was repeated five times for each cement. The testing system was controlled in displacement or rotation during all the tests.

Results

Elasticity

The elastic modulus was measured as the tangent at the origin of the stress-strain curves represented in Figure 7. The mean elastic constants and their associated standard deviations (SD) measured for both cements are shown in Table 1.

Tensile, compressive and shear elastic moduli of the hydroxyapatite cement are approximately two times higher than those of brushite. For both cements, the elastic modulus

is higher in the compressive than in the tensile mode. The value of the Poisson's ratio measured with the biaxial extensometer is comparable for both cements.

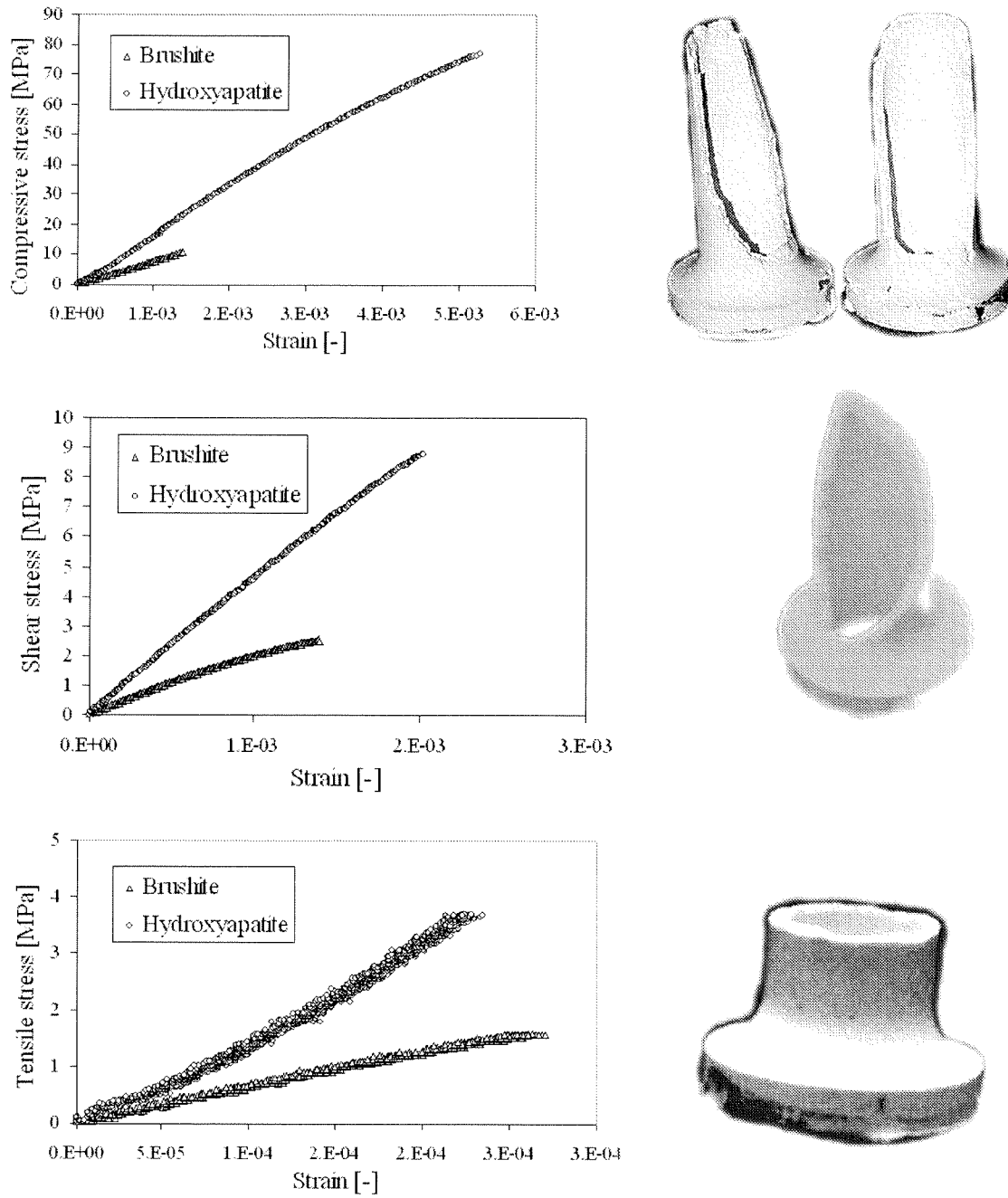


Figure 7: Representative compressive (a), shear (b) and tensile (c) stress-strain curves with related rupture facies of the sample

Table 1 : Brushite and hydroxyapatite mechanical properties

	Tension		Compression			Shear	
	Modulus [GPa]	Strength [MPa]	Modulus [GPa]	Strength [MPa]	Poisson's ratio [-]	Modulus [GPa]	Strength [MPa]
Brushite	6.6 ± 0.4	1.3 ± 0.3	7.9 ± 0.3	10.7 ± 2.0	0.16 ± 0.03	2.7 ± 0.4	2.9 ± 0.4
Hydroxyapatite	12.3 ± 0.8	3.5 ± 0.9	13.5 ± 0.8	75.0 ± 4.2	0.14 ± 0.02	4.8 ± 0.3	9.8 ± 2.6

The variation of the elastic moduli observed as a function of strain rate are represented in Figure 8. Typical stress-strain curves are shown in Figure 9, where a hysteresis can be clearly distinguished.

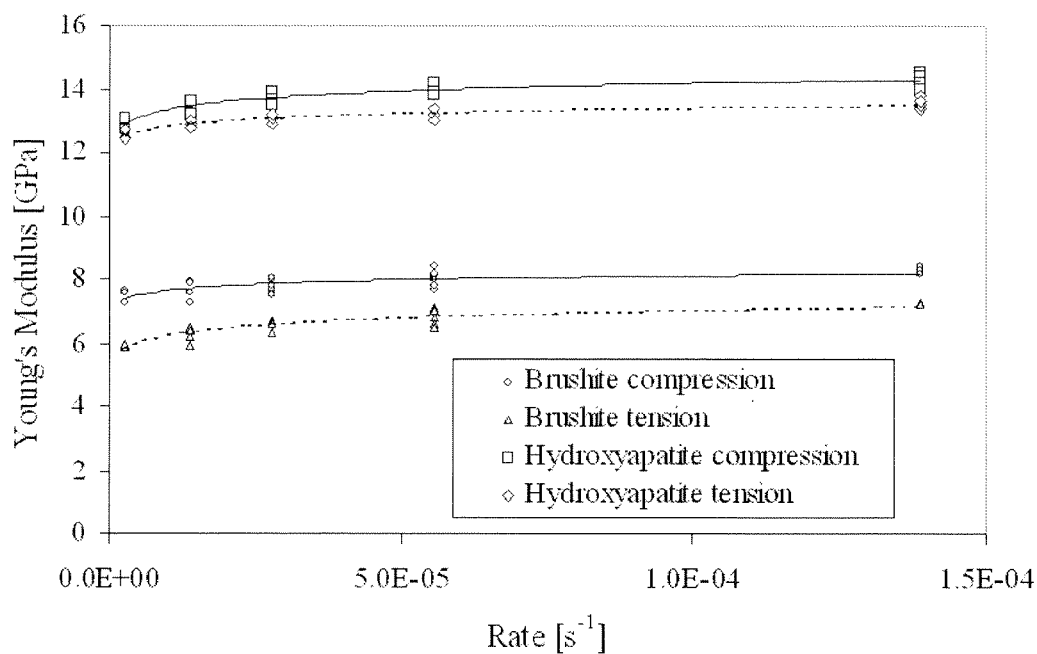


Figure 8 : Rate dependency and differences between compressive and tensile elasticity modulus for both cements

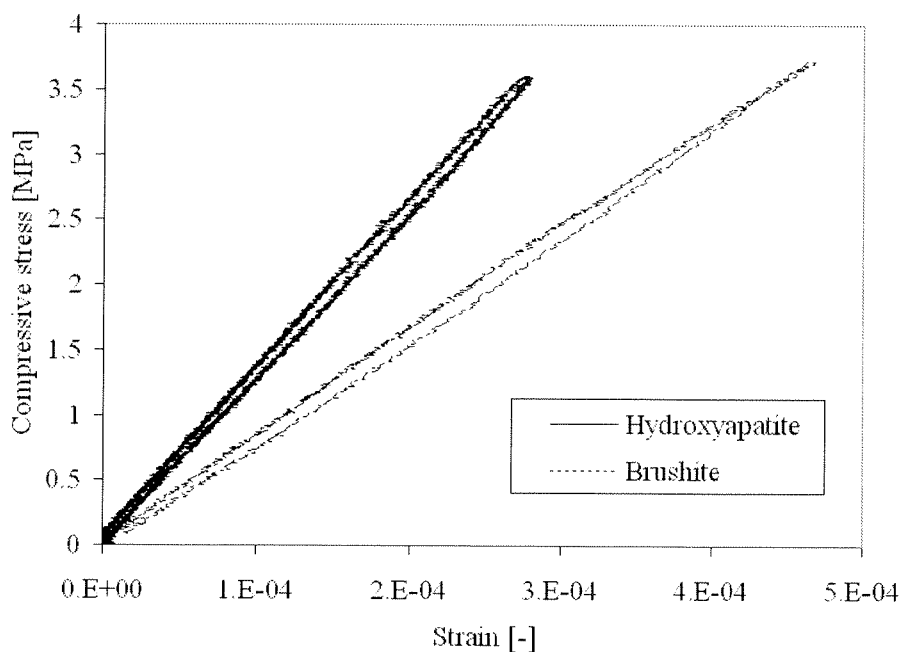


Figure 9 : Representative hysteresis on low compressive loading

Failure

The fracture surfaces as well as representative stress-strain curves are illustrated in Figure 7 for all tests. The fracture surfaces of the sample tested in tension corresponds to a perfect uniaxial tensile rupture and indicates a good sample alignment with the testing machine. The faces of the sample tested in compression corresponds to a $\pi/4$ rupture in shear. The faces of the sample tested in torsion represents a typical helicoidal fracture of a brittle material. The mean strengths and their associated standard deviations (SD) are shown in Table 1 for both cements. The strength of the hydroxyapatite cement is approximately seven times higher in compression, three times higher in tension and in torsion than the corresponding properties of brushite.

Discussion

Elasticity

The difference between tensile and compressive elastic moduli is about 16% for the brushite and 9% for the hydroxyapatite cements. This difference is explained by the presence of microcracks that open in tension and close in compression. Opening the cracks decreases the effective area of the sample and thus the apparent elastic modulus.

Direct measurement of Poisson's ratio by means of a biaxial extensometer revealed very good reproducibility. No significant differences in Poisson's ratio were found between both cements and between the compressive and the tensile loading cases. Nevertheless, indirect calculations of the Poisson's ratio with equation 3 give a poor reproducibility. Calculated Poisson's ratios for the brushite cement are 0.26 ± 0.24 in tension and 0.51 ± 0.23 in compression. For the hydroxyapatite cement, the Poisson's ratios are 0.27 ± 0.12 in tension and 0.49 ± 0.32 in compression. These important errors are explained by the combined dispersion of the elastic moduli and the Lamé shear constant, which were not measured on the same samples. In fact, Poisson's ratio should be evaluated either using a biaxial extensometer, or with a uniaxial one, requiring two tests performed on the same sample (e.g. compression and torsion).

A 2D representation (where the third principal stress σ_3 is set to zero) of the conewise linear elasticity model for both cements in the stress space is shown in Figure 11 for a unit value of the complementary free energy ($W(\boldsymbol{\sigma})=1$). For each loading direction, brushite is always more compliant than hydroxyapatite.

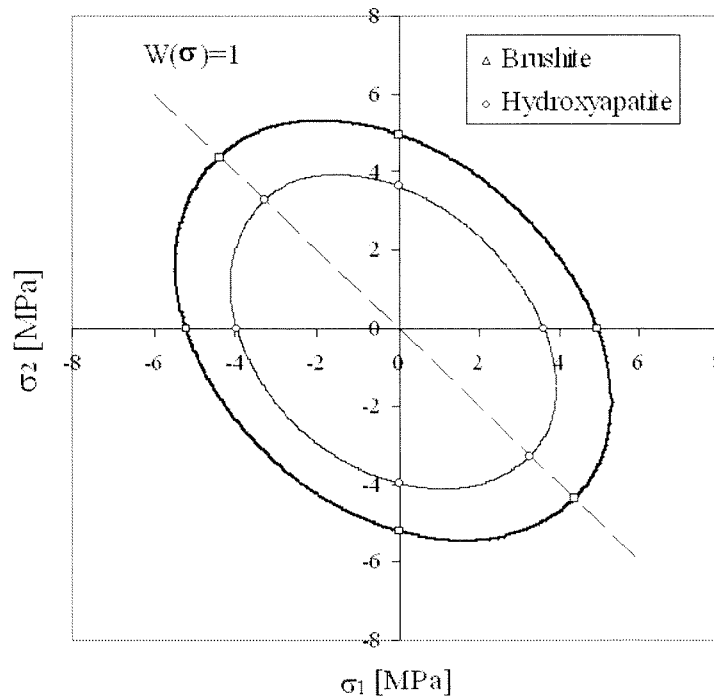


Figure 10 : 2D illustration of the conewise model of both cements in the stress space

As these cements are meant to be used as bone substitutes, their stiffness should ideally match that of human bone. Figure 11 shows that brushite and hydroxyapatite cements exhibit indeed Young's moduli comparable to those of average human cancellous and cortical

bone tissues[18,19,20,21,22,23,24,25]. On the other hand, their stiffness is highly above that of the cancellous bone structure.

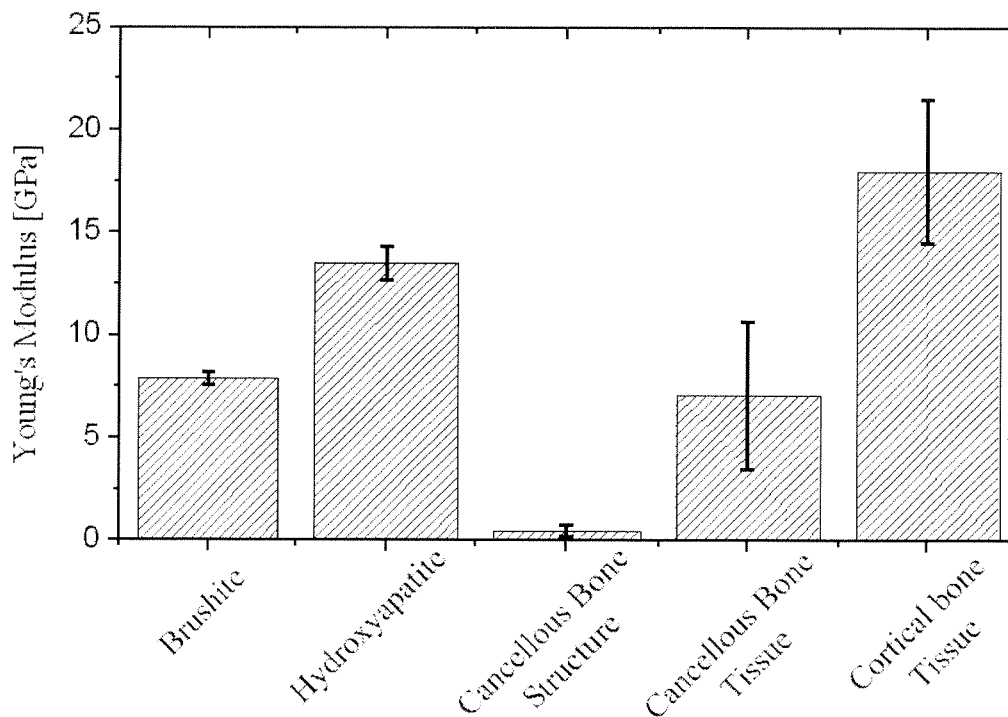


Figure 11 : Young's moduli of both cements with their associated standard deviation compared to mean bone Young's moduli found in the literature [18,19,20,21,22,23,24,25].

Cyclic loading of both cements reveals an increase of the elastic moduli with strain rate (Figure 9). However, at a strain rate of $5 \cdot 10^{-5} \text{ s}^{-1}$ and above, the elastic modulus remains almost constant. Since physiological strain rates for the human body are typically higher than $5 \cdot 10^{-5} \text{ s}^{-1}$, this value represents a good lower limit for mechanical testing of these cements. Hysteresis was observed on both cements (Figure 10), which indicates the occurrence of an energy dissipative process. This time-dependent behavior may be explained by the presence of water in the nanometer size pores of the cements. As the samples are put under stress, the water is forced out of the pores and generates heat by friction with the solid phase.

Failure

Ultimate strengths of the brushite cement measured in tension and compression in this study are comparable to those measured by Bermudez et al. [26]. However, as the experimental conditions and testing methods are not similar, it would be inappropriate to draw conclusions from this comparison. In various studies [26,27,28,29,30], tensile strengths were estimated with a diametral compression test, also known as Brazilian test. Indeed, to avoid systematic overestimation of tensile strength, the Brazilian method requires that the tested material has a compressive strength at least eight times higher than the tensile one [30], which

is not verified for most calcium phosphate cements. Furthermore, the Brazilian method generates a heterogeneous stress state in the sample and depends on sample size as well as precise boundary conditions.

Mechanical strengths measured with the system described in this paper exhibited excellent reproducibility. The standard deviation is lower than that found in the literature for materials of the same class [16, 31]. Furthermore, the obtained fracture surfaces, shown in Figure 7, indicate the homogeneity of the stress state within the sample. The present method is therefore a more accurate and reproducible way to characterize the compressive, tensile and shear strengths of biocements. Nevertheless, such experiments are more time-consuming than Brazilian and standard compressive tests.

Figure 12 represents the mean strengths as well as the fitted Tsai-Wu criterion for a two-dimensional stress state. The failure envelope of the hydroxyapatite cement contains the one of the brushite cement. However, in the tensile region, the difference is less discernable. The lack of experimental strength values in the multiaxial compression quadrant limits the accuracy of the Tsai-Wu criterion in this region. Multiaxial compressive tests may modify the envelope shape in this region, as multiaxial experiments measure material resistance to pore collapsing.

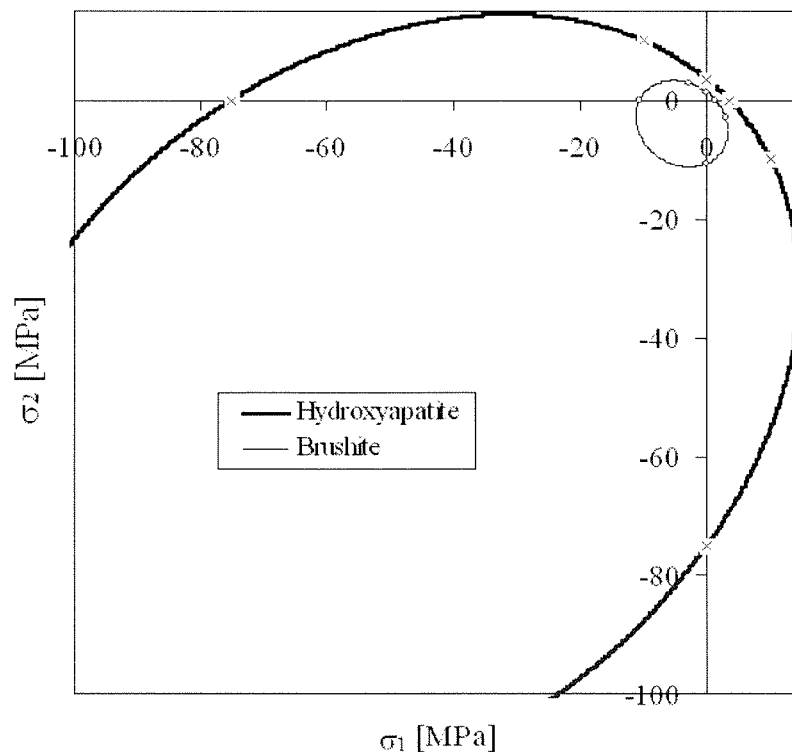


Figure 12 : Isotropic Tsai-Wu criterion for brushite and hydroxyapatite

The ratio between the hydroxyapatite and brushite strengths is 2.7 in tension, 3.4 in shear and 7.0 in compression. These observations are related to the fact that compressive

strengths are more related to the bulk material properties, while microstructural defects have more influences on tensile and shear strengths. Hydroxyapatite has therefore better mechanical properties than brushite. Furthermore, the applicability of these cements for orthopedic implants can be estimated by comparing their strengths with those of human bone (Figure 13). The brushite cement exhibits failure properties comparable or below those of average human cancellous bone structure [18,19,32,33,34] and confirms its indication as a bone filling material. The hydroxyapatite cement has a compressive strength an order of magnitude larger than average human cancellous bone structure, while tensile and shear strengths are comparable. This cement therefore appears more compatible with a multiaxial weight-bearing function in bone substitution.

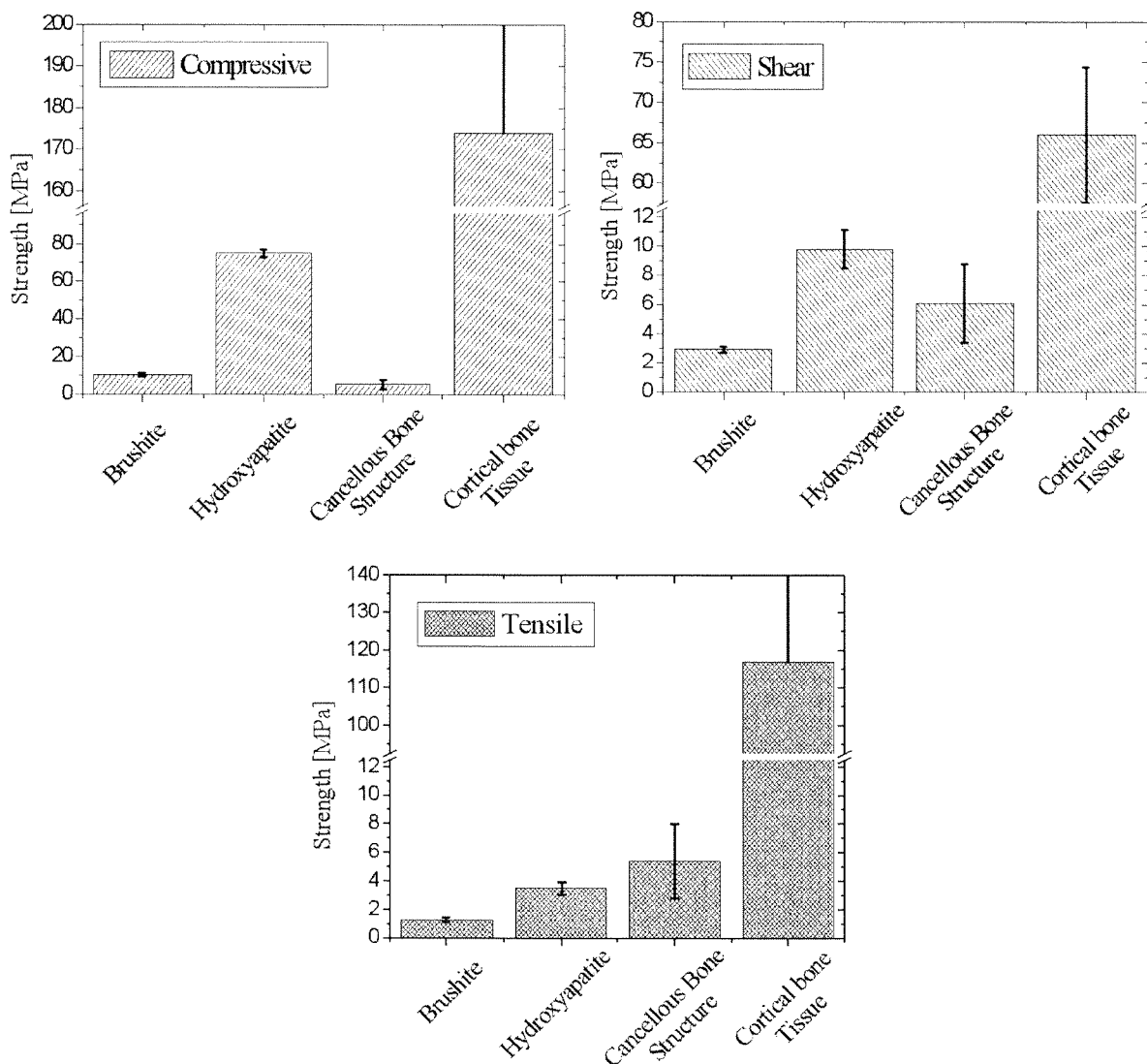


Figure 13 : Compressive (a), shear (b) and tensile (c) strengths of both cements with their associated standard deviation compared to mean bone strengths found in the literature [18,19,32,33,34]

Finally, the degradation of these cements in physiological environment must be considered. Moisture environment induces cement dissolution and precipitation processes. Thus, mechanical strengths of moist cements vary with the immersion time. Bermudez et al. [35] have shown that calcium orthophosphate cements reached their maximum strength within 5 hours after setting. The strength diminished upon further soaking in Ringer's solution at 37 °C. After 10 weeks of soaking, the strength decreased down to 62% of the maximum value. Therefore, biocements should be tested not only immediately after setting, but also after longer time periods in physiological conditions.

Conclusions

Compression, tension and torsion tests together with the use of a conewise linear elasticity model and a Tsai-Wu failure criterion provide an exhaustive characterization of both elastic and failure properties of a brushite and a hydroxyapatite cement. In particular, their elastic behavior and potential failure may be simulated by numerical analysis for various physiological loading conditions. Reproducibility of the mechanical tests is better than that found in the literature. Difference between compressive and tensile Young's modulus were observed that may be attributed to the crack opening and closing. Furthermore, the elastic properties of moist cements are strain rate dependant, indicating interactions between water and cement microstructure. Besides, it was confirmed in this study that the hydroxyapatite cement has a higher potential for weight-bearing functions than brushite.

However, as the mechanical properties of these cements degrade over time in a physiological environment, the inclusion of a controlled macroporosity that allows for early colonization by osteoprogenitor cells may be a suitable strategy for specific clinical applications. Promising cements with controlled macroporosity structures shall be characterized by the presented elasticity and failure assessment method in future studies.

References

- 1 Horii H, Nemat-Nasser S. Overall moduli of solids with microcracks: load induced anisotropy. *J. of the Mechanics and Physics of Solids* 1983;32:155-171.
- 2 Chaboche JL. On the description of damage induced anisotropy and active/passive damage effect. In Ju JW, Krajcinovic D, Schreyer HL (eds). *Damage mechanics in engineering materials*. AMD/ASME 1990:153-166.
- 3 Mazars J, Berthaud Y, Ramtani S. The unilateral behavior of damaged concrete. *Eng. Fract. Mech* 1990;35:629-635.
- 4 Costa-Mattos H, Fremond M, Mamiya EN. A simple model of the mechanical behavior of ceramic-like materials. *Int. J. of Solids and Structures* 1992;29:3185-3200.
- 5 Curnier A, Qi-Chang H, Zysset P. Conewise linear elastic materials. *Journal of Elasticity* 1995;37(1):1-38.
- 6 Hill R. *The mathematical theory of plasticity*. Oxford University Press, London 1950.
- 7 Hoffman O. The brittle strength of materials. *J. Compos. Mater.* 1967;1:200-206.
- 8 Tsai SW, Wu EM. A general theory of strength for anisotropic materials. *J. Compos. Mater.* 1971;5:58-80.
- 9 Priddy TG. A fracture theory for brittle anisotropic materials. *J. Eng. Mater. and Techn.* 1974;91-96.
- 10 Tennyson RC, Elliott WG. Failure analysis of composite laminates including biaxial compression. NASA CR 72192 1983.
- 11 Tennyson RC, Jiang Z. Closure of the cubic tensor polynomial failure surface. *J. Compos. Mater.* 1989; 23:208-231.
- 12 Roschke P, Mascorro E. Failure prediction for cross-rolled beryllium sheet material. *J. Eng. Mater. and Techn.* Transactions of the ASME 1996;118(2):207-212.
- 13 Benzeggagh ML, Khellil K, Chotard T. Experimental determination of Tsai failure tensorial terms F_{ij} for unidirectional composite materials. *Composites Science and Technology* 1995;55(2):145-156.
- 14 Nahla K. Hassan, Mohamed A. Mohamedien, Sami H. Rizkalla. Finite element analysis of bolted connections for PFRP composites. *Composites Part B: Engineering* 1996;27(3-4):339-349.
- 15 Bednar N, Garmestani H. Biaxial testing of high strength carbon fiber composite cylinders for pulsed magnet reinforcement *Composites Part A: Applied Science and Manufacturing* 1999;30(2):147-152.
- 16 Mirtchi AA, Lemaître J, Terao N. Calcium phosphate cements: study of the α -tricalcium phosphate-monocalcium phosphate system. *Biomaterials* 1989;10:634-638.
- 17 Van Landuyt P, Peter B, Beluze L, Lemaître J. Reinforcement of osteosynthesis screws with brushite cement. *Bone* 1999;25 No 2 Supplement: 95S-98S.
- 18 Goulet RW, Goldstein SA, Ciarelli MJ, Kuhn JL, Brown MB, Feldkamp LA. The relationship between the structural and orthogonal compressive properties of trabecular bone. *J Biomech* 1994;27(4):375-389.
- 19 Bruyere-Garnier K. Caractérisation et modélisation mécanique de l'os spongieux humain en relation avec ses propriétés structurales et architecturales. PhD. Thesis 2000. INSA Lyon (France). N° 2000 ISAL 0002.
- 20 Hou FJ, Lang SM, Hoshaw SJ, Reimann DA, Fyhrie DP. Human vertebral body apparent and hard tissue stiffness. *J Biomech* 1998;31(11):1009-1015.
- 21 Runkle JC, Pugh J. The micro-mechanics of cancellous bone. II. Determination of the elastic modulus of individual trabeculae by a buckling analysis. *Bull Hosp Joint Dis* 1975;36(1):2-10.

- 22 Townsend PR, Rose RM, Radin EL. Buckling studies of single human trabeculae. *J Biomech* 1975;8(3-4):199-201.
- 23 Kuhn JL, Goldstein SA, Choi K, London M, Feldkamp LA, Matthews LS. Comparison of the trabecular and cortical tissue moduli from human iliac crests. *J Orthop Res* 1989;7(6):876-884.
- 24 Mente PL, Lewis JL. Young's modulus of trabecular bone tissue. *Trans. 33rd Annu. Meet. Orthop. Res. Soc.* 1987:49.
- 25 Rho JY, Ashman RB, Turner CH. Young's modulus of trabecular and cortical bone material: ultrasonic and microtensile measurements. *J Biomech* 1993;26(2):111-119.
- 26 Bermudez O, Boltong MG, Driessens FCM, Planell JA. Compressive strengths and diametral tensile strength of some calcium-orthophosphate cements: a pilot study. *Mater. Sci. Mater. Med.* 1993;4:389-393.
- 27 Martin RI, Brown PW. Mechanical properties of hydroxyapatite formed at physiological temperature. *Mater. Sci. Mater. Med.* 1995;6:138-143.
- 28 Mirtchi AA, Lemaître J, Munting E. Calcium phosphate cements: effect of fluorides on the setting and hardening of b-tricalcium phosphate-dicalcium phosphate-calcite cements. *Biomaterials.* 1991;12: 505-510.
- 29 Van Landuyt P, Lowe C, Lemaître J. Optimization of setting time and mechanical strength of b-TCP/MCPM cements. *Bioceramics.* 1997;10: 477-480.
- 30 Pittet C, Lemaître J. Mechanical characterisation of brushite cements - A Mohr circles' approach. Submitted to *Journal of Biomedical Materials Research - Applied Biomaterials*
- 31 Driessens FCM, Planell JA, Lopez Valero I, Bermudez Castillo O. Mechanical properties of calcium phosphate cements. In: Doherty PJ et al., editors. *Biomaterial-Tissue Interface. Advances in Biomaterials.* 1992. p. 123-126.
- 32 Rohl L, Larsen E, Linde F, Odgaard A, Jorgensen J. Tensile and compressive properties of cancellous bone. *J Biomech* 1991;24(12):1143-1149.
- 33 Reilly DT, Burstein AH. The elastic and ultimate properties of compact bone tissue. *J Biomech* 1975;8(6):393-405.
- 34 Cowin SC. *Bone mechanics.* Florida: CRC Press, 1991.
- 35 Bermudez O, Boltong MG, Driessens FCM, Planell JA. Optimization of a calcium orthophosphate cement formulation occurring in the combination of monocalcium phosphate monohydrate with calcium oxide. *Journal of Materials Science: Materials in Medicine* 1994;5(2):67-71.

**HYDROXYAPATITE CEMENT SCAFFOLDS WITH
CONTROLLED MACROPOROSITY:
FABRICATION PROTOCOL AND MECHANICAL
PROPERTIES¹****ABSTRACT**

Precipitated hydroxyapatite cement scaffolds with macroporosity of controlled size and shape were successfully built using a solid freeform fabrication process. The negative macroporosity was designed using CAD software and built with an inkjet machine. A slip casting process using a plaster mold was used to precipitate the cement and manufacture samples for mechanical testing. The negative macroporosity was then extracted from the samples using a thermal process.

Compression, tension and torsion tests were completed successfully on the precipitated hydroxyapatite cement samples in moist condition. Elastic and strength properties were measured for these three loading cases and compared to the plain hydroxyapatite cement properties reported in a previous study.

Homogenization theory was applied to estimate the elastic properties of the manufactured scaffolds. A good correlation was obtained between the experimental data and the theory.

¹ *This chapter has been submitted to "Biomaterials" with the title : "Hydroxyapatite cement scaffolds with controlled macroporosity: fabrication protocol and mechanical properties". †E. Charrière, *J. Lemaitre & Ph. Zysset ; Department of Mechanical Engineering, EPFL; †Hôpital Orthopédique de la Suisse Romande ; *Department of Material Sciences, EPFL*

Introduction

Bone regeneration is required in many clinical issues addressed by orthopaedic and dental medicine. The autogenous bone graft is the gold standard, but host tissue is often scarce and can hardly be modeled to the shape required for successful reconstruction.

Alternatives for autogenous bone graft involve biomaterial-cell scaffolds with a number of objectives¹:

1. Provide temporary mechanical support that compares with the combined structural properties of cortical and trabecular bone.
2. Synthesize new bone by intramembranous or endochondral ossification. Favor cell attachment, angiogenesis, synthesis of osteoid and proper tissue mineralization.
3. Degrade in a controlled fashion by fragmenting over a defined period of time into non-toxic molecules which can be metabolized or excreted by the body.
4. Allow the natural process of bone remodeling that adapts the microstructure of the tissue to the loading environment.

Among the existing materials that fulfill at least some of the above requirements (e.g. PLLA¹, PLGA², PPF³, Hap⁴, β -TCP⁵...), microporous calcium phosphate cements are well recognized for their biocompatibility, osteoconduction, resorbability and compressive mechanical properties. The microporosity (diameter < 10 μ m) allows the ions produced during degradation of these cements, to diffuse out of the graft, whereas an open macroporosity (interconnected pores of 200-1000 μ m diameter) of a synthetic graft would be necessary to ensure rapid colonization of the implant with blood vessels and bone cells⁶. It is therefore of considerable interest to manufacture calcium phosphate cements with macroporosity of controlled size and shape in order to enhance osteoconduction without compromising mechanical support.

Standard manufacturing methods like salt leaching^{7,8}, gas foaming^{7,8}, emulsion⁹, do not allow a precise control of pore size, shape and spatial distribution. Furthermore, connectivity obtained with such structures is poor when compared to the volume of the pores¹⁰. These drawbacks lead to low mechanical strengths and prevent the use of these biomaterials in weight bearing areas.

Recent solid freeform fabrication methods allow for a complete control of structural parameters and represent ideal candidates for manufacturing 3D scaffolds, that would be the negative of the desired macroporosity.

Precipitated hydroxyapatite (Hap) cements are an attractive class of microporous calcium phosphate cements, especially in terms of mechanical properties¹¹. Indeed, sintering hydroxyapatite cements will transform them into an even stronger and stiffer ceramic, but with the major inconvenient that they do not degrade. A negative macroporosity should therefore be strong enough to be manipulated but should also be easily removable using a low temperature process to avoid sintering of the hydroxyapatite phase.

The main goal of this work was to build precipitated hydroxyapatite cement scaffolds with a periodic macroporosity of controlled size and shape and to quantify their mechanical properties in compression, tension and shear. A second goal of this work was to find a reliable model for prediction of the elastic properties of the generated scaffolds.

Materials and methods

Design of the negative macroporosity

A periodic, orthogonal array of cylinders with a diameter of 1 mm and variable spacing was designed (Figure 1). The external shape is a cylinder of 18x18x30mm, that can be fabricated with the same mold and compared to plain hydroxyapatite samples tested in a previous study¹². The unit cell or representative volume element (RVE) of the material with the designed macroporosity is represented as a binary digital image in Figure 2. The aspect ratio was defined as the diameter divided by spacing and the corresponding volume fraction was calculated from the relative number of voxels that belonged to the solid part of the scaffold.

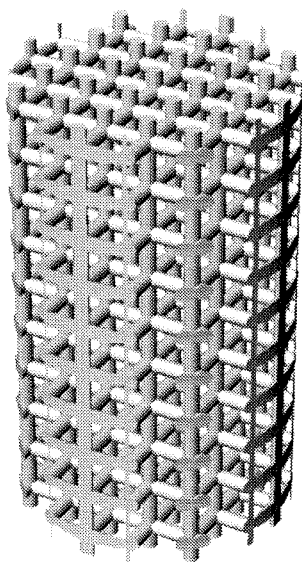


Figure 1 : Negative macroporosity for a cylindrical sample.

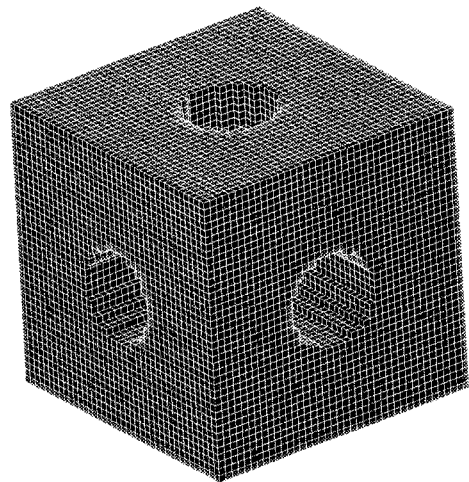


Figure 2 : Digital image of a representative volume element (RVE) of the designed scaffold.

Manufacturing

It is difficult, if not impossible, to build interconnected rod structures with 1mm diameter using classical subtractive fabrication methods. Solid freeform fabrication (SFF) methods can build structures of a wide range of geometric complexity without the need for an elaborate process. Furthermore, SFF methods support an increasing variety of building materials.

The choice of the most appropriate SFF method depends, for our application, on the accuracy requirement and of the admissible materials. In order to build cylinders with 1mm diameter, a resolution of about 50 μ m in all directions is mandatory. In addition, the support material used by some SFF methods must be removed without altering the designed structure. Finally, for our molding strategy, the building material must also be removed without damaging (mechanically or chemically) the hydroxyapatite cement. Among existing systems, stereolithography (SLA), fuse deposition modelling (FDM), and inkjet (IJ) are possible choices for such applications.

SLA systems use thermosets resins: such materials are very difficult to remove either chemically or thermally without damaging or sintering the hydroxyapatite cement. FDM systems allow the use of wax materials, which are easily removed with a low temperature process. Unfortunately, the resolution of parts made out of this process is currently too coarse. The IJ systems are able to build structures with high resolution and accuracy. They use thermoplastics as building materials that can be dissolved or melted at low temperature. Moreover, they use support materials based on wax that can be removed very easily. This last method was retained for manufacturing the macroporous hydroxyapatite scaffolds in this study.

In order to test the feasibility of the selected method, a negative macroporosity with an aspect ratio of 1/3 was built with 6x6x10 RVEs (Figure 3).

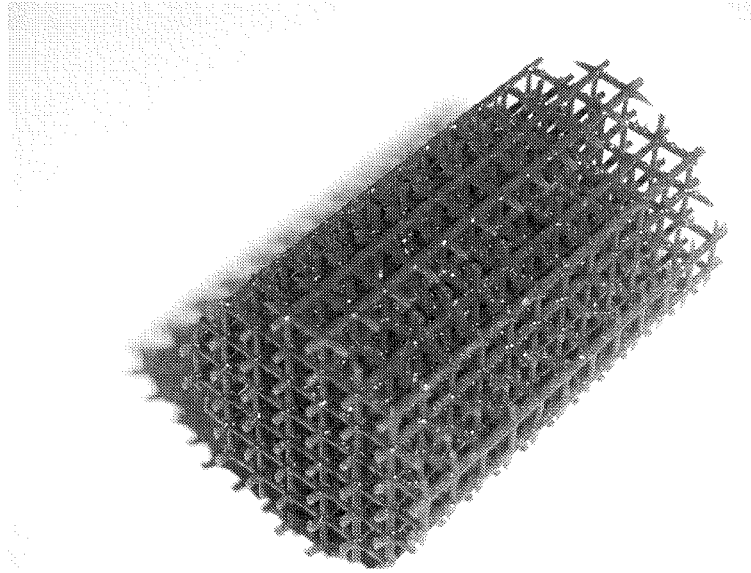


Figure 3 : Thermoplastic negative macroporosity made with an inkjet technology.

A slip casting process using a plaster mold was then applied to a dicalcium phosphate and calcite mixture with a dispersing agent in order to obtain hydroxyapatite cement. The complete protocol of the cement fabrication was previously published¹². The mixture was then poured in a mold containing the negative macroporosity (Figure 4).

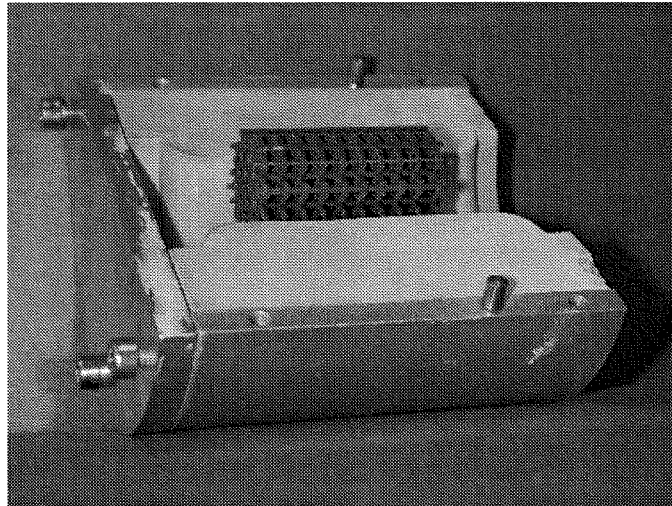


Figure 4 : Negative macroporosity viewed in a half-mold

The demolding process of the green body was made after 6 hours and the sample was put in a 100% moisture environment during two weeks. The green body was then completely converted into hydroxyapatite by heating it at 90°C for one day (which is different from the plain Hap protocol and might give straight differences in the results). During this process, the thermoplastic negative macroporosity melted and was completely eliminated from the sample. The obtained structure with a macroscopic volume fraction of 0.78 (without the

microporosity) is represented in Figure 5. The global volume fraction (including the microporosity) is 0.44.

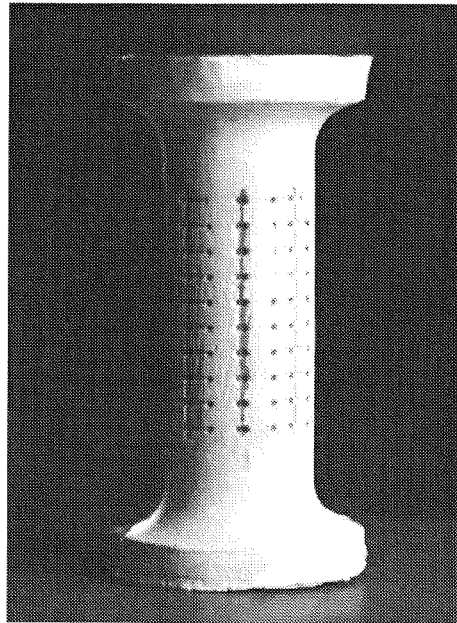


Figure 5 : Hydroxyapatite cement sample with the designed macroporosity.

Mechanical tests

An MTS axial-torsional servohydraulic system was used for all mechanical tests. The geometry of revolution of the samples (Figure 5) was selected to allow the application of compressive, tensile and torsional loading and reduce stress concentrations at the extremities. To prevent early failure associated with the unavoidable misalignment of standard grips, our samples were aligned along the machine axis using a liquid metal at a temperature of 60°C (Ostalloy 136, Dieco corporate, Ohio, USA) and fixed by cooling the alloy down to room temperature.

Compressive, tensile and torsion tests were performed on the moist hydroxyapatite samples under displacement or rotation control. In a first step, a biaxial extensometer was mounted on the specimens to measure the axial and transverse displacement during non destructive axial loading. This step allows direct calculation of Young's modulus and Poisson's ratio. In a second step, a uniaxial extensometer was used for monotonic axial loading up to failure of the specimens (Figure 6). Deformation rate was $5.5 \cdot 10^{-5} \text{ s}^{-1}$ for all tests.

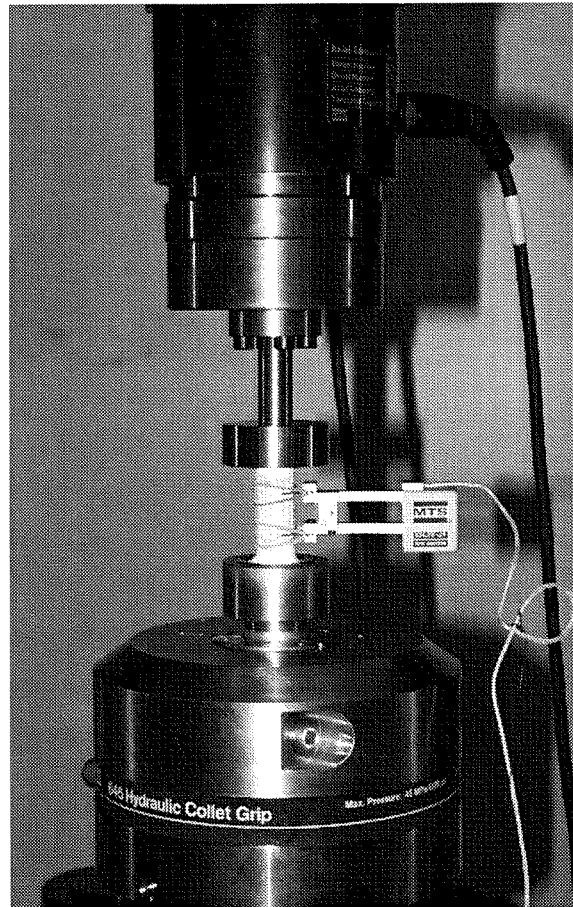


Figure 6 : Grippped sample with Ostalloy fixture and uniaxial extensometer

Homogenization

Since elastic properties of the scaffolds are essential for mechanical support, bone formation and bone remodeling, an appropriate model for their prediction is needed.

In principle, it is possible to compute the properties of these scaffolds with a standard finite element approach. However, the periodic nature of the scaffolds suggests the use of the efficient homogeneization theory to compute their effective elastic properties. A displacement based digital finite element approach was used to solve the 6 canonical homogenization equations with periodic boundary conditions¹³.

Representative volume elements with aspect ratios of 0.05, 0.133, 0.33, 0.5, 0.66, 0.8 and 1 were analyzed. They correspond to volume fractions of 0.007, 0.036, 0.206, 0.403, 0.623, 0.779 and 0.943 respectively. A custom- solid modeling and mesh generation program was used to generate the finite element mesh for each case (Figure 7). The effective elasticity tensors were computed for each mesh using custom software.

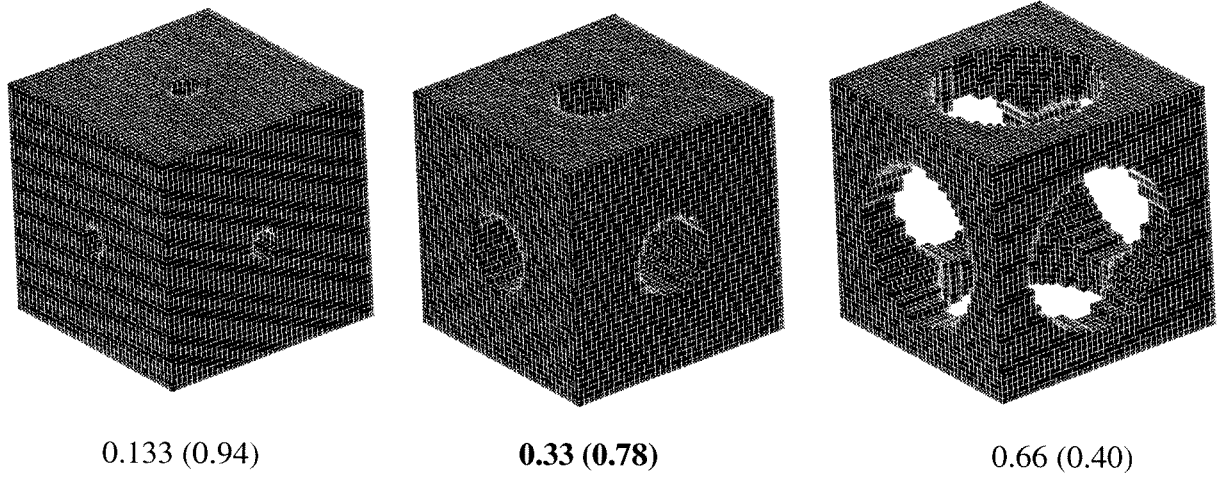


Figure 7 : Variation of the aspect ratio for a 40x40x40 hexahedral elements mesh. The corresponding volume fraction is indicated inside the bracket. The 0.33 aspect ratio mesh corresponds to the built scaffold.

For linear anisotropic materials, the number of independent elastic constants of the fourth order elasticity tensor \mathbf{S}_0 is 21. For materials that exhibit cubic symmetry such as the RVEs designed in this study, the numbers of independent elastic constants of \mathbf{S}_0 is decreased to 3. In fact, \mathbf{S}_0 can be expressed as:

$$\mathbf{S}_0 = \begin{bmatrix} \lambda_1 & \lambda_2 & \lambda_2 & 0 & 0 & 0 \\ \lambda_2 & \lambda_1 & \lambda_2 & 0 & 0 & 0 \\ \lambda_2 & \lambda_2 & \lambda_1 & 0 & 0 & 0 \\ 0 & 0 & 0 & 2\mu & 0 & 0 \\ 0 & 0 & 0 & 0 & 2\mu & 0 \\ 0 & 0 & 0 & 0 & 0 & 2\mu \end{bmatrix} \quad \text{Equation 1}$$

and its inverse by:

$$\mathbf{S}_0^{-1} = \begin{bmatrix} \frac{1}{\varepsilon} & -\frac{\nu}{\varepsilon} & -\frac{\nu}{\varepsilon} & 0 & 0 & 0 \\ -\frac{\nu}{\varepsilon} & \frac{1}{\varepsilon} & -\frac{\nu}{\varepsilon} & 0 & 0 & 0 \\ -\frac{\nu}{\varepsilon} & -\frac{\nu}{\varepsilon} & \frac{1}{\varepsilon} & 0 & 0 & 0 \\ 0 & 0 & 0 & \frac{1}{2\mu} & 0 & 0 \\ 0 & 0 & 0 & 0 & \frac{1}{2\mu} & 0 \\ 0 & 0 & 0 & 0 & 0 & \frac{1}{2\mu} \end{bmatrix} \quad \text{Equation 2}$$

with the following relationships between Young's modulus ε , Poisson's ratio ν and the stiffnesses λ_1, λ_2 :

$$\varepsilon = \frac{\lambda_1^2 + \lambda_1\lambda_2 - 2\lambda_2^2}{\lambda_1 + \lambda_2} \quad \text{Equation 3}$$

$$\nu = \frac{\lambda_2}{\lambda_1 + \lambda_2} \quad \text{Equation 4}$$

In the case of cubic symmetry, the Lamé shear constant μ cannot be described by a function of ϵ and ν (as it is in the isotropic case), and represents the third independent parameter.

Results

Manufacturing

Among the 15 samples prepared, two samples broke during the unmolding process while one sample broke during the thermal treatment. The total number of successfully built samples was therefore 12.

Mechanical tests

Four samples were used for each of the compressive, tensile and torsion tests. The mean elastic constants and their associated standard deviations (SD) are reported in Table 1 and compared to the elastic properties of the plain hydroxyapatite cement (without macroporosity). Tensile, compressive and shear elastic moduli of the macroporous Hap cement are approximately two times lower than those of plain hydroxyapatite. Poisson's ratio is comparable for the plain and the macroporous cements.

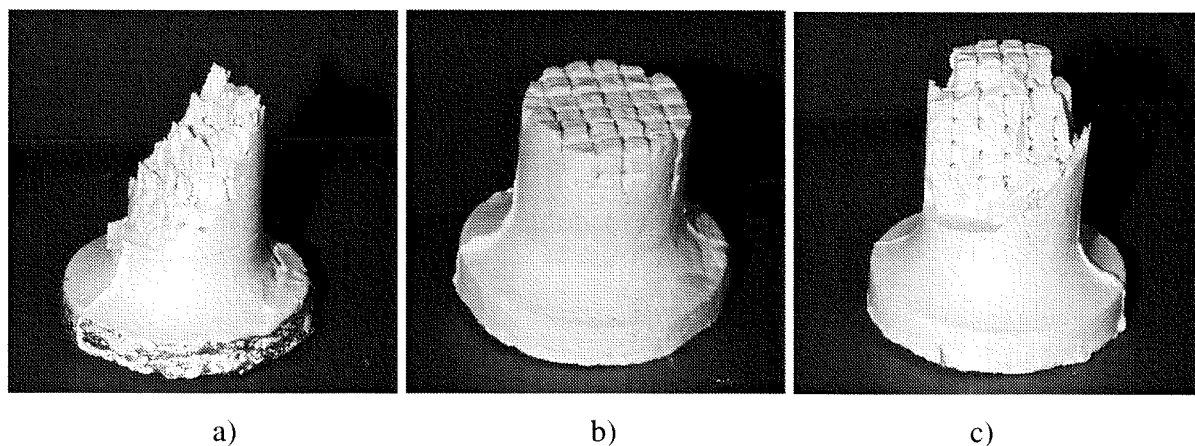


Figure 8 : Characteristic fracture surfaces of the samples tested in compression a), tension b) and torsion c).

Table 1 : Mechanical properties of the macroporous and plain hydroxyapatite cements. The data of the plain hydroxyapatite cement were taken from a previous study¹².

	Tension		Compression			Shear	
	Modulus	Strength	Modulus	Strength	Poisson's	Modulus	Strength
	[GPa]	[MPa]	[GPa]	[MPa]	ratio [-]	[GPa]	[MPa]
Macroporous Hap	7.4 ± 0.6	0.7 ± 0.1	7.6 ± 1.2	12.5 ± 4.6	0.15 ± 0.02	2.6 ± 0.1	1.3 ± 0.2
Plain Hap	12.3 ± 0.8	3.5 ± 0.9	13.5 ± 0.8	75.0 ± 4.2	0.14 ± 0.02	4.8 ± 0.3	9.8 ± 2.6

The representative fracture surfaces are illustrated in Figure 8 for all tests. The fracture surface of the sample tested in tension corresponds to a perfect uniaxial tensile rupture and indicates a good sample alignment with the testing system. The rupture faces of the sample tested in compression correspond to a $\pi/4$ rupture in shear. The faces of the sample tested in torsion represent a typical helicoidal fracture of a brittle material. The mean strengths and their associated standard deviations (SD) are also shown in Table 1 for both macroporous and plain cements. The strength of the macroporous hydroxyapatite cement is approximately five times lower in compression and in tension and seven times lower in torsion than the corresponding properties of the plain hydroxyapatite.

Homogenization

Based on previous characterization of the isotropic elastic properties of the plain hydroxyapatite cement, homogenization analysis provided the three elastic constants of the cubic RVEs as a function of volume fraction (Figure 10). A good way to visualize the elastic behavior of an anisotropic material is to express the elongation modulus as a function of the orientation in material space. This elongation modulus is defined as

$$K(\mathbf{n}) = \mathbf{N} : \mathbf{S}_0 \mathbf{N} \quad \text{Equation 5}$$

where \mathbf{S}_0 is the fourth rank stiffness tensor and $\mathbf{N} = \mathbf{n} \otimes \mathbf{n}$ is the dyadic product of the uniaxial elongation direction \mathbf{n} with itself.

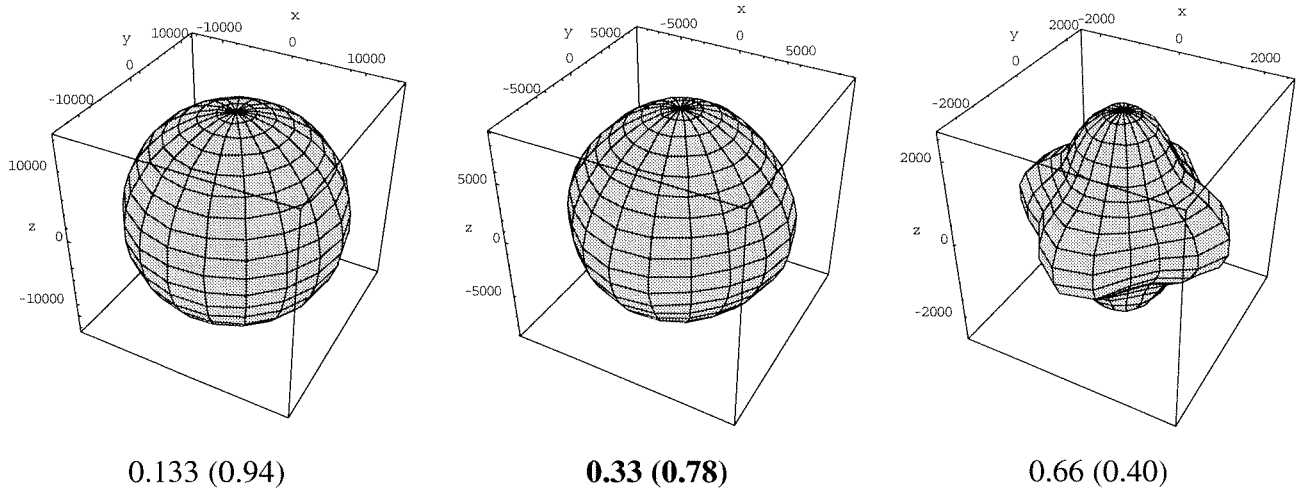


Figure 9 : Predicted elongation modulus as a function of the aspect ratio (computed using the homogenization program). The corresponding volume fraction is indicated inside the bracket. The X,Y,Z axis correspond to the principal directions in the RVE. The 0.33 aspect ratio mesh corresponds to the built structure. The scales of the X,Y,Z axis are not the same in the three graphs.

The elastic modulus of the designed hydroxyapatite scaffold increased as a power function of aspect ratio between 0 and 13 GPa, the modulus of the plain hydroxyapatite cement¹². The other coefficients also increased as power functions.

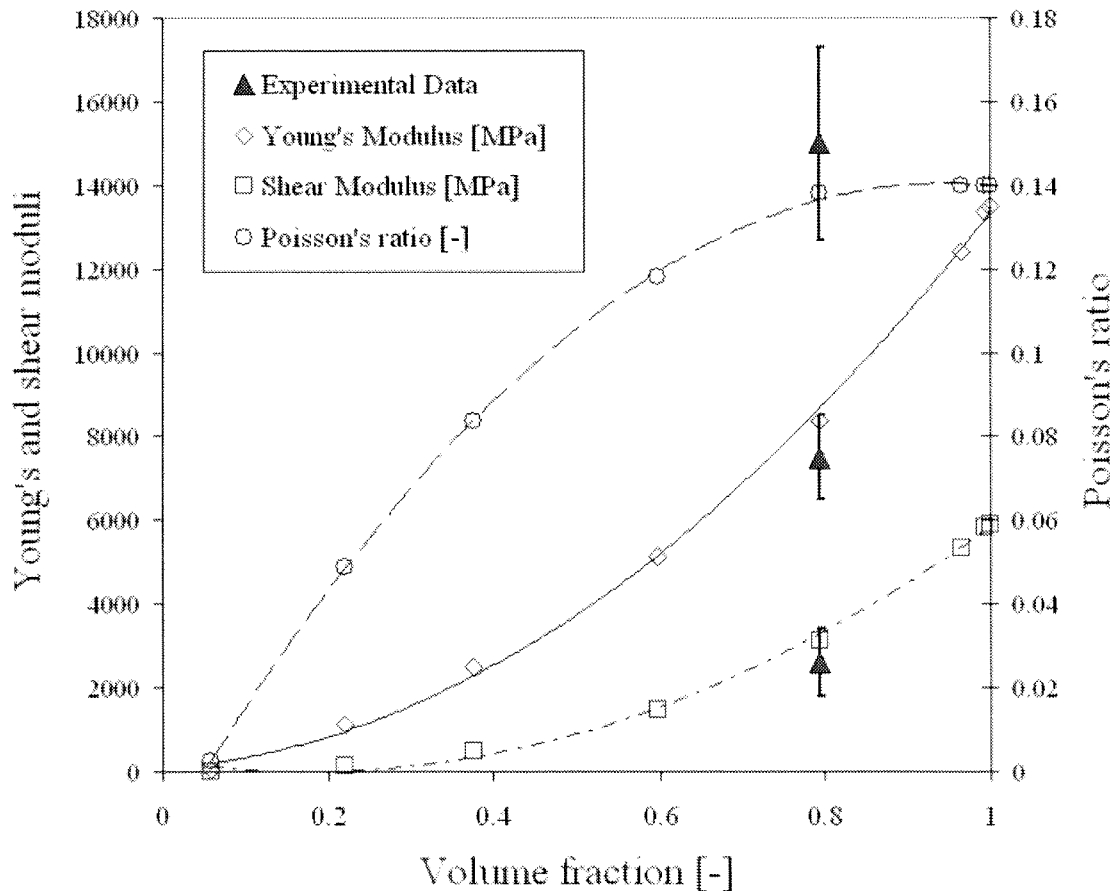


Figure 10 : Elastic constants as a function of volume fraction of the RVE.

Discussion

Feasibility of manufacturing precipitated hydroxyapatite cement scaffolds with a cylindrical porosity of 1 mm diameter was demonstrated in this study. No distortion or shrinkage of the pore geometry was observed during the manufacturing process. The pores were free of the thermoplastic SFF material and remained interconnected. Difficulties occurred when removing the samples out of the mold. Among the fifteen prepared samples, two of them broke during the unmolding process of the green body. This was mainly due to shear stresses that acted on the green body when removing a half-mold.

The resolution and the accuracy of the negative macroporosity are limited by the selected SFF method, but there are also restrictions in sample size due to building material fragility. Two 10x10x10mm cubic samples with a cylindrical porosity of 500 μm in diameter were manufactured with the same inkjet method. However, we were not successful in building an 18x18x30mm cylindrical sample with a similar porosity of 500 μm in diameter. The thermoplastic part broke during the wax removal process.

Using a SFF method to build macroporous scaffolds for bone reconstruction has key advantages compared to standard fabrication tools. First, it allows to build grafts with an arbitrary external shape that can be generated from patient based clinical imaging data (Hollister et al.^{14,15}). Second, according to the results of the present work, the elastic properties of the grafts can be controlled using volume fraction as well as anisotropy of the macroporosity.

The standard deviations of Young's moduli, shear moduli and Poisson's ratios are higher for the macroporous hydroxyapatite than for the plain hydroxyapatite plain cement. This is a straight consequence of the local defects associated with the multistep process adopted for manufacturing of the macroporosity.

The Young's modulus and shear modulus of the macroporous hydroxyapatite scaffold lay between those of cancellous bone structure and cortical bone tissue (Figure 11).

Considering strength, the macroporous hydroxyapatite cement has substantially lower properties than the plain material (Figure 12). When compared to human cancellous bone, the macroporous cement exhibits poor tensile and shear strength. However, the compressive strength remains sufficient to ensure primary stabilization in weight bearing areas dominated by a compressive loading mode.

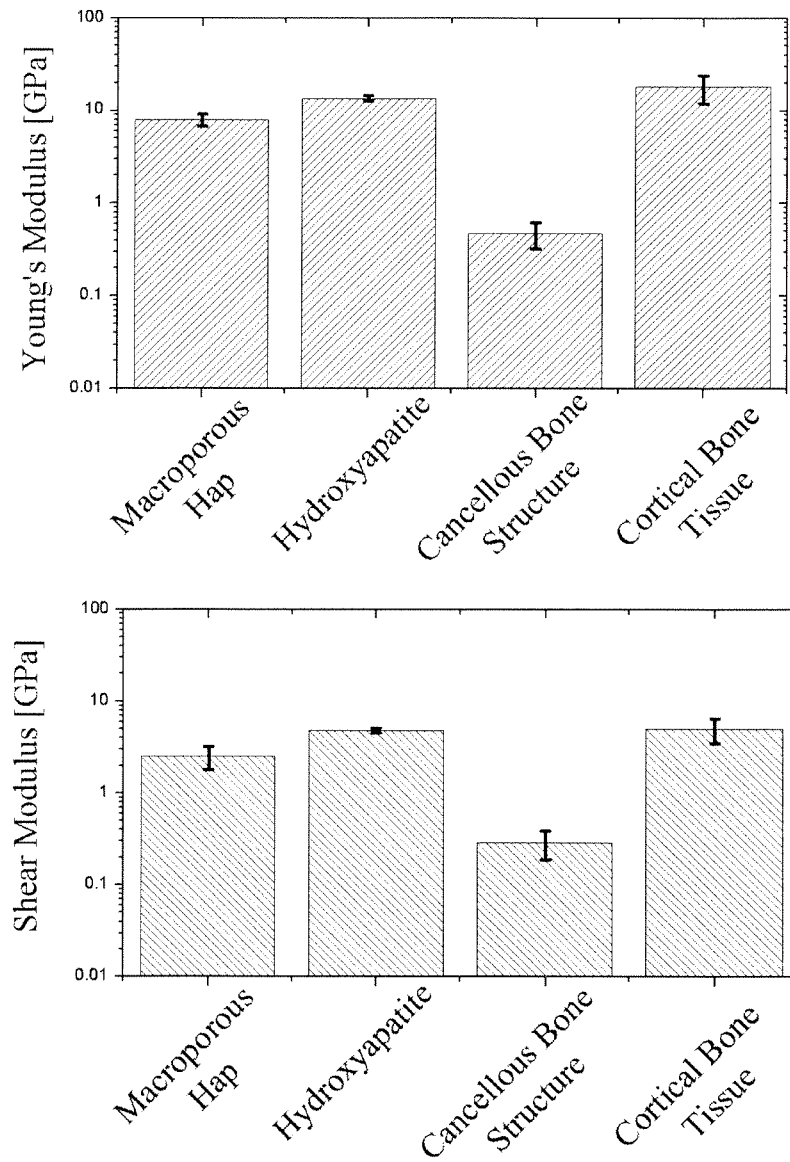


Figure 11 : Young's moduli and shear moduli of the macroporous and plain hydroxyapatite cements compared to those of human bone.^{16,17,18,19,20,21,22,23}

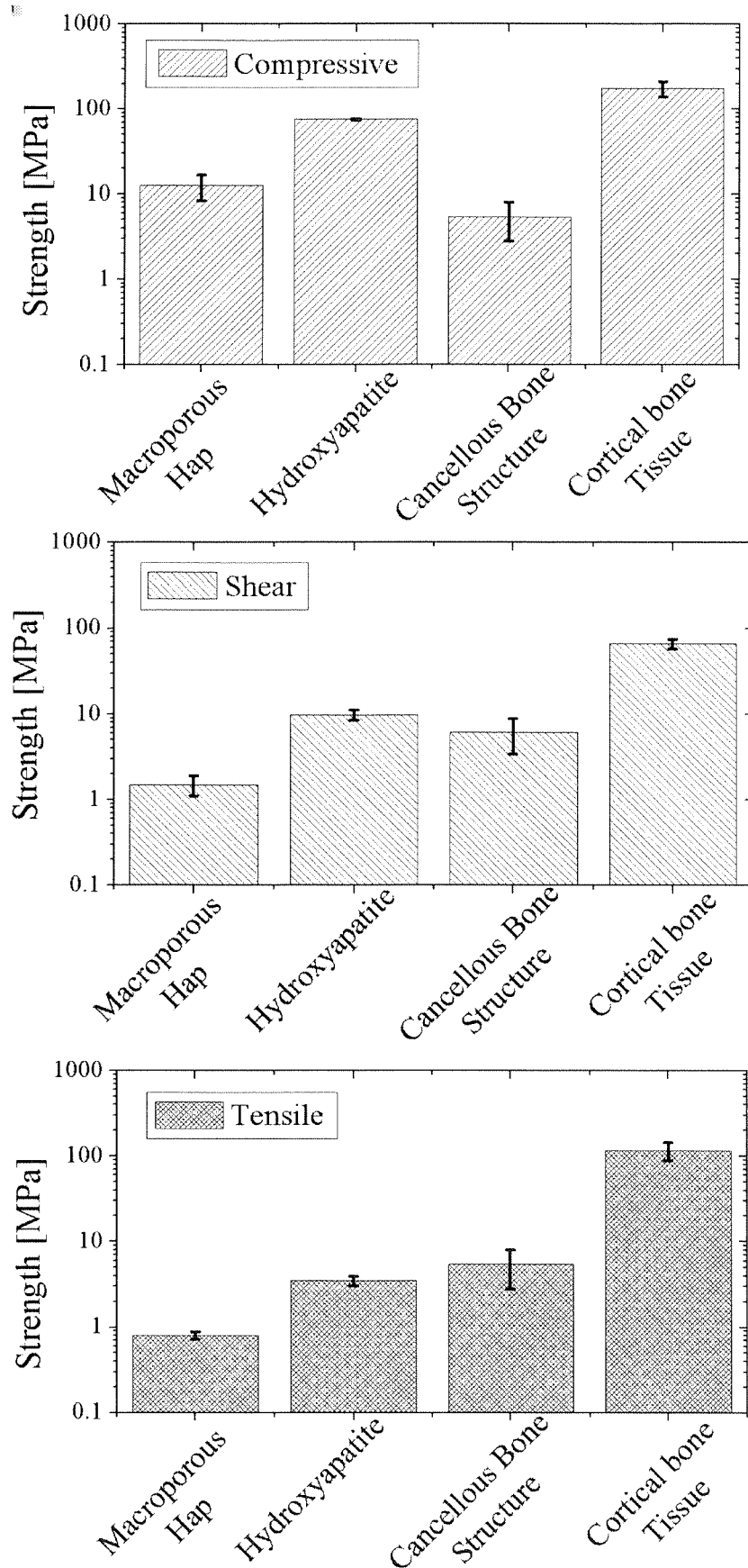


Figure 12 : Compressive, tensile and shear strength of the macroporous and plain hydroxyapatite compared to the corresponding bone strength ^{16,17,24,25,26}.

As we used only six RVEs in the transversal direction of the samples, the continuum assumption underlying the use of homogenization analysis according to which the size of the pores is small when compared to the size of the sample is not fulfilled¹³. However, despite this theoretical limitation, the experimental data (Young's modulus, shear modulus and Poisson's ratio) are close to the homogenization results. The applied homogenization method appears therefore to be a low cost and reliable method to estimate the effective elastic properties of periodic scaffolds with a complex macroporosity.

To conclude, a new method to manufacture hydroxyapatite scaffolds with controlled porosity and predictable elastic properties was developed. Since precipitated hydroxyapatite cements are biocompatible, biodegradable and osteoconductive, the manufactured scaffolds represent a biomaterial of choice for bone reconstruction in weight bearing areas dominated by compressive stresses. Future studies will focus on the behaviour of these biomaterials *in vivo* aiming at finding new strategies to enhance their tensile and shear strength.

References

- 1 Mikos AG, Thorsen AJ, Czerwonka LA et al. Preparation and characterization of poly(L-lactic acid) foams. *Polymer* 1994;35:1068-1077.
- 2 Mikos AG, Sarakinos G, Leite SM, Vacanti JP, Langer R. Laminated three-dimensional biodegradable foams for use in tissue engineering. *Biomaterials* 1993;14:323-330.
- 3 Yaszemski MJ, Payne RG, Hayes WC, Langer RS, Aufdemorte TB, Mikos AG. The ingrowth of new bone tissue into and initial mechanical properties of a degrading polymeric composite scaffold. *Tissue Engng* 1995;1:42-44.
- 4 LeGeros RZ. In: Brown PW, Constantz B, eds. *Hydroxyapatite and related materials*. Boca Raton: CRC Press, 1994:3-28.
- 5 Egli PS, Muller W, Schenk RK. Porous hydroxyapatite and tricalcium phosphate cylinders with two different pore size ranges implanted in the cancellous bone of rabbits. *Clin Orthop Rel Res* 1988;232:127-138.
- 6 Gauthier O, Bouler JM, Aguado E, Pilet P, Daculsi G. Macroporous biphasic calcium phosphate ceramics: influence of macropore diameter and macroporosity percentage on bone ingrowth. *Biomaterials* 1998;19(1-3):133-9.
- 7 Yoon JJ, Park TG. Degradation behaviors of biodegradable macroporous scaffolds prepared by gas foaming of effervescent salts. *J Biomed Mater Res* 2001;55(3):401-8.
- 8 Harris LD, Kim BS, Mooney DJ. Open pore biodegradable matrices formed with gas foaming. *J Biomed Mater Res* 1998;42(3):396-402.
- 9 Ambrosio AM, Sahota JS, Khan Y, Laurencin CT. A novel amorphous calcium phosphate polymer ceramic for bone repair: I. Synthesis and characterization. *J Biomed Mater Res* 2001 May 1;58(3):295-301.
- 10 Bouler JM, Trecant M, Delecrin J, Royer J, Passuti N, Daculsi G. Macroporous biphasic calcium phosphate ceramics: influence of five synthesis parameters on compressive strength. *J Biomed Mater Res* 1996;32(4):603-9.
- 11 Charrière E., Terrazzoni S., Pittet C., Mordasini P., Dutoit M., Lemaître J., Zysset P.K. Mechanical characterization of brushite and hydroxyapatite cements. *Biomaterials* 2001;22(21):2937-2945.
- 12 Charrière E., Terrazzoni S., Pittet C., Mordasini P., Dutoit M., Lemaître J., Zysset P.K. Mechanical characterization of brushite and hydroxyapatite cements. *Biomaterials* 2001;22(21):2937-2945.
- 13 Hollister S.J., Kikuchi N. A comparison of homogenization and standard mechanics analyses for periodic porous composites. *Computational Mechanics* 1992;10:73-95.
- 14 Hollister, S.J., Chu, T.M., Guldberg, R.E., Zysset, P.K., Levy, R.A., Halloran, J.W. & Feinberg, S.E. "Image based design and manufacture of scaffolds for bone reconstruction" in Pedersen, P. and Bendsoe, M. Eds, *IUTAM Synthesis in Biosolid Mechanics*, Kluwer Press, 1998.
- 15 Hollister S.J., Zysset P.K., Guldberg R.E, Chu T.M. and Halloran J.W., "Engineering Microstructures to Evaluate and Replace Trabecular Bone" in Majumdar S. and Bay B. Eds, *Non invasive Assessment of Trabecular Bone Architecture and Competence of Bone*, Kluwer Academic/Plenum Publishers, New York, in press.

- 16 Goulet RW, Goldstein SA, Ciarelli MJ, Kuhn JL, Brown MB, Feldkamp LA. The relationship between the structural and orthogonal compressive properties of trabecular bone. *J Biomech* 1994;27(4):375-389.
- 17 Bruyere-Garnier K. Caractérisation et modélisation mécanique de l'os spongieux humain en relation avec ses propriétés structurales et architecturales. PhD. Thesis 2000. INSA Lyon (France). N° 2000 ISAL 0002.
- 18 Hou FJ, Lang SM, Hoshaw SJ, Reimann DA, Fyhrie DP. Human vertebral body apparent and hard tissue stiffness. *J Biomech* 1998;31(11):1009-1015.
- 19 Runkle JC, Pugh J. The micro-mechanics of cancellous bone. II. Determination of the elastic modulus of individual trabeculae by a buckling analysis. *Bull Hosp Joint Dis* 1975;36(1):2-10.
- 20 Townsend PR, Rose RM, Radin EL. Buckling studies of single human trabeculae. *J Biomech* 1975;8(3-4):199-201.
- 21 Kuhn JL, Goldstein SA, Choi K, London M, Feldkamp LA, Matthews LS. Comparison of the trabecular and cortical tissue moduli from human iliac crests. *J Orthop Res* 1989;7(6):876-884.
- 22 Mente PL, Lewis JL. Young's modulus of trabecular bone tissue. *Trans. 33rd Annu. Meet. Orthop. Res. Soc.* 1987:49.
- 23 Rho JY, Ashman RB, Turner CH. Young's modulus of trabecular and cortical bone material: ultrasonic and microtensile measurements. *J Biomech* 1993;26(2):111-119.
- 24 Rohl L, Larsen E, Linde F, Odgaard A, Jorgensen J. Tensile and compressive properties of cancellous bone. *J Biomech* 1991;24(12):1143-1149.
- 25 Reilly DT, Burstein AH. The elastic and ultimate properties of compact bone tissue. *J Biomech* 1975;8(6):393-405.
- 26 Cowin SC. *Bone mechanics*. Florida: CRC Press, 1991.

**COMPLIANCE OF THE L5-S1 SPINAL UNIT:
A COMPARATIVE STUDY BETWEEN AN
UNCONSTRAINED AND A SEMI-
CONSTRAINED SYSTEM¹****ABSTRACT**

Study design : A comparison between an unconstrained and a partially constrained system for *in vitro* biomechanical testing of the L5-S1 spinal unit was conducted.

Objectives : Compare the compliance and the coupling of the L5-S1 unit measured with an unconstrained and a partially constrained test for the three major physiological motions of the human spine.

Summary of Background Data : Very few studies compared unconstrained and partially constrained testing systems using the same cadaveric FSUs.

Methods : Seven human L5-S1 units were tested on both a pneumatic, unconstrained, and a servohydraulic, partially constrained system. Each FSU was tested along three motions: flexion-extension, lateral bending and axial rotation.

Results : The obtained kinematics and flexibility curves on both systems are not equivalent, except for the flexion-extension case, where both motions are similar. The directions of coupled motions were similar for both tests, but their magnitudes were smaller in the semi-constrained configuration. The use of a semi-constrained system to characterize lateral bending and axial rotation of the lumbosacral FSU decreased significantly the measured stiffness of the segment.

Conclusions : The unconstrained system is today's "gold standard" for the characterization of FSUs. The selected semi-constrained method seems also to be an appropriate way to characterize FSUs for specific applications. Care should be taken using the latter method when the coupled motions are important.

¹ This chapter has been submitted to *Spine* with the title : " Compliance of the L5-S1 spinal unit: a comparative study between an unconstrained and a semi-constrained system". †‡Charriere E; *Beutler T; †Caride M; ‡Mordasini P; *Orr TE; †Zysset PK.† Swiss Federal Institute of Technology, Mechanical Engineering Department, Lausanne, Switzerland. ‡"Hôpital Orthopédique de la Suisse Romande", Lausanne, Switzerland* M.E. Müller Institute for Biomechanics, University of Bern, Switzerland.

Introduction

Biomechanical testing of functional spinal units (FSUs) is used extensively to better understand the kinematics and the kinetics of the intact and instrumented human spine. Although the fully unconstrained system is considered as the “gold standard”, it remains unclear how the mechanical behavior is affected by the introduction of the limited number of constraints associated with multiple degrees of freedom (DOF) servohydraulic testing systems. There is also a long lasting controversy regarding the choice of the system to reproduce the physiological behavior of an FSU for biomechanical tests.

Some biomechanical studies are conducted using unconstrained systems^{3,4,5,7,10,13,18,19,20,22,24,27,28,30} whereas others are using constrained systems^{2,8,14,15,17,29}. Among all these studies, only one¹² attempted to compare the mechanical behavior between a unconstrained and a semi-constrained system on the same intact FSU. The purpose of such systems are to characterize the three-dimensional mechanics of FSUs or multi-segmental samples^{10,24}, as well as to test implants and fixations devices for the spine^{6,8,9,18,21,29}.

Unconstrained systems are designed to let the tested segment completely free to move and rotate along the six DOF of a rigid body. Pure torque being applied, the segment will follow a free pathway to its stable position and rotate around its “own” rotation axis. Coupled motions occur, especially for boundary conditions breaking the sagittal plane of symmetry, such as lateral bending and axial rotations. This testing method is appropriate to characterize the three-dimensional motion of the L5-S1 FSU.

Constrained systems do not let the segment move and rotate along the 6 DOF. These systems restrict motions along certain directions and some additional forces/torques are therefore produced. The center of rotation is constrained and is not allowed to move freely according to the samples' geometry and to the studied loading case (i.e. injured and stabilized segment). The main advantage of such systems is the simplicity of applying loads or displacements with universal materials testing machines.

We define semi-constrained systems as constrained-like systems with more than one free DOF, but with less than 6 free DOF (as for the fully unconstrained system). With such systems it is possible to apply loads or displacements in a specific direction and to control loads or displacements in the others. New laboratory servohydraulic equipments allow this combination of such forces and displacements and are less sensitive to the positioning of the center of rotation than fully constrained systems. Coupling can also occur and be measured with such systems. Their main advantages are the possibility to control torques, forces, angles

and displacements in multiple directions and to apply dynamic boundary conditions to the tested segment.

This study does not intend to compare the accuracy of load-controlled versus displacement-controlled spine testing system to the *in vivo* case^{13,25,26}. A good review has been made concerning this point by Goel et al.¹¹. The purpose of the present study is to compare the compliance curves of the lumbosacral FSU measured with a semi-constrained system and an unconstrained system using the same anatomical specimens.

Materials and Methods

Seven fresh human cadaveric L5-S1 FSUs (4 M, 3F, avg. age 79 y/o) were obtained in agreement with the ethics regulations of the affiliated hospital. L5-S1 segments with vertebral body abnormalities, gross spinal pathology (including spondylolisthesis, and disk space collapse) and those who had undergone spinal surgery were excluded. All non-ligamentous soft tissues were removed before mounting the FSUs in polymethylmethacrylate (PMMA) blocks. FSUs were wrapped with water-soaked cloth, put in a plastic bag and kept in a freezer at -25°C . The night before testing, they were left to thaw at ambient temperature.

The FSUs were tested in flexion-extension (FE), bilateral axial rotation (AR) and bilateral lateral bending (LB) using first an unconstrained (custom designed, also used for the Grassmann et al. study¹) and then a semi-constrained system (MTS, Minneapolis, MN). The former system (Figure 1A) involved the application of stepwise unconstrained pure moments (0 Nm, 2.5 Nm, 5 Nm, 7.5 Nm and 10 Nm) on L5 in the principal motion direction, allowing motion along 6 DOF that was quantified using an optoelectronic camera (Northern Digital, Waterloo, ON). S1 was fixed and unable to move. This procedure was repeated three times and data were recorded during the last cycle. The segment was left creeping during one minute between each moment increment. According to Panjabi et al.²², a flexibility protocol has been used for this configuration. The latter was a commercial multiaxial system (Figure 1B), which allowed the control of a maximum of three DOF. For the FE motion, flexion-extension angles were applied, axial torque and axial force being strictly kept to zero. For the LB motion, bilateral lateral bending angles were applied, axial torque and axial force being strictly kept to zero. Finally, for the AR motion, bilateral axial rotation angles were applied, axial force being strictly kept to zero. All other motion directions were fixed. This system is called the “semi-constrained system” in this paper. The specimens were positioned on and aligned to the systems with frontal and lateral X-ray radiographs.

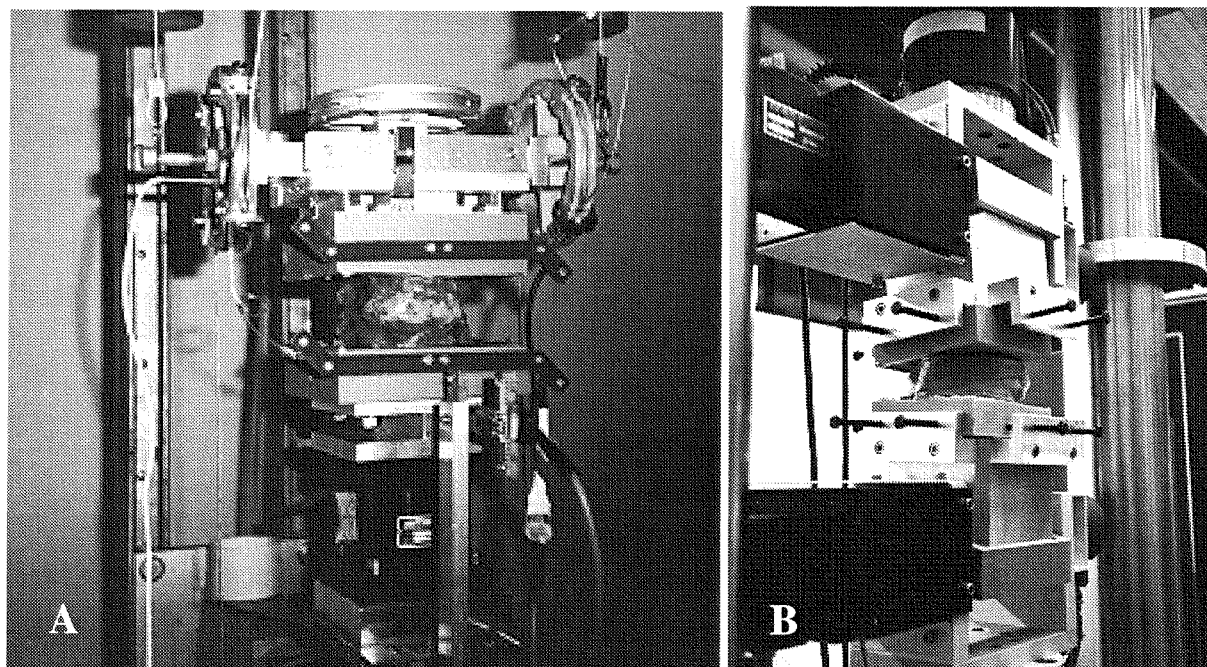


Figure 1: Picture of mechanical test set-ups. A : Unconstrained system in the flexion-extension configuration. Pulleys are used to apply a pure torque. The upper PMMA block is free to move in all directions. Eight active infrared light-emitting diodes enabled the measurement of the three-dimensional relative motion. B : Semi-constrained system in the flexion-extension configuration. The MTS multi-axial servohydraulic system allows the application of controlled torque or angle.

For the sake of direct comparison between the two experiments, it is necessary to characterize the nonlinear compliance curves by some variables. Stiffness is calculated as the slope of the observed linear part of the compliance curve (between 2.5 Nm and 10 Nm) and the neutral zone by its intersection with the angle axis. The experimental data are also fitted with a two-parameter power law (Equation 1).

$$\text{Angle} = a \cdot |\text{Torque}|^b \quad (\text{Equation 1})$$

Angle decomposition

In order to compare these two testing methods as accurately as possible, it is necessary to express the variables in the same reference system. The goal of this work being to quantify the movement of L5 compared to S1, a reference system is associated with each vertebra and the relative movement of the one compared to the other will be measured or calculated according to the experimental method used.

The origin of the reference system associated with L5 is the inferioposterior point of the average sagittal plane of the vertebral body. For S1, the vertebral body being more difficult to distinguish individually, since it is fused with the different sacral vertebrae, the origin of the reference system is located at the superioposterior point of the average sagittal

plan. For the two systems of axes, the X axis is directed towards the left and it is perpendicular to the sagittal plan. The XZ plan selected was defined parallel to the lower endplate of the vertebral body of L5, respectively the upper endplate of that of S1. The Figure 2 shows a schematic sagittal representation of the segment and its associated reference systems.

All rigid body motions have been described in three axis rotations and one translation using the ZYX Cardan angle decomposition.

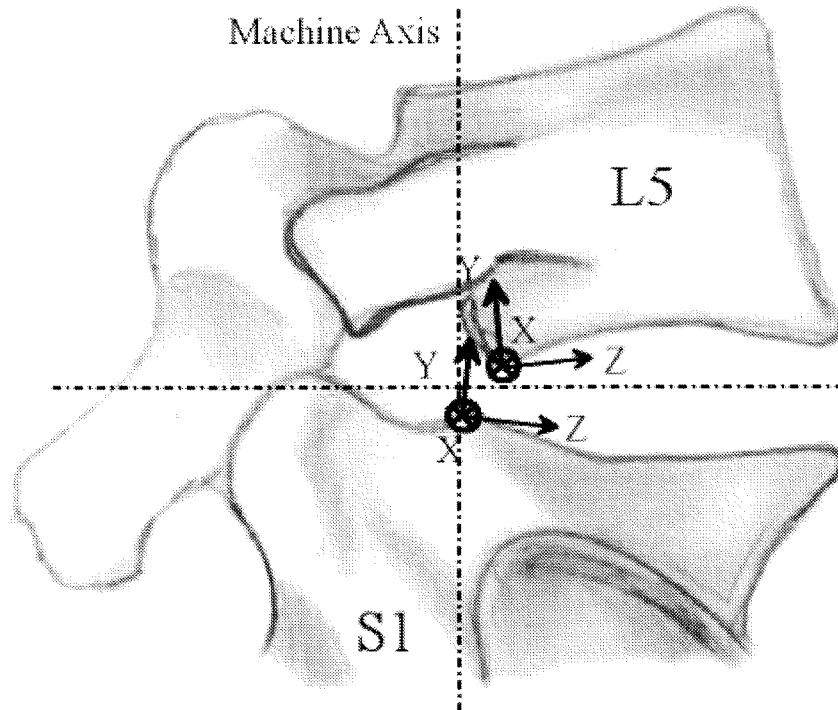


Figure 2 : Schematic sagittal representation of the segment and its associated reference systems

Instantaneous axis of rotation

The motion of a rigid body may be expressed with a unique rotation about and a unique translation along a particular axis³¹. The axis along which the object translates and rotates is called the helical axis (screw axis or instantaneous axis of rotation AOR). This representation of a joint motion is very useful in order to understand and compare complex motions, such as joint movement. It is therefore possible to compare the AOR of a joint and the translation of the bones involved in a joint. The mathematical helical decomposition of such angle and translations used in this study was done according to Kinzel et al.¹⁶. Considering the helical axis, the helical angle is defined as the angle measured around this axis and the helical torque is the projection of the torque on this axis. Helical stiffness is calculated as the slope of the observed linear part of the helical compliance curve (helical angle vs. helical torque).

Statistical analysis

Statistical comparisons between the unconstrained and the semi-constrained results were conducted using the two-sample Wilcoxon signed rank test. Significance was attributed to p values below 0.05.

Results

Figure 3 shows all obtained angle-torque curves as well as the mean flexibility fitted power laws for all segments and all motion types on both systems. These fitted curves are compared to the results obtained by Panjabi et al.²⁴. The two coefficients of the power law are presented in Table 1 for all motions. In order to simplify the presentation of the results, coupled motions are not shown in this paper. The coupled motions measured on the unconstrained system agree with those found by Panjabi et al.²⁴. The directions of coupled motions, which are allowed to occur on the semi-constrained system, were similar for both set-ups, but the magnitudes were smaller in the semi-constrained configuration, especially in axial torsion and lateral bending. The largest motion and neutral zone occur in flexion. In axial rotation, the neutral zone is the smallest and stiffness the largest compared to the other motions.

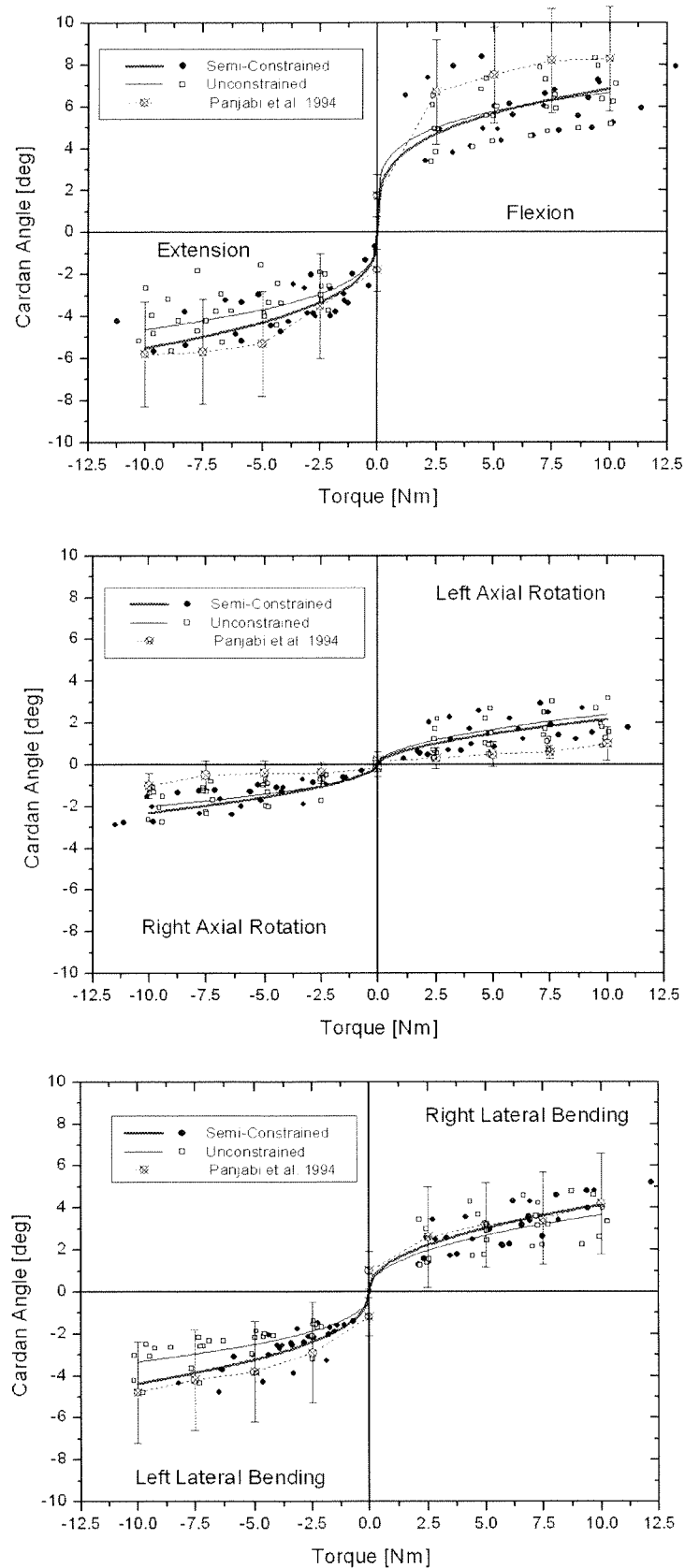


Figure 3 : Compliance curves for flexion-extension(A), bilateral axial rotation(B) and bilateral lateral bending(C). They were fitted with the four experimental data for each experiment and for each motion and compared with the study of Panjabi et al.²⁴

For flexion-extension (Figure 3A), stiffness did not show significant differences between both methods (Figure 4). Furthermore, directions and magnitude of the allowed coupled motions were similar. No significant differences were found between unconstrained and semi-constrained neutral zones (Figure 5, $p=0.15$ for flexion and $p=0.28$ for extension motion). Considering axial rotation (Figure 3B), a significant difference in stiffness ($p=0.047$) was found between the unconstrained and semi-constrained methods. The unconstrained principal motion was 26% stiffer than the semi-constrained one. No significant differences were found between unconstrained and semi-constrained neutral zones ($p=0.81$). Finally, considering lateral bending (Figure 3C), more significant differences in both stiffness ($p=0.015$) and neutral zone ($p=0.016$) were found. The unconstrained principal motion was 53% stiffer than the semi-constrained one. The unconstrained neutral zone was 6% larger than the constrained one.

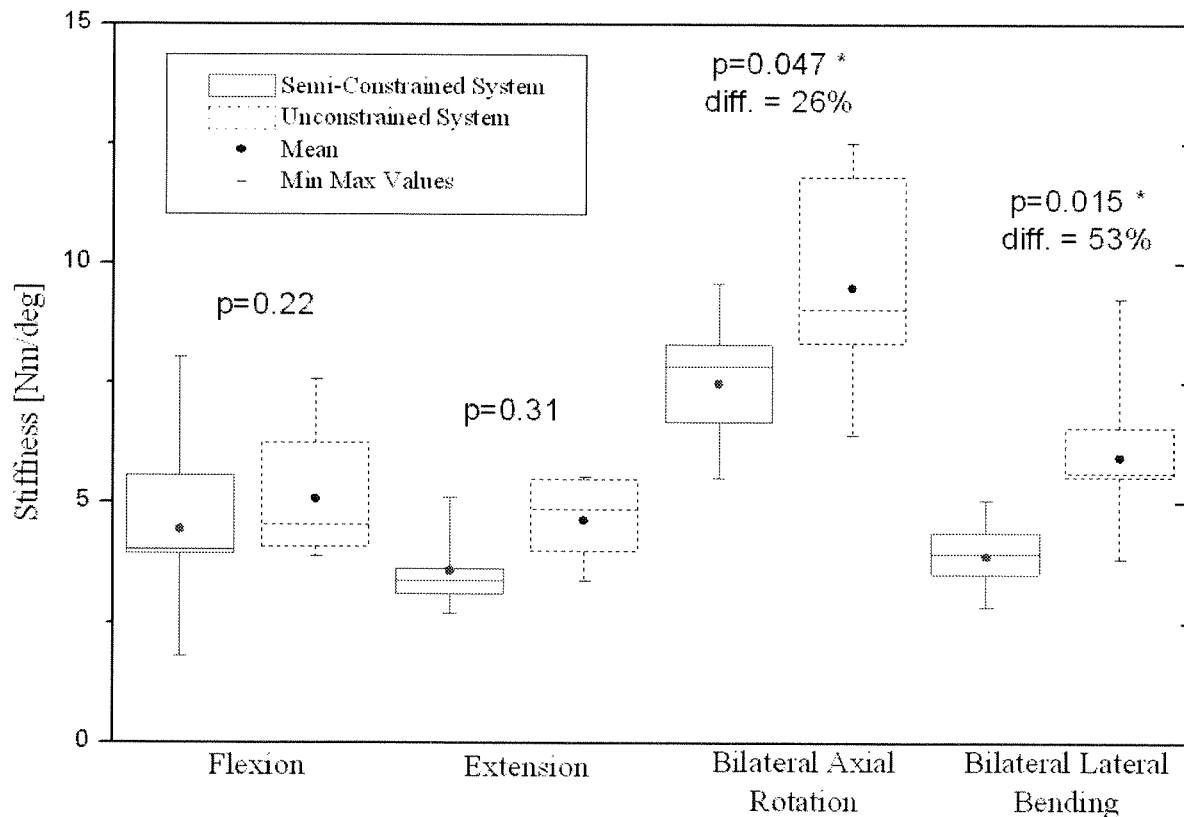


Figure 4 : Box-whisker plots of stiffness compared between both systems. The boxes represent the upper and lower quartiles, whereas the whiskers show the maximum and minimum values. Significant differences are designed by a * after the p value.

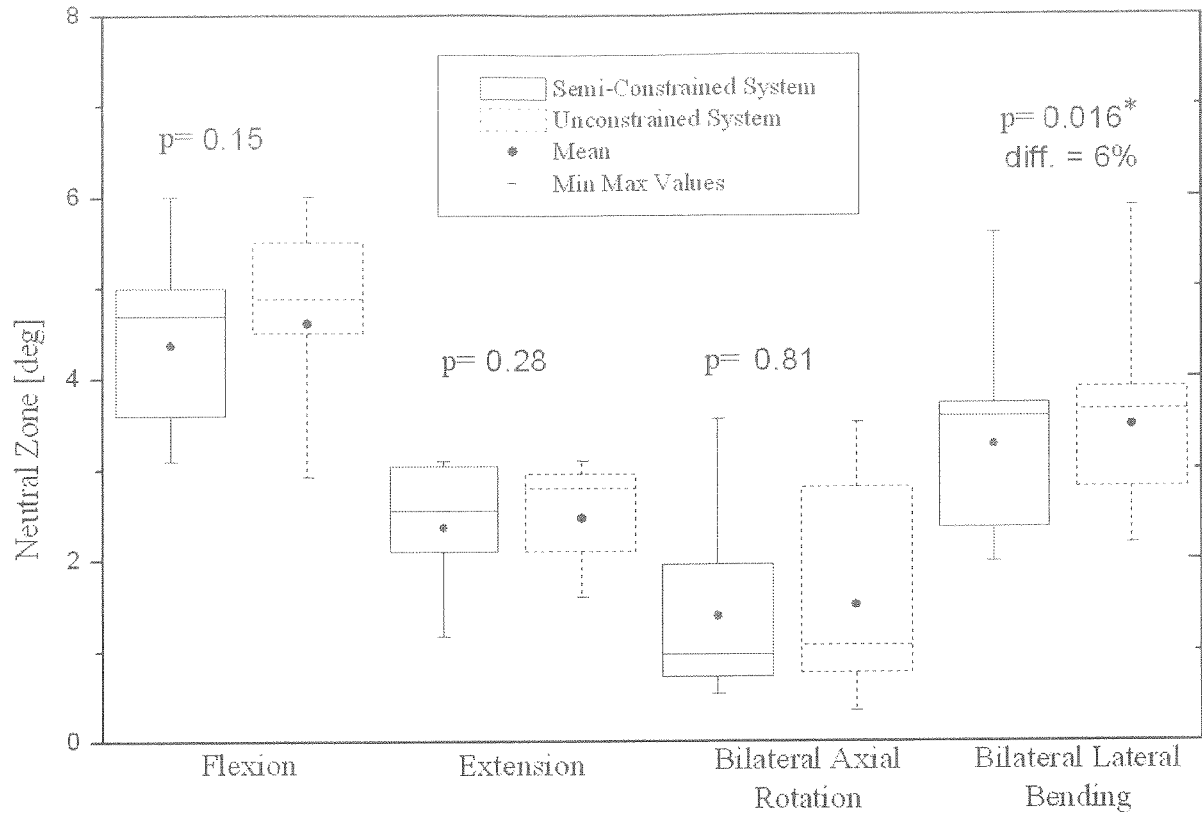


Figure 5 : Box –whisker plots of the neutral zone compared between both systems. . The boxes represent the upper and lower quartiles, whereas the whiskers show the maximum and minimum values. Significant differences are designed by a * after the p value

Table 1 : Coefficients of the power law ($Angle = a \cdot |Torque|^b$) for all motions on both systems. The results for the unconstrained system are printed in italic and in the gray columns.

	Flexion	Extension	Bilateral Axial Rotation	Bilateral Lateral Bending
abs(a)	3.65±1.26	2.38±0.78	0.61±0.39	1.53±0.56
	<i>4.12±1.03</i>	<i>2.16±0.47</i>	<i>0.65±0.48</i>	<i>1.46±0.66</i>
b	0.27±0.06	0.37±0.10	0.56±0.12	0.44±0.12
	<i>0.21±0.05</i>	<i>0.33±0.04</i>	<i>0.51±0.19</i>	<i>0.39±0.11</i>

For flexion-extension, there is also no significant difference between helical stiffness ($p=0.22$ for flexion and $p=0.25$ for extension). In flexion, the helical neutral zone is 15% larger for the unconstrained compared to the semi-constrained system ($p=0.015$). In extension, no significant differences have been observed ($p=0.31$). For bilateral axial rotation, there is also no significant difference between helical stiffness on both systems ($p=0.25$). The helical neutral zone is 56% larger for the unconstrained compared to the semi-constrained system ($p=0.006$). For bilateral lateral bending, the helical stiffness is 35% larger for the

unconstrained compared to the semi-constrained system ($p=0.0398$). The helical neutral zone is 52% larger for the unconstrained compared to the semi-constrained system ($p=0.0005$).

The helical axis averaged over the seven FSUs of the right lateral bending (motion which gave the most important differences in the stiffness and neutral zones between both systems) is shown on Figure 6 for both systems. The unconstrained AOR differs extensively from the semi-constrained set-up, as coupled motions are more important on the former system.

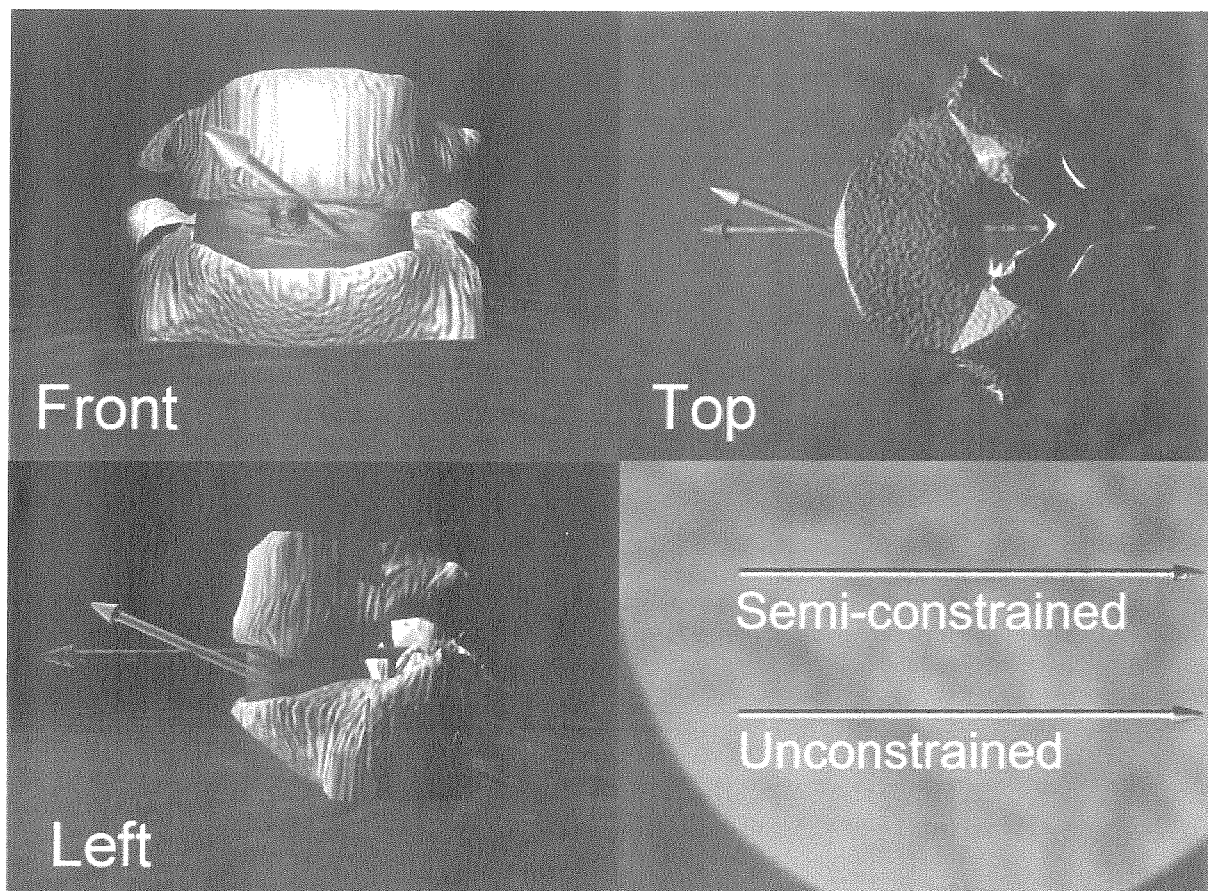


Figure 6 : Standard views of the helical axis for the left lateral bending. The arrows indicate the negative helical rotation.

Discussion

Despite the advanced age of our anatomical specimens, the principal flexibility curves obtained with the unconstrained method in flexion-extension, axial rotation and lateral bending were consistent with previous data²⁴. Flexion-extension motions depend extensively on the disk material properties and stiffness of these disks increases with age. Therefore, it seems reasonable that our elderly segments are somewhat stiffer than the one tested by Panjabi et al.²⁴ for the flexion-extension motion. Furthermore, as axial rotations range of motion depends extensively on the quality of the facets and of the remaining quantity of cartilage on them, the laxity of our aged segments is greater than the one measured by Panjabi et al.

The semi-constrained method appears to provide the same flexion-extension behavior than the unconstrained method. Since the coupled translations are comparable, the semi-constrained set-up could therefore be used as an alternative to the unconstrained one for this particular motion.

As a result, dynamic testing of L5-S1 segments could be envisaged for the flexion-extension motion type. However, a precise placement of the axis of rotation (AOR) is recommended in order to keep the results comparable. According to Panjabi et al.²³ & Haher et al.¹⁵ studies, the AOR is located around the vicinity of the posterior longitudinal ligament, nearby the posterior point of the average sagittal plan of the vertebral body (as used in this study and shown in Figure 2). These authors claim that changing the position of the AOR has a profound effect on the flexibility curve of the tested FSU.

Position of the AOR was found to be nearly equivalent on the two mechanical set-ups for the flexion-extension motion. As coupling is negligible for such movement, the AOR is almost perpendicular to the sagittal plane. Differences between the sagittal locations (YZ plan) of the axis do not exceed 15 mm. The difference is mainly due to the positioning of the segment on the semi-constrained machine. For such system, aligning the sagittal machine axis to average plan of the disk and the longitudinal machine axis to superioposterior point of the average sagittal plan of S1 will shift the AOR posteriorly and cranially. For the unconstrained system, fixing S1 to the table and let only L5 move will shift the AOR caudally. Despite these dissimilarities between the results obtained on both systems, the mechanical behavior of the segment is comparable.

The use of a semi-constrained system to characterize lateral bending and, to a lower extend, axial rotation of the lumbosacral FSU decreases significantly the measured stiffness. This behavior was previously observed by Grassmann et al.¹² in axial rotation of lumbar FSUs. It was shown that coupled motions tended to restrict the principal motion of lumbar FSUs. Constraining the segment reduces the coupled motions and decreases the principal stiffness. It is not easy to conceive why the stiffness increases with the number of free DOF on the testing set-up. The helical decomposition tends to decrease the differences between stiffness, because all motions are taken into account in this case (main motion + coupled motions). On the one hand, the mean stiffness of the FSUs tested on the semi-constrained system for the bilateral lateral bending remains almost constant, independently of the used decomposition (7.5 Nm/deg in the Cardan decomposition and 7.7 Nm/deg in the helical decomposition). On the other hand, the mean stiffness of the FSUs tested on the unconstrained system for the same motion decreases from 9.5 Nm/deg in the Cardan

decomposition to 7.0 Nm/deg in the helical decomposition. This decrease of the stiffness is explained by the large amount of coupling in this case. In the semi-constrained configuration and in the lateral bending case, the helical neutral zone and stiffness remain smaller than in the unconstrained configuration. Furthermore, differences in the mean AOR position averaged over the seven FSUs (22 mm for the bilateral axial rotation in the XZ plan and 25 mm for the bilateral lateral bending in the XY plan, both laterally) is larger than for the flexion-extension motion and are mainly due to the large amount of coupling for such motions.

As the helical axis (for the whole motion) is not oriented and positioned identically in the two configurations, the FSU is tested along two quite distinct motions. The fact that the unconstrained loading path leads to a lower compliance than the semi-constrained path should be confirmed by the use of a finite element model of the lumbosacral FSU including the joint facets with the corresponding boundary conditions.

Comparing this study with the one conducted by Grassmann et al. provides new information on these testing methods. As found for the completely constrained axial rotation¹², we have found that constraining the segment decreases the stiffness. Same results have been found for lateral bending, and the decrease of the stiffness was even more pronounced. However, for the flexion-extension motion, both systems are comparable, and both could therefore be used for the characterization of intact FSU. Trying to characterize the mechanical behavior of injured segments or segments with fixations or implants with the semi-constrained system for the flexion-extension motion may increase the difference between the results found on both systems. The natural AOR may shift with these new conditions and additional forces may be generated in the semi-constrained configuration.

According to our findings, particular care should be given when quantifying and comparing the compliance of the intact or instrumented spine with experimental set-ups of various degrees of constraints for axial rotation and to an even larger extent for lateral bending. The obtained kinematics and compliance on both systems are not equivalent, i.e. the segment does not follow the same pathway to the equilibrium positions, except for the flexion-extension case, where both motions are similar. Furthermore, as *in vivo* boundary conditions are mixed conditions (i.e. torques and forces, rotations and translations are simultaneously imposed to various parts of the segment) that are not well identified, it remains very difficult to impose realistic boundary conditions to the segment *in vitro*.

References

1. Abumi K, Panjabi MM, Duranceau J. Biomechanical evaluation of spinal fixation devices. Part III. Stability provided by six spinal fixation devices. *Spine* 1989;14:1249-55.
2. Adams M, Hutton W. The relevance of torsion to the mechanical derangement of the lumbar spine. *Spine* 1981;6:241-8.
3. Ahmed AM, Duncan NA, Burke DL. The effect of facet geometry on the axial torque-rotation response of lumbar motion segments. *Spine* 1990;15:391-401.
4. Andersson GBJm, Schultz AB. Effects of fluid injection on mechanical properties of intervertebral discs. *J Biomech* 1979;12:453-8.
5. Asazuma T, Stokes IAF, Moreland MS, et al. Intersegmental spinal flexibility with lumbosacral instrumentation: An *in vitro* biomechanical investigation. *Spine* 1990;15:1153-8.
6. Ashman RB, Birch JB, Bone LB, et al. Mechanical testing of spinal instrumentation. *Clin Orthop* 1988;227:113-25
7. Bodem SD, Martin C, Rudolph R, et al. Increase of motion between lumbar vertebrae after excision of the capsule and cartilage of the facets-a cadaver study. *J Bone Joint Surg [Am]* 1994;76:1847-53.
8. Brodke DS, Dick JC, Kunz DN, et al. Posterior lumbar interbody fusion – a biomechanical comparison, including a new threaded cage. *Spine* 1997;22:26-31.
9. Edwards WT. Biomechanics of posterior lumbar fixation. Analysis of testing methodologies. *Spine* 1991;16:1224-32
10. Goel VK, Goyal S, Clark C, et al. Kinematics of the whole lumbar spine : Effect of discectomy. *Spine* 1985;10:543-54.
11. Goel VK, Wilder DG, Pope MH, et al. Controversy : Biomechanical testing of the spine. Load-controlled versus displacement-controlled analysis. *Spine* 1995;20(21):2354-7.
12. Grassmann S, Oxland TR, Gerich U, et al. Constrained testing conditions affect the axial rotation response of the lumbar functional spinal units. *Spine* 1998;23:1155-62.
13. Gunzburg R, Hutton W, Fraser R. Axial rotation of the lumbar spine and the effect of flexion. *Spine* 1991;16(1):22-28.
14. Hafer TR, O'Brien M, Dryer JW, et al. The role of the lumbar facet joints in spinal stability: Identification of alternative paths of loading. *Spine* 1994;19:2667-71.
15. Hafer T, O'Brien M, Felmy WT et al. Instantaneous axis of rotation as a function of the three columns of the spine. *Spine* 1992;17-6 suppl.:149-154
16. Kinzel GL, Hall AS, Hillberry BM. Measurement of the total motion between two body segments-I. Analytical development. *J. Biomech* 1972;5:93-105.
17. Kunz DN, McCabe RP, Zdeblick TA, et al. A multi-degree of freedom system for biomechanical testing. *J Biomech Eng* 1994;116:371-3.
18. Lund T, Oxland TR, Jost B, et al. Interbody cage stabilization in the lumbar spine. *J Bone Joint Surg [Br]* 1998;80-B:351-9.
19. Nachemson AL, Schultz AB, Berkson MH. Mechanical properties of human lumbar spine motion segments : Influence of age, sex, disc level, and degeneration. *Spine*;4(1):1-8.

20. Oxland TR, Crisco JJ III, Panjabi MM, et al. The effect of injury on rotational coupling at the lumbosacral joint. A biomechanical investigation. *Spine* 1992;17:74-80.
21. Panjabi MM. Biomechanical evaluation of spinal fixation devices : 1. A conceptual framework. *Spine* 1988;13:1129-34.
22. Panjabi MM, Brand RM, White AA. Three-dimensional flexibility and stiffness properties of the human thoracic spine. *J. Biomech* 1976;9:185-192.
23. Panjabi MM, Kato Y, Hoffman H, et al. A study of stiffness protocol as exemplified by testing of a burst fracture model in sagittal plane. *Spine* 2000;21:2748-54
24. Panjabi MM, Oxland TR, Yamamoto I, et al. Mechanical behavior of the human lumbar and lumbosacral spine as shown by the three-dimensional load-displacement curves. *JBJS* 1994;76-A:413-24
25. Pearcy M, Portek I, Shepherd J. Three-dimensional X-ray analysis of normal movement in the lumbar spine. *Spine* 1984;9(3):294-300.
26. Pearcy MJ, Tibrewal SB. Axial rotation and lateral bending in the normal lumbar spine measured by three-dimensional radiography. *Spine* 1984;9(6):582-7.
27. Schultz AB, Warwick DN, Berkson MH, et al. Mechanical properties of human lumbar motion segments-part I : Responses in flexion, extension, lateral bending, and torsion. *J Biomech Eng* 1979;101:46-52.
28. Tencer AF, Ahmed AM, Burke DL. Some static mechanical properties of the lumbar intervertebral joint, intact and injured. *J Biomech Eng* 1982;104:193-201.
29. Tencer AF, Hampton D, Eddy S. Biomechanical properties of threaded inserts for lumbar interbody spinal fusion. *Spine*;20(22):2408-14.
30. Wilke HJ, Claes L, Schmitt H, et al. A universal spine tester for *in vitro* experiments with muscle force simulation. *Eur Spine J* 1994;3:91-7.
31. Woltring HJ, Huiskes R, De Lange A, et al. Finite centroid and helical axis estimation from noisy landmark measurements in the study of human joint kinematics. *Biomech* 1985;18:379-89.

**A FINITE ELEMENT MODEL OF THE L5-S1
FUNCTIONAL SPINAL UNIT: DEVELOPMENT
AND COMPARISON WITH BIOMECHANICAL
TESTS *IN VITRO*****ABSTRACT**

The main objective of this work is to develop a new three-dimensional finite element model of the L5-S1 segment that is able to simulate its passive mobility measured *in vitro*. The model includes the 5th lumbar vertebra, the 1st vertebra of the sacrum, the intervertebral disk, the facet joints as well as the ligaments connecting the two vertebrae. Geometrical modeling is based on the segment of a 72 years old man that was used for the quasi-static biomechanical tests.

Due to their limited role in segment mobility, an isotropic linear elastic constitutive law was used for cartilage, cancellous and cortical bone. The intervertebral disk ground substance was modeled with a non-linear hyperelastic polynomial law. Fibers of the disk, as well as ligaments, were modeled with piecewise linear springs. Flexion-extension, axial rotation, and lateral bending torques were applied to the model. A comparison with the experimental results obtained on the same segment for these three major motions was conducted.

The compliance of the segment subjected to pure torques was found to be similar between numerical and experimental results for all major motions. Coupled motions and translations were also similar, even in their amplitude. Most of the ligaments were stretched exclusively in flexion and extension. For lateral bending, the normal coupled motions originate from the geometry of the disk and not from the facet geometry.

Introduction

The spinal column is a complex structure, which ensures the functions of body support, trunk mobility, and protection of the spinal cord. The L5-S1 segment made up of the fifth lumbar vertebra and the first vertebra of the sacrum is a functional spinal unit (FSU) which is often the source of pathologies. For example, a slipped vertebra often leads to sciatica, and degeneration of the disk causes the apparition of pain in the lumbar region. Serious instabilities of the L5-S1 segment are treated with invasive surgical methods, that aim at achieving a bony fusion of the vertebrae. A recent technique consists in replacing a part of the intervertebral disk by a titanium cage. Experimental evaluation of these interventions raises many difficulties, and the increase of the computing resources suggests to consider numerical models.

Many studies focus on multi-segmental units of the spine. Some are experimental studies^{1,2,3,4,5}, whereas others are numerical^{6,7,8,9,10}. Few among them attempted a understanding of joint kinematics and a comprehensive validation of their model with experimental data obtained on the same geometry.

Mechanical modeling with the finite element method becomes a powerful tool of evaluation¹¹, which must imperatively be validated with careful experiments. This approach makes it possible to limit the use of *in vitro* experiments. The boundary conditions are easily modifiable and the segment remains “intact”, allowing to re-use the model infinitely, and to subject it to all the desired loading cases. Experimental validation of the modeled segment is indispensable before the application of the finite element model. The combination of experiments and simulation is thus a good approach for evaluation of new surgical techniques.

The main objective of this work is to develop a new three-dimensional model of the L5-S1 segment able to simulate its passive mobility and flexibility curves. Three motions are analyzed: flexion-extension (rotation along the transversal axe), axial rotation (rotation along the longitudinal axe) and lateral bending (rotation along the sagittal axe). Comparison with previous experimental results⁵ is made, as well as an evaluation of the stresses and strains in the involved tissues for the three considered motions. Contact zone position at the facet joints are also evaluated for the three motions.

Materials and methods

The segment of a 72 years old man was selected among seven human cadaveric L5-S1 functional spine units (4 M, 3F, avg. age 79 y/o). This segment was chosen because its kinematics represents an average among the seven tested specimens⁵. All non-ligamentous soft tissues except the intervertebral disk were removed. In order to build an accurate finite element mesh of the L5-S1 FSU, reconstruction of the geometry was obtained using quantitative computed tomography (p-QCT). The segment was scanned in a relaxed configuration (no applied weight).

The elaboration of a finite element model requires the geometry of its constituent. Geometric surfaces of the following elements are obtained: the first vertebra of the sacrum, the fifth lumbar vertebra, the cartilage of the zygapophyseal joints (or facet joints), and the intervertebral disk. The two vertebrae have complex surfaces, and require an elaborate method which uses a p-QCT technique in order to reconstruct them. The 80 sliced transversal images of the segment obtained from the p-QCT are separated by 1mm gaps. They are exploited by a segmentation software to reconstitute surfaces of the two vertebral bodies. Surface construction starting from the two-dimensional cuts requires a clear definition of the inner and outer volumes of each vertebra. Images provided by p-QCT do not provide a sufficient contrast for an automatic reconstruction. Manual interventions on the two-dimensional cuts allow correcting the contour evaluation. The introduction of these new cuts in a segmentation software provides a 3D representation of the two vertebrae (Figure 1). This representation is done by a polygon mesh, which is a cloud of points located at the borders of the volumes and connected by segments. We thus do not have at this stage the mathematical representation of surfaces, or the equations of surfaces of the two vertebrae, needed for the construction of the model. This last stage is done by a generating Non-Uniform Rational B-Spline (NURBS) surfaces software. The maximal construction error (defined by the normal distance) between the polygon mesh and the B-spline surface is 0.61 mm. At the facet joints, this error does not exceed 0.17 mm.

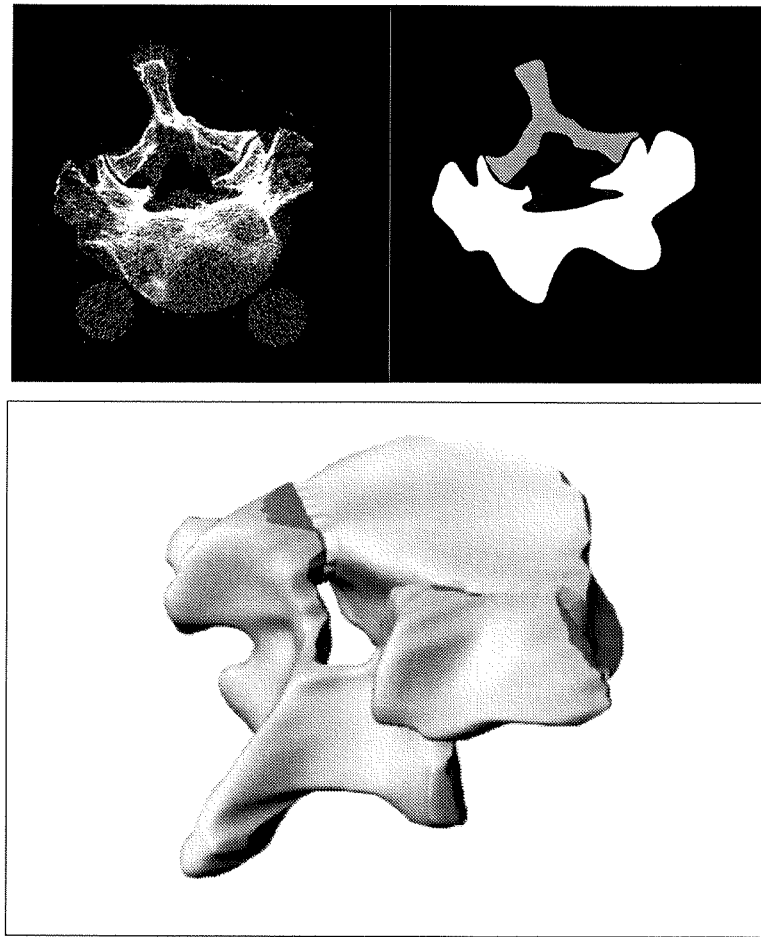


Figure 1 : L5 3D reconstruction: the obtained images from the p-QCT are manually post treated with an image processing software. The segmentation of these new images engenders a 3D polygon mesh.

The surfaces of cartilage were built on the basis of the two facet joints surfaces and of the literature for their thickness. Swanepoel¹² studied the thickness of zygapophyseal joints in his thesis for the L1-L2 joints. The mean cartilage thickness for the concave facets (entire superior zygapophyseal joint surfaces) is $1.10\text{mm} \pm 0.31\text{mm}$. The thickest cartilage occurs centrally, and is 1.21mm thick with a 95% confidence interval of 0.10mm . The corresponding figures for the inferior convex joint surfaces are $0.94\text{mm} \pm 0.31\text{mm}$ for the entire joint surface, (mean \pm 1 SD), with the thickest cartilage occurring centrally - $1.07\text{mm} \pm 0.10\text{mm}$. Therefore, for superior and inferior zygapophyseal joint surfaces, a cartilage thickness of 1 mm was used for our model.

The geometry of the disk was extruded between the upper and lower endplate and was drawn directly with a three-dimensional CAD software (I-Deas Master Series 8, SDRC Inc).

In order to generate the finite element mesh of this complex structure, the B-spline surfaces were imported in a CAD software (I-Deas Master Series 8, SDRC Inc.). The volumes were reconstructed from these surfaces. The meshing was achieved with linear tetrahedral

solid for all volumes, shell elements for the cortical bone and piecewise linear springs elements for ligaments and intervertebral disk fibers. The thickness of all shell elements is 1mm. According to the literature^{20,13}, the piecewise linear springs elements of the intervertebral disk were added to the intervertebral disk in six layers of 30° crisscrossed springs. The following ligaments were modeled: the anterior longitudinal ligament (ALL), the posterior longitudinal ligament (PLL), the yellow ligament or *ligamentum flavum* (LF), the left capsular ligament (LCL), the right capsular ligament (RCL), the interspinous ligament (ISL) and the supraspinous ligament (SSL). A dissection was performed on the segment and allowed to evaluate the insertion location of the ligaments, as well as to measure their dimensions. All element types and numbers are listed in Table 1.

Table 1: Number of elements, element type and Abaqus denomination for all entities.

	# elements	element type	Abaqus denomination
L5 cancellous bone	6237	Linear solid elements	C3D4
L5 cortical bone	2422	Linear shell elements	S3
S1 cancellous bone	5530	Linear solid elements	C3D4
S1 cortical bone	2326	Linear shell elements	S3
L5 cartilage	2676	Linear solid elements	C3D4
S1 cartilage	2587	Linear solid elements	C3D4
Intervertebral disk ground substance	1950	Linear solid elements	C3D4H
Intervertebral disk collagen fibers	110	Nonlinear springs	SPRINGA
Ligaments	79	Nonlinear springs	SPRINGA

This model was designed for the simulation of the relative movement of L5 compared to S1. This movement is largely conditioned by the intervertebral disk, and to a much lower extent by cartilage and bone. We thus paid detailed attention to the definition of the constitutive law of the disk.

Cartilage is biphasic, viscoelastic, non-linear and anisotropic^{14,15}. Furthermore, its tensile behavior is distinct from the compressive one. Bone is poroelastic, anisotropic and viscoelastic¹⁶. However, cartilage, as well as cancellous and cortical bone, were modeled with a linear isotropic elastic law. Due to their minor role in the quasi-static compliance of the L5-

SI FSU^{17,19,24}, an isotropic linear elastic constitutive law was assumed for these tissues. The linear elastic constitutive law is expressed as:

$$\boldsymbol{\sigma} = \mathbb{k} \boldsymbol{\varepsilon}$$

where $\boldsymbol{\sigma}$ is the total stress tensor, \mathbb{k} the isotropic elasticity tensor, and $\boldsymbol{\varepsilon}$ the total strain tensor.

The material properties of the solid linear elements using this law are listed in Table 2.

Table 2 : Material properties of the solid linear elastic elements.

	Young's modulus [MPa]	Poisson's ratio [-]
Cortical bone ²⁴	12000	0.3
Cancellous bone ¹⁸	113	0.3
Facet joint cartilage ¹⁹	0.7	0.1

The intervertebral disk is biphasic, nonlinear, anisotropic and its tensile behavior is distinct from its compressive one. It is composed of two parts: the annulus fibrosus and the nucleus pulposus. The intervertebral disk annulus fibrosus has a multilayered structure, each layer being formed from well-organized collagen fibers running in opposite directions in any adjacent layers at approximately 30° to the horizontal plane²⁰. This structure provides the annulus with a high tensile modulus and strength. The nucleus pulposus is enclosed within the space delimited by the annulus and the endplates and is composed mainly of a hydrophilic polymer called glycosaminoglycan, which is capable of absorbing a large amount of water and which forms a gel-like matrix. The annulus fibrosus was modeled by a hyperelastic constitutive law for the ground substance and by nonlinear 30° springs for the collagen fibers. The hyperelasticity allows simulating the non-linear elasticity of the ground substance in large strain. Hyperelastic materials were described by their potential energy of deformation $W(\mathbf{C})$. This function represents the potential energy stored in material per unit of volume of reference at the point considered for deformation. Many forms of potentials were proposed²¹: Arruda-Boyce, Mooney-Rivlin, Neo-Hookean, Ogden, polynomial, polynomial reduced, Yeoh, and Van der Waals. We choose the polynomial form, which is a generalization of Mooney-Rivlin and reduced polynomial forms.

The polynomial constitutive law is expressed as:

$$\mathbf{S} = 2\nabla_{\mathbf{C}} W = 2\left(\nabla_{\bar{I}_1} W \cdot \nabla_{\mathbf{C}} \bar{I}_1 + \nabla_{\bar{I}_2} W \cdot \nabla_{\mathbf{C}} \bar{I}_2 + \nabla_{\bar{I}_3} W \cdot \nabla_{\mathbf{C}} \bar{I}_3\right)$$

with

$$\begin{aligned}\bar{I}_1 &= J^{-\frac{2}{3}} \cdot (\text{tr} \mathbf{C}) & \bar{I}_2 &= J^{\frac{2}{3}} \cdot (\text{tr}(\mathbf{C}^{-1})) & \bar{I}_3 &= J \\ \nabla_{\mathbf{C}} \bar{I}_1 &= -\frac{2}{3} J^{-\frac{2}{3}} \cdot (\text{tr} \mathbf{C}) \cdot \mathbf{C}^{-1} + J^{-\frac{2}{3}} \cdot \mathbf{I} \\ \nabla_{\mathbf{C}} \bar{I}_2 &= \frac{2}{3} J^{\frac{2}{3}} \cdot (\text{tr}(\mathbf{C}^{-1})) \cdot \mathbf{C}^{-1} - J^{\frac{2}{3}} \cdot \mathbf{C}^{-2} \\ \nabla_{\mathbf{C}} \bar{I}_3 &= J \cdot \mathbf{C}^{-1} \\ \nabla_{\bar{I}_1} W &= \sum_{i+j=1}^N c_{ij} i (J^{-\frac{2}{3}} \cdot \text{tr} \mathbf{C} - 3)^{i-1} (J^{\frac{2}{3}} \cdot \text{tr}(\mathbf{C}^{-1}) - 3)^j \\ \nabla_{\bar{I}_2} W &= \sum_{i+j=1}^N c_{ij} j (J^{-\frac{2}{3}} \cdot \text{tr} \mathbf{C} - 3)^i (J^{\frac{2}{3}} \cdot \text{tr}(\mathbf{C}^{-1}) - 3)^{j-1} \\ \nabla_{\bar{I}_3} W &= \sum_{i=1}^N \frac{2i}{D_i} (J-1)^{2i-1}\end{aligned}$$

where \mathbf{S} is the stress tensor, W the elastic energy, $\bar{I}_1, \bar{I}_2, \bar{I}_3$ the three deviatoric invariants, \mathbf{C} the metric material tensor ($\mathbf{C} = \mathbf{F}^T \mathbf{F}$), J the Jacobian ($J = \det \mathbf{F}$) and \mathbf{F} the deformation gradient. c_{ij} and D_i are the unknown coefficients of this law. As the strain does not exceed 100% in the disk, the N value can be set to two²¹. Thus, this law contains 7 unknown coefficients (5 c_{ij} and 2 D_i).

In order to find the most appropriate coefficients for the constitutive law of the disk, tension, compression, flexion, extension, axial rotation and lateral bending experiments were conducted on a L5-S1 segment (86 y/o, male), where all ligaments and facets were removed. Nine parameters (seven for the ground substance of the disk and two for the fibers of the disk) were modified with a trial and error method. The fibers were modeled with a piecewise linear elastic law using two different stiffness. The nine parameters were corrected until the kinematics of the finite element model fits as well as possible the one obtained experimentally for these different types of motion. The seven optimized coefficients of the polynomial law are listed in Table 1.

Table 3 : Coefficients of the polynomial constitutive law of the disk.

C_{10}	C_{01}	C_{11}	C_{20}	C_{02}	D_1	D_2
0.107E05	-151.5	0.182E06	-0.123E06	-0.109E05	0.258E-05	0.223E-06

In order to examine the mechanical behavior of the intervertebral disk, two types of zones were defined. The first zones separate the anterior, posterior, right and left part of the disk, whereas the second separate the disk in six different layers (Figure 2). Each one of these layers corresponds to a layer of non-linear springs inserted in the disk.

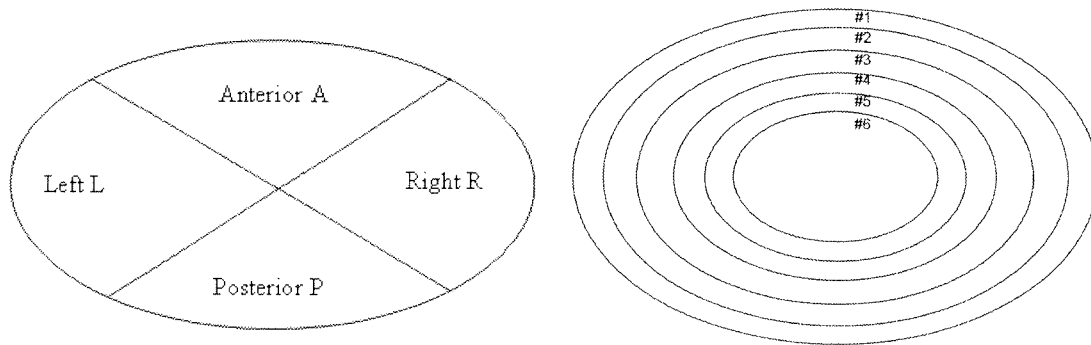


Figure 2 : Definition of the different defined zones in the disk. These separations are used to examine the regional behavior of the fibers.

A solid modeling of the ligaments would be useful if an isolated study of their behavior is intended, which is not within the framework of this work. As this model intended to reproduce their influence on the joint compliance, non-linear springs are sufficient for this purpose. Springs with piecewise constant rigidity in traction and null in compression model this behavior qualitatively. The constitutive law of ligaments and disk fibers is the following:

$$F = \begin{cases} K_1 \cdot \lambda_1, \forall \lambda_1 < \lambda_c \\ K_2 \cdot \lambda_2, \forall \lambda_2 \geq \lambda_c \end{cases}$$

where F is the force, K_1 the rigidity for an elongation λ_1 between zero and λ_c and K_2 the rigidity for an elongation λ_2 larger than λ_c .

It was thus necessary to divide rigidities of the ligament noted K1 and K2 to obtain rigidities of each spring. The rigidity of the ligaments K2 was calculated from the average of different data^{9,18,22,23}. Rigidity K1 of the ligaments, and critical strain ϵ_c were calculated from the experimental results of Goel and al.²⁴. All rigidities and critical strains are listed in Table 4.

Table 4 : Ligaments are modeled by non-linear springs. The number of non-linear spring elements, their mean lengths, their critical strains (strain at which rigidity changes from K_1 to K_2) and their two rigidities are printed for all ligaments.

	# Springs	Mean length [mm]	ϵ_c^{24} [%]	K_1 [N/mm]	K_2 [N/mm]
Anterior longitudinal ligament	9	20	12	146	375
Posterior longitudinal ligament	3	12	11	50	100
Left capsular ligament	26	5	25	66	289
Right capsular ligament	29	4	25	66	289
Ligamentum flavum	5	15	6	166	216
Interspinous ligament	6	13	14	107	125
Supraspinous ligament	1	22	20	60	113

Torques were applied on the L5-S1 FSU by using rigid beam elements attached to the upper L5 endplate, with the S1 lower region being immobilized. These beam elements were concentrated to a single node, where a pure torque of 10 Nm is applied, so that it follows the motion of L5. Six different load cases were studied: flexion, extension, left and right axial rotation, left and right lateral bending. The same loading cases were applied *in vitro* using a fully unconstrained system⁵. At least four computation increments were completed for each case.

The global L5-S1 finite element model with the beam elements used to apply boundary conditions is shown on Figure 3.

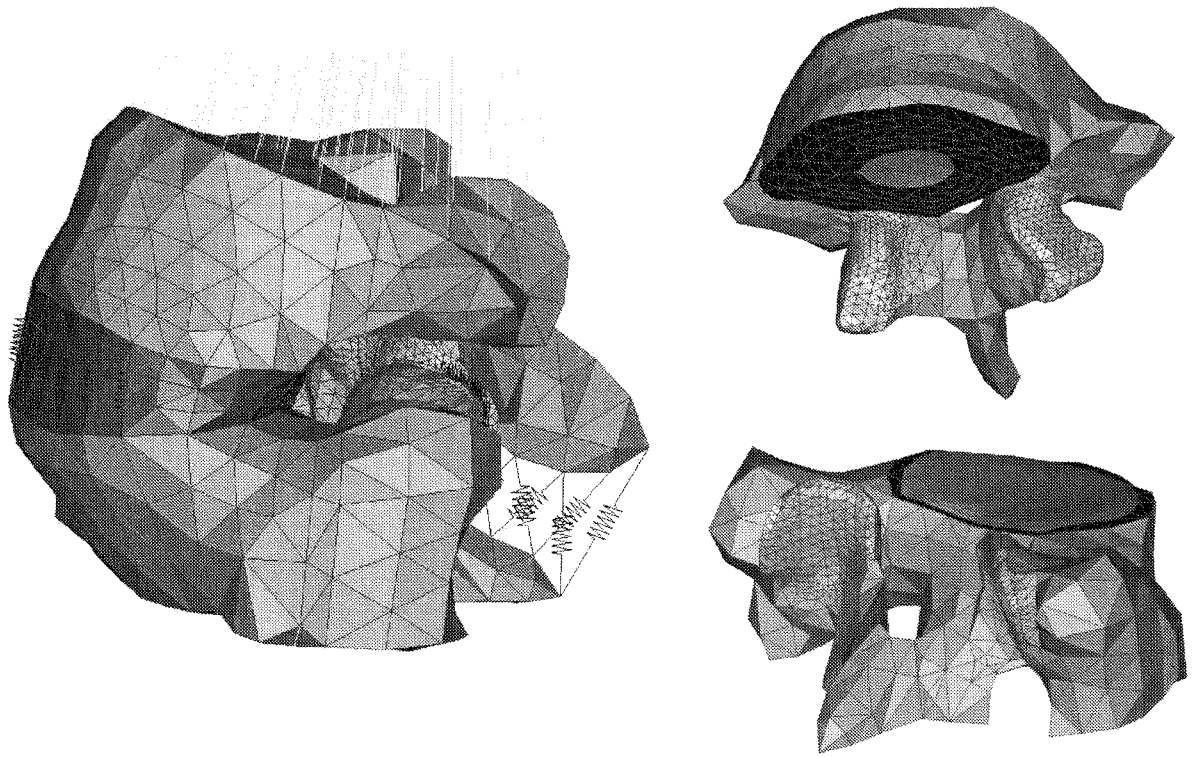


Figure 3 : Finite element model of the L5-S1 segment. The yellow rigid beams are concentrated to a node, where a pure torque is applied

Results

All of the six different simulations converge properly to a solution. Computation time varies from 1 to 24 hours on a 300 MHz bi-processor workstation, depending on the number of needed increments. Obtained flexibility curves for all motions between numerical and experimental data are shown in Figure 4 for flexion-extension, in Figure 5 for bilateral axial rotation and in Figure 6 for bilateral lateral bending. Main motions and major coupled motions are shown. Translations are not plotted, but are quantitatively similar between experimental and numeric for all the motions type.

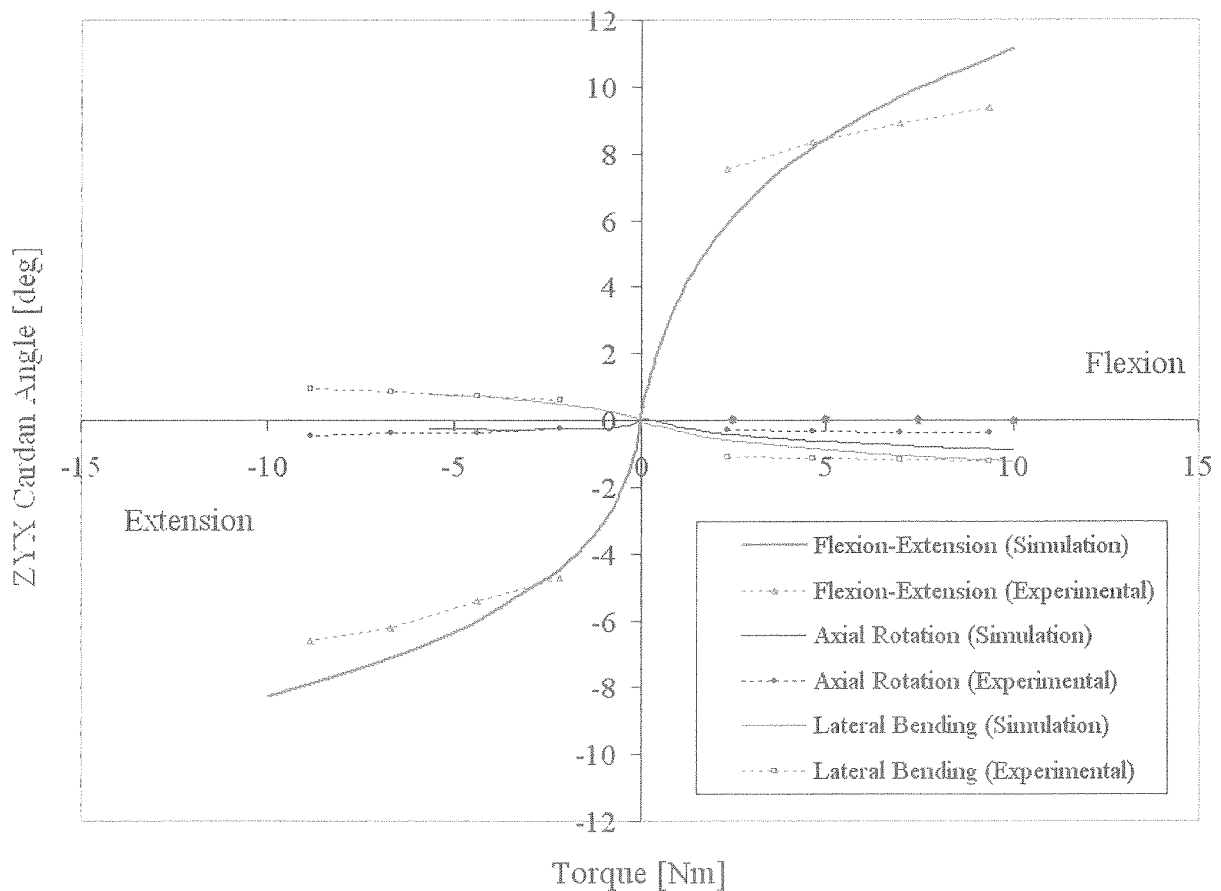


Figure 4 : Numerical and experimental main motion curves for flexion-extension. Coupled motions are also shown for numerical and experimental results. The non-symmetrical characteristic of the flexion-extension motion shows up on both experimentally and numerically systems. Extension motion seems properly modeled, even for the coupled motions. Accurately fitting the flexion motion with our model is not possible, as neutral zone is not large enough and stiffness is too small. However, coupled motions are also similar in flexion.

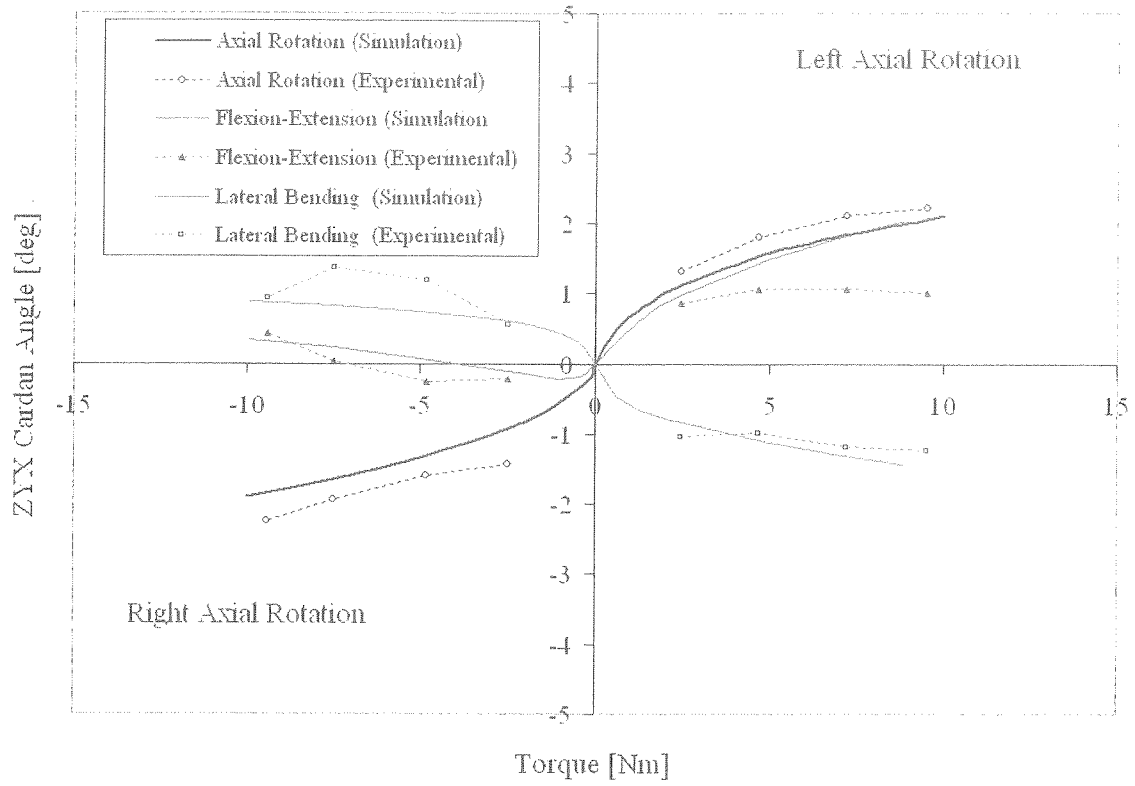


Figure 5 : Numerical and experimental main motion curves for axial rotation. Coupled motions are also shown for numerical and experimental results.

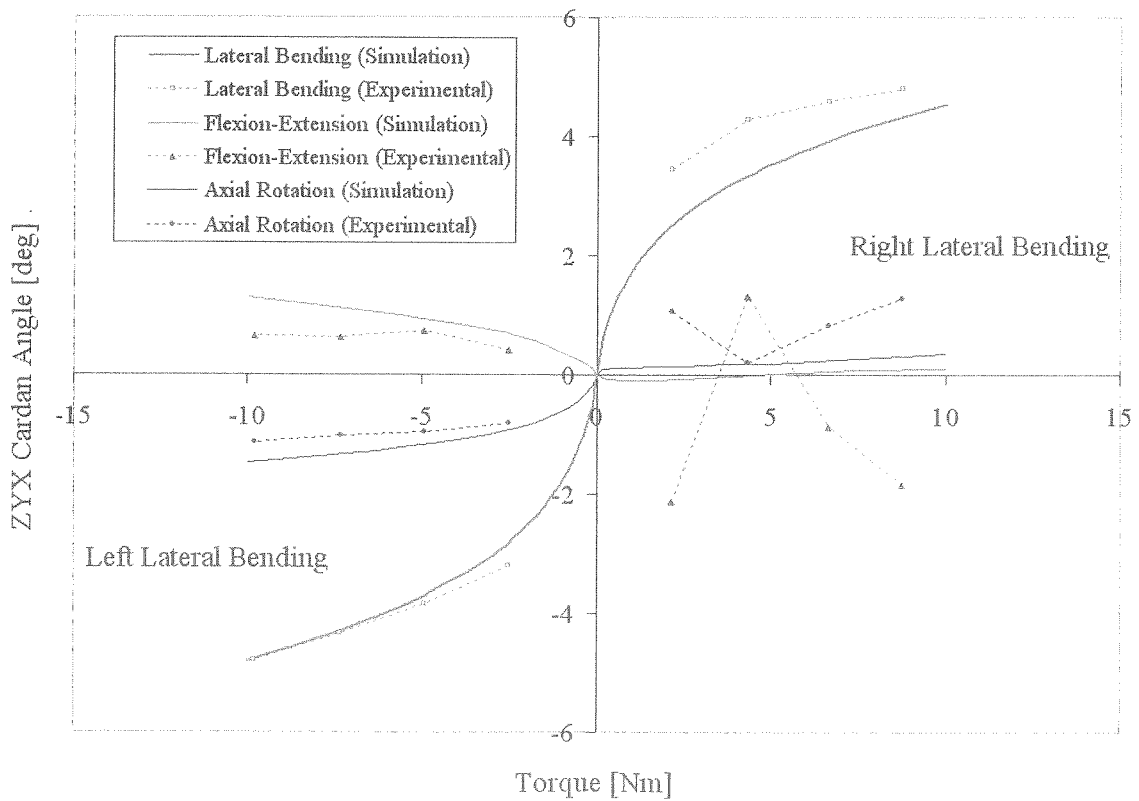


Figure 6 : Numerical and experimental main motion for lateral bending. Coupled motions are also shown for numerical and experimental results.

In flexion, the contact zone is located at the top part of the two S1 facet joints cartilage (Figure 7). This particular position emphasizes the large antero-cranial translation, the small right axial rotation, and the small left lateral bending of the L5 vertebra (Figure 4). Differences between the left and right contact zone are visible. The left cartilage is subjected to higher stresses than the right one. This asymmetry of the stress distribution is due to the geometrical asymmetry of the two facet joints. In extension, the contact zone is located on the caudal part of the right S1 facet cartilage (Figure 7). The right cartilage is the only one to be loaded. There is a large caudal translation, a small right lateral bending and a small right axial rotation of L5. Cartilage undergoes higher stresses in extension than in flexion. Indeed, a maximum equivalent strain of 11% is observed in flexion, whereas the cartilage equivalent strain is 21% in extension (Figure 9).

An important contact zone on the left S1 facet joints cartilage, almost covering all the facet surface area, appears during the right axial rotation motion (Figure 7). Equivalent strain of the left cartilage reaches up to 35% (Figure 9). During the left axial rotation motion, a more important contact zone appears, with equivalent strain up to 37%. The differences between contact zones are again explained by the asymmetry of the facet geometry. Facets joints limit the main motion only in axial rotation, because their surfaces are almost perpendicular to the direction of movement.

During left lateral bending, the contact zone appears on the bottom of the right S1 facet joint surface (Figure 7). For the opposite motion, the contact zone is located on the same facet surface, but more cranially. One could expect to have found the same contact zone in the left facet joint. This difference is probably related to the asymmetry of the flexibility curves obtained for such movement (Figure 6). For this two motion types, maximum cartilage equivalent strain is small and bilaterally similar. It reaches 8% in left lateral bending and 7% in right lateral bending (Figure 9). These results confirm that the lateral bending motion is little affected by the facet joints.

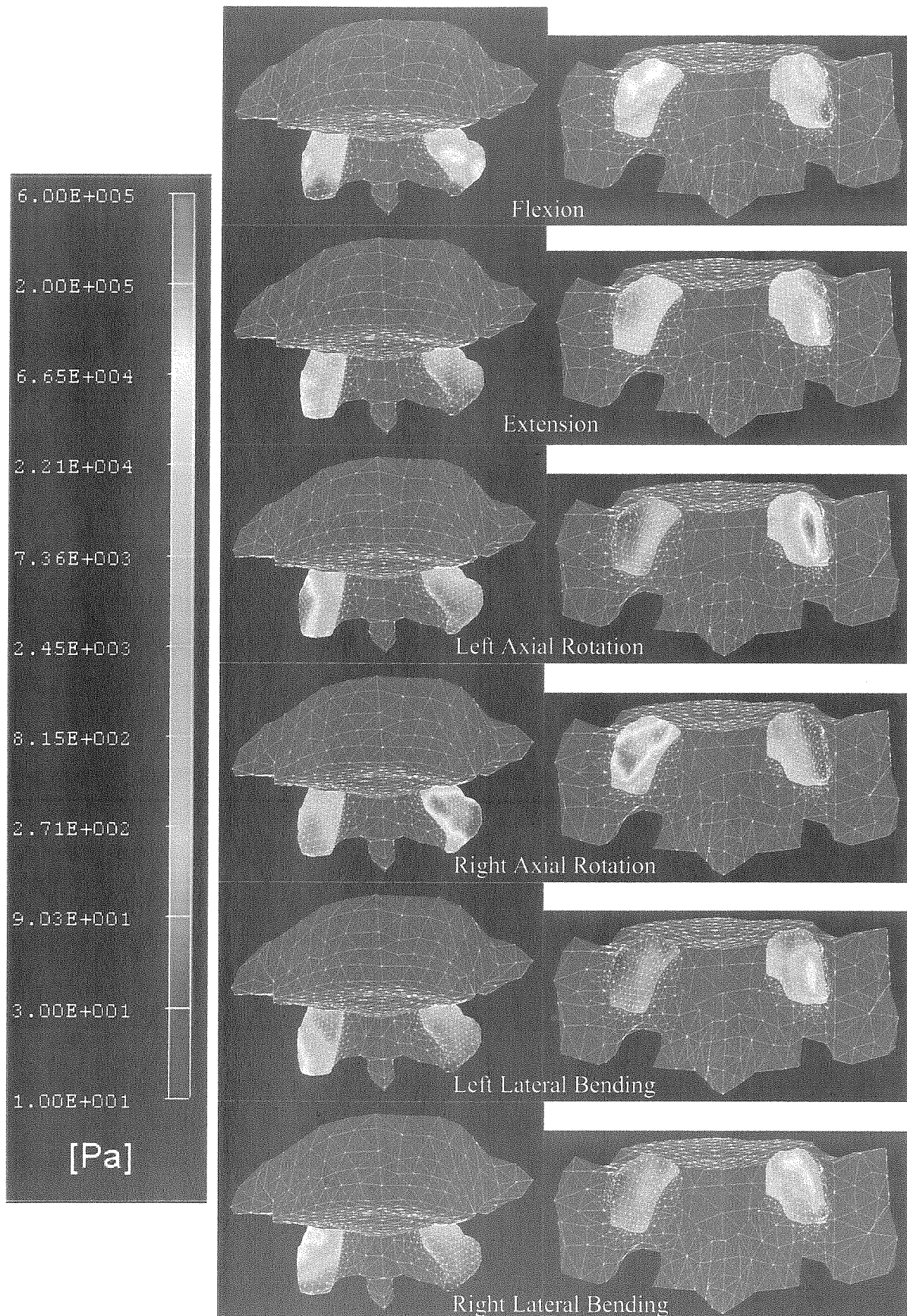


Figure 7 : Normal stresses distribution on the two contact zones. An anterior view of L5 is shown on the left, whereas a posterior view of S1 is shown on the right.

In flexion and extension, the disk maximum compressive Von Mises equivalent strain is 49%. In flexion it is located anteriorly, whereas in extension it is located posteriorly (Figure 8). Although the equivalent strain is similar for both motions, the strain energy density is larger in extension than in flexion (Figure 8). This statement could be explained by the narrowing of the disk in its posterior region.

The strain energy density of intervertebral disk ground substance is small for both axial rotation motion (Figure 10). These strain energies are ten times lower than the one computed for the flexion motion. The equivalent strains do not exceed 30% and are mainly present in the tensile mode.

In left lateral bending, most of the strain energy density is located on the left part of the intervertebral disk (Figure 8), where a maximum equivalent strain of 53% occurs. Concerning the right lateral bending, most of the strain energy density is concentrated in the right part of the disk, where a maximum equivalent strain of 55% occurs. High symmetry between the two strain energy density distributions is observed (Figure 8). The intensity of this strain energy density is located in-between the one measured in flexion and the one measured in extension.

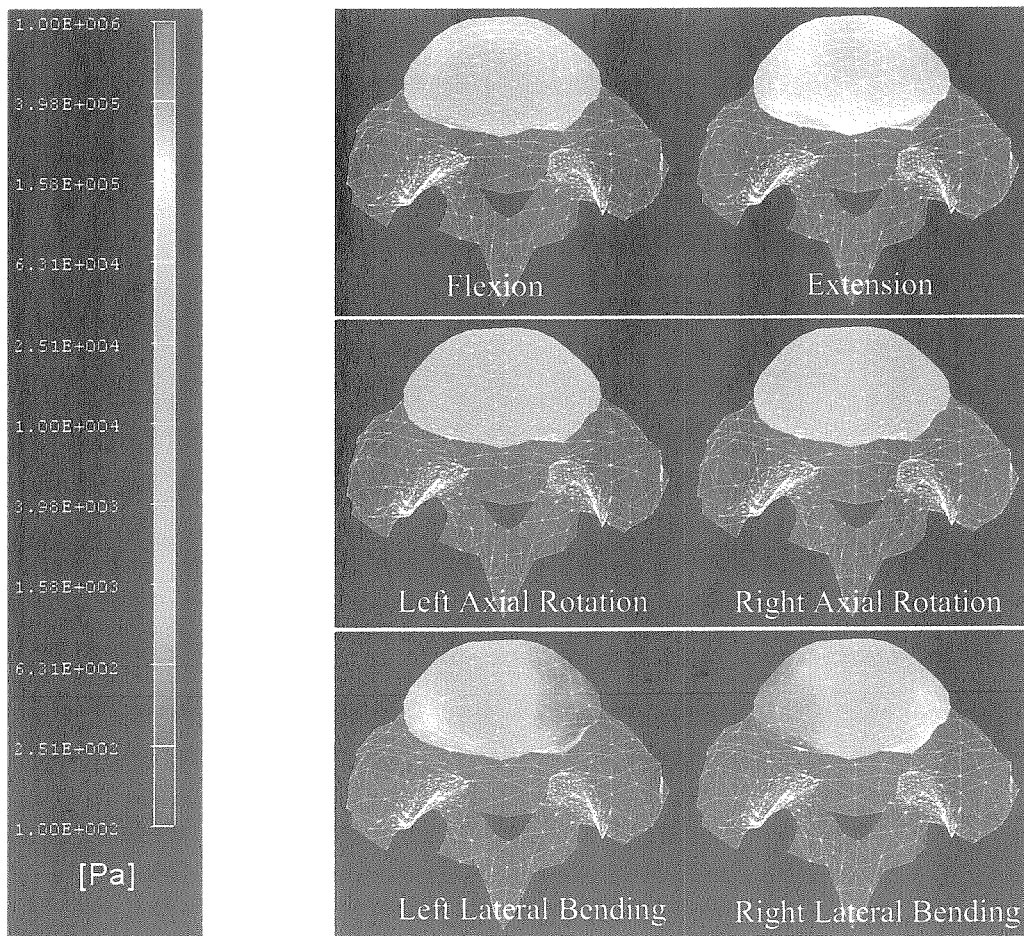


Figure 8 : L5 upper view of the strain energy density of the disk ground substance.

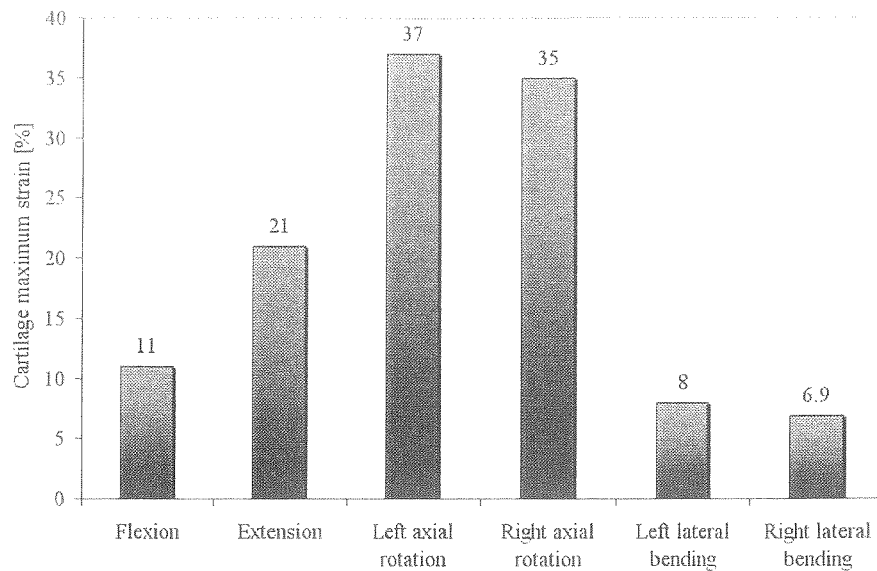


Figure 9 : Cartilage maximum strain at the facet joints.

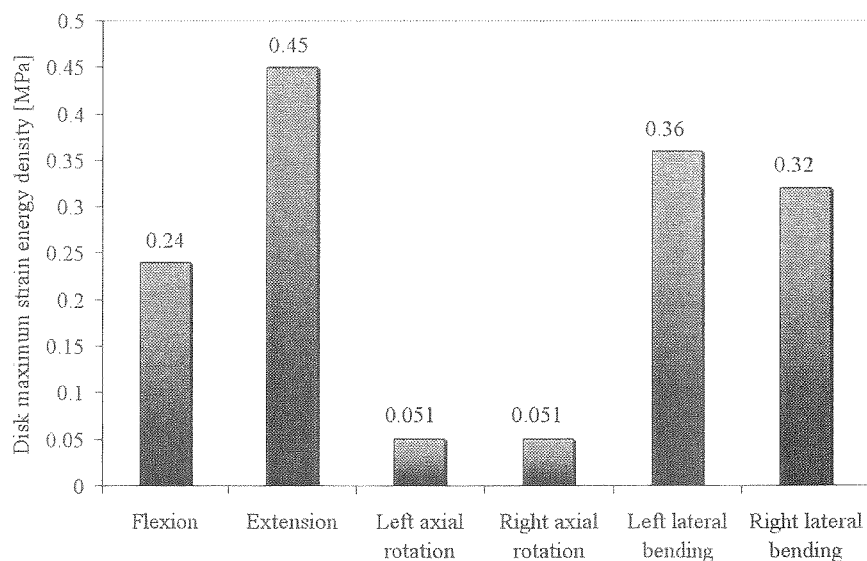


Figure 10 : Ground substance of the intervertebral disk : maximum strain energy density.

In flexion, all ligaments except the anterior longitudinal ligament are loaded (Table 5). The posterior ligaments are the most solicited, especially the ligamentum flavum. Its deformation reaches 30% (Table 5) with a force of 15.7 N (Table 6). In extension, only the anterior longitudinal and the capsular ligaments have substantial deformations, but with very low forces applied on them compared to the force obtained in the flexion motion.

No ligament, except the left capsular ligament, is stretched in bilateral axial rotation (Table 5, Table 6). The forces in the left capsular ligament do not exceed 0.6 N.

No significative deformation of ligaments appears for bilateral lateral bending motions, except for the capsular ligaments. However, amplitude of these deformations is low

compared to the one obtained in flexion. The maximum deformation occurs in the LCL in left lateral bending with 11.5% of deformation (Table 5), whereas a maximum force of 0.32 N (Table 6) is found on the SSL, which is very low.

Most of the ligaments are only solicited in flexion-extension. As expected, their role is to constraint the motion at large amplitude. The ALL limits only the main motion in extension, whereas the PLL, LF, ISL and SSL limit the motion in flexion. In flexion, the ligaments are also means of load transfer, while in extension, load is transmitted through the pedicles, laminae, and articular processes. Capsular ligaments are used in all motions, with a higher function in flexion-extension. However, they do not have an important effect on the overall main motion.

Table 5 : Ligaments strain in % at the maximum motion range. LLA (Anterior Longitudinal Ligament), PLL (Posterior Longitudinal Ligament), LCL (Left Capsular Ligament), RCL (Right Capsular Ligament), LF (Ligamentum Flavum), ISL (Inter-Spinous Ligament), SSL (Supra-Spinous Ligament).

	Flexion	Extension	Right Axial Rotation	Left Axial Rotation	Right Lateral Bending	Left Lateral Bending
ALL	0	4	0	0	0	1.3
PLL	7.6	0	0	0	0	0
LCL	20.7	22.8	13.2	5.4	3.7	11.5
RCL	27.1	8.6	0	0.4	4.6	3.6
LF	30.5	0	0	0	0	0
ISL	39	0	0	0	0.2	0
SSL	20	0	0	0	1.1	0

Table 6 : Force [N] acting on each ligament at the maximum motion range. LLA (Anterior Longitudinal Ligament), PLL (Posterior Longitudinal Ligament), LCL (Left Capsular Ligament), RCL (Right Capsular Ligament), LF (Ligamentum Flavum), ISL (Inter-Spinous Ligament), SSL (Supra-Spinous Ligament).

	Flexion	Extension	Right Axial Rotation	Left Axial Rotation	Right Lateral Bending	Left Lateral Bending
ALL	0	3.5	0	0	0	0
PLL	0.4	0	0	0	0.1	0
LCL	1.0	1.0	0.6	0.2	0.2	0.2
RCL	0.9	0.7	0	0	0	0.1
LF	15.7	0	0	0	0	0
ISL	9.5	0	0	0	0	0
SSL	12.7	0	0	0	0.3	0

In flexion, 75% of the solicited fibers are located in the posterior part of the disk. Only the three outer fibers layers are solicited (Table 7). It corresponds to 30% of the dimensions (length and width) of the disk. In extension, all the solicited fibers of the disk are located anteriorly. Only the two first fibers layers are solicited (Table 7), which corresponds to 20% of the dimensions of the disk. The other fibers layers do not participate in the flexion-extension motion.

In bilateral axial rotation, most of the solicited fibers are situated in the anterior part of the disk (43% in right axial rotation and 67% in left axial rotation). No fibers are solicited in the posterior zone (Table 7). As the initial center of rotation is located on the posterior part of the vertebral body, fibers that are far away from this center are more solicited. This statement explains that the posterior disk fibers are not solicited in bilateral axial rotation. These deformed fibers are stretched, as for other motion types, only in tension in the three outer layers of the disk.

62% of the fibers are solicited on the right part of the intervertebral disk for the left lateral bending and 84% on the left part for the right lateral bending (Table 7). As for the other motions, fibers are only solicited in the first three outer layers of the intervertebral disk.

Table 7 : *Relative anatomic location (anterior, posterior, right and left) of the solicited disk fibers and percentage of solicited fibers in each disk layer in % related to other layers as explained in Figure 2.*

	Flexion	Extension	Right Axial Rotation	Left Axial Rotation	Right Lateral Bending	Left Lateral Bending
Anterior	0	100	42	67	0	31
Posterior	75	0	0	0	8	8
Right	6	0	25	8	8	62
Left	19	0	33	25	84	0
1st layer	56	50	67	50	42	46
2nd layer	25	50	33	33	42	46
3rd layer	19	0	0	17	16	8
4th layer	0	0	0	0	0	0
5th layer	0	0	0	0	0	0
6th layer	0	0	0	0	0	0

Discussion

Despite the advanced age of our anatomical specimen, the principal flexibility curves and coupled motions measured experimentally in flexion-extension, axial rotation and lateral bending are consistent with previous experimental data²⁵ obtained on younger human lumbo-sacral specimens. These data are also obtained on a fully unconstrained mechanical set-up and they might therefore be directly compared to our results.

For the flexion-extension movement, reasonable correlations in the flexibility curves of the segment are found between numerical and experimental results (Figure 4). Coupled motions and translations are similar. Non-linearity is accounted for, thanks to the hyperelastic constitutive law of the disk and of the non-linear springs used for modeling ligaments and disk fibers. However, neutral zone and stiffness at large torques (5-10 Nm) are not large enough in flexion to fit the experimental results perfectly. This is due to the polynomial hyperelastic law, which shows some limitations: this law is not able to describe a weak stress for a large range of strain around the relaxed configuration. The cancellous and cortical bones are subjected to the highest stresses in the flexion movement. Cortical bone Von Mises equivalent stress is lower than 24 MPa, and cancellous bone Von Mises equivalent stress does not exceed 0.5 MPa, which is substantially lower than their corresponding failure strength²⁶.

For the bilateral axial rotation movement, good correlations in the flexibility curves of the segment are also found between numerical and experimental results (Figure 5). Coupled motions and translations are also similar. The neutral zone amplitude is small, as the facets surfaces touch each others at the beginning of the motion. Indeed, this type of motion is blocked by the facets, which geometry does not allow large axial rotation. In right axial rotation, coupled motions in the flexion-extension direction begin at low torque in extension and end at high torque in flexion. This behavior was already observed by Panjabi et al.²⁵ Surprisingly, this effect is not seen in left axial rotation. The cause of this effect remains unclear, but is probably associated with the facet asymmetry. A pronounced coupled motion in right lateral bending is observed in right axial rotation, while an important left lateral bending coupled motion is found in left axial rotation. For this motion, a flexion coupled motion as large as the main motion is also observed (Figure 5).

As for previous motions, good correlations in the flexibility curves of the segment are found between numerical and experimental results for the bilateral lateral bending motion (Figure 6). Non-linearity is also well modeled. However, the neutral zone is not large enough in right lateral bending to fit well experimental results. Coupled motions and translations of the right lateral bending are also similar. Furthermore, these results are also close to those

found by Panjabi et al.²⁵ The left lateral bending coupled motions are different of the right motion. Coupled motions are oscillatory in the experimental results and almost nonexistent in the numerical results. The coupled motions behavior shows that our model is sensitive to this phenomenon, but no explanation is available.

Facets joints do not seem to play a major role in the main motion for flexion-extension and for bilateral lateral bending. In order to understand their role and the origin of the coupled motions, a finite element analysis was conducted with the same model and the same boundary conditions, but with the successive removal of facets joints, ligaments and disk fibers. They were all removed because they could constitute a source of coupling in the model. Only the bilateral lateral bending was studied with these new conditions. The obtained kinematics is shown on Figure 11. Main motion of segment without facets joints, ligaments and disk fibers is obviously softer than the original one. In the domain of stability of the polynomial hyperelastic constitutive law (angle $<6^{\circ}$ in left lateral bending and angle $<5^{\circ}$ in right lateral bending), coupled motions still occur, and even with larger amplitude. Thus, coupled motions for bilateral lateral bending are a consequence of the disk geometry, and probably on the initial center of rotation position.

The strange coupled motions observed in right lateral bending are not due to the geometry of the disk, but probably to the geometry of the facet joints. Indeed, this simulation of the right lateral bending without facets joints, ligaments and disk fibers shows “normal” coupled motion. Therefore, for this particular case, coupled motions are blocked by the right facet joint.

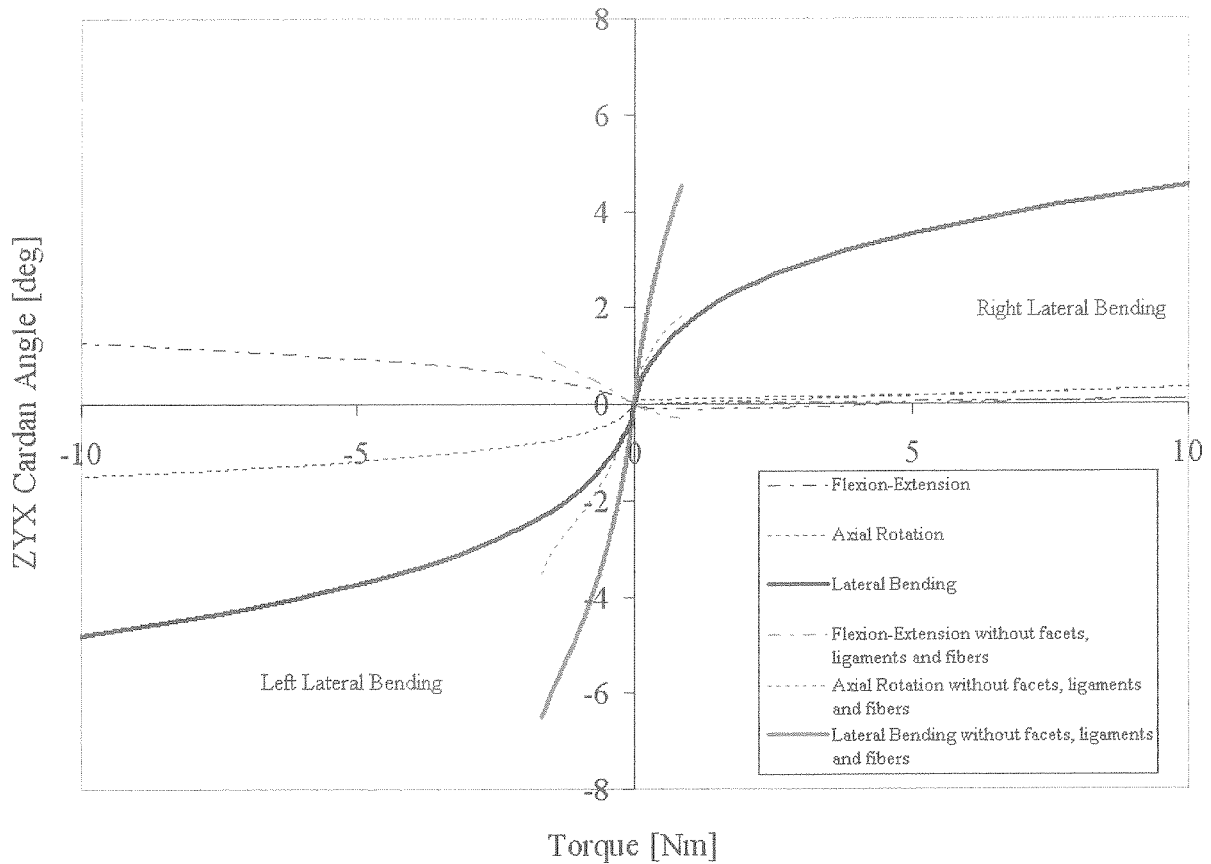


Figure 11 : Bilateral lateral bending kinematics of the « intact » segment and of the segment without facets joints, ligaments and disk fibers.

Several assumptions and limitations are applicable to this model. Accuracy of the cartilage surface, ligament insertion and dimensions is difficult to obtain. Indeed, the cartilage surfaces are reconstructed manually and their thicknesses are kept constant. It is also difficult to measure a precise ligament insertion. The ligaments properties were selected from the literature. For some ligaments (e.g. capsular ligament), it is very difficult to obtain accurate and representative data and dispersion of their material properties is large. In our case, it seems that stiffness of ligaments at high torque is not large enough to better fit the experimental results. The linearity assumption of the cartilage and bone constitutive behavior might also generate errors on the stress-strain distribution in these tissues. The hyperelastic law of the ground substance has some limitations too. It is not possible to treat the tensile and compressive region independently. Furthermore, this law is not able to describe a weak stress for a large range of strain around the relaxed configuration. This limitation explains that the obtained numerical main motions do not possess a large neutral zone. A solution would be to develop a new constitutive law of the ground substance. Despite these disadvantages, this law seems to be appropriate for a first approximation of the kinematics of L5-S1 segments. Boundary conditions applied to the model correspond to the *in vitro* biomechanical tests. No

axial load and no muscles are used in this model. Furthermore, the tests are quasi-static, which is not the case *in vivo*, and the segment is not necessarily representative of all L5-S1 FSUs.

Nevertheless, this model is able to reproduce the compliance of a particular L5-S1 FSU. To our knowledge, it is one of the first time that a numerical model of L5-S1 is validated with experimental results obtained on the same segment for the three major motions. Furthermore, it allows to evaluate the stresses in cartilage, intervertebral disk and ligaments. The role of the facet joints is found to be only important in the axial rotation movement. For the other motions, facet joints might affect the coupled motions in particular case. However, in flexion-extension and in lateral bending, main flexibility curves and coupled motions are mainly dominated by the constitutive law and the geometry of the intervertebral disk. This is in accordance with results obtained by Rao and Dumas²⁷: material properties of the intervertebral ground substance have an important role in the prediction of the biomechanical response of the segment. Thus, an appropriate modeling of the disk geometry and constitutive law is necessary to obtain accurate biomechanical data.

This model is now validated by experimental data, and can therefore be used to analyze the effect of various surgical interventions on joint compliance and stresses inside the tissues of L5-S1 FSU submitted to various surgical interventions.

References

- 1 Ahmed AM, Duncan NA, Burke DL. The effect of facet geometry on the axial torque-rotation response of lumbar motion segments. *Spine* 1990;15:391-401.
- 2 Asazuma T, Stokes IAF, Moreland MS, et al. Intersegmental spinal flexibility with lumbosacral instrumentation: An *in vitro* biomechanical investigation. *Spine* 1990;15:1153-8.
- 3 Goel VK, Wilder DG, Pope MH, et al. Controversy : Biomechanical testing of the spine. Load-controlled versus displacement-controlled analysis. *Spine* 1995;20(21):2354-7.
- 4 Grassmann S, Oxland TR, Gerich U, et al. Constrained testing conditions affect the axial rotation response of the lumbar functional spinal units. *Spine* 1998;23:1155-62.
- 5 Charriere E, Beutler T, Caride M, Mordasini P, Orr TE, Zysset PK. Compliance of the L5-S1 spinal unit: a comparative study between an unconstrained and a semi-constrained system. Submitted to *Spine*.
- 6 Goel VK, Kim YE, Lim TH, Weinstein JN. An analytical investigation of the mechanics of spinal instrumentation. *Spine* 1988;13(9) :1003-1011.
- 7 Kim YE, Goel VK, Weinstein JN, Lim TH. Effects of disc degeneration at one level on the adjacent level in axial model. *Spine* 1991;16:331-335.
- 8 Kong WZ, Goel VK, Gilbertson LG, Weinstein JN. Effects of muscle dysfunction on lumbar spine mechanics. A finite element study based on a two motion segments model. *Spine* 1996;21(19):2197-206.
- 9 Lavaste F, Skalli W, Robin S, Roy-Camille R, Mazel C. Three-dimensional geometrical and mechanical modeling of the lumbar spine. *J. Biomech.* 1992;25:1153-1164.
- 10 Robin A, Skalli W, Lavaste F. Influence of geometrical factors on the behaviour of lumbar spine segments : a finite element analysis. *Eur. Spine J.* 1994;3:84-90.
- 11 Gilbertson LG, Goel VK, Kong WZ, Clausen JD. Finite element methods in spine biomechanics research. *Critical reviews in Biomedical Engineering*, 1995 ;23(5&6) :411-473.
- 12 Swanepoel MW, Cartilage stiffness, morphology and degeneration of the human lumbar apophyseal joints, PhD thesis, Dept of Clinical Medicine, University of Leeds, 1993.
- 13 Lotz JC, Colliou OK, Chin JR, Duncan NA, Liebenberg E. Compression-induced degeneration of the intervertebral disc: an *in vivo* mouse model and finite-element study. *Spine* 1998;23(23):2493-506.
- 14 Sotz MS, Ateshian GA. A conewise linear elasticity mixture model for the analysis of tension-compression nonlinearity in articular cartilage. *J. Biomech. Eng.* 2000 ;122 :1-11.
- 15 Setton LA. Effects of intrinsic viscoelasticity and ion-induced swelling on the mechanical behavior of articular cartilage : theory and experiments. PhD Thesis. 1993 Columbia University.
- 16 Cowin SC. Bone Poroelasticity. *J. Biomech.* 1999 ;32 :217-238.
- 17 Wirtz DC, Shiffers N, Pandorf T, Radermacher K, Weichert D, Forst R. Critical evaluation of known bone material properties to realize anisotropic FE-simulation of the proximal femur. *Journal of Biomechanics* 2000;33(10);1325-1330.
- 18 Suwito W, Keller TS, Basu PK, Weisberger AM, Strauss AM, Spengler DM. Geometric and Material Property Study of the Human Lumbar Spine Using the Finite Element Method. *Journal of the spinal Disorders* 1992; 5-1: 50-59.
- 19 Mow VC, Ratcliffe A, Woos LY, *Biomechanics of Diarthrodial Joints* 1990 ;1

- 20 Cassidy JJ, Hiltner A, Baer E. Hierarchical structure of the intervertebral disc. *Connective Tissue Research* 1989;23:75-88.
- 21 Abaqus/standard 5.8 theory manual and volume I. Hibbitt, Karlsson, Sorensen, Inc. 1998.
- 22 Shirazi-Adl SA. Nonlinear response analysis of the ligamentous lumbar spine in compression, on mechanisms affecting the postural stability. *Spine* 1993 ;18 :147-158.
- 23 Goel VK, Monroe BT, Gilbertson LG, Brinckmann P. Interlaminar shear stresses and laminae separation in a disc : finite element analysis of the L3-L4 motion segment subjected to axial compressive loads. *Spine* 1995 ;20 :689-698.
- 24 Goel K Ramirez SA, Kong W, Gilbertson LG, – Cancellous Bone Young's Modulus Variation Within the Vertebral Body of a Ligamentous Lumbar Spine-Application of Bone Adaptative Remodeling Concepts. *Transactions of the ASME* 1995 ;117: 266-271.
- 25 Panjabi MM, Brand RM, White AA. Three-dimensional flexibility and stiffness properties of the human thoracic spine. *J. Biomech* 1976;9:185-192.
- 26 Cowin SC. *Bone mechanics*. Florida: CRC Press, 1991.
- 27 Rao AA, Dumas GA. Influence of material properties on the mechanical behaviour of the L5-S1 intervertebral disc in compression : a nonlinear finite element study. *J. Biomed. Eng.* 1991 ;13 :139-151.

ABSTRACT

In a first step, the global and the five specific objectives of this thesis are recalled and the major results of each chapter are summarized.

In a second step, in order to address the main hypothesis of this thesis, the validated finite element model is applied to assess the mechanical behavior of the L5-S1 functional spinal unit in presence of an ALIF implant made of hydroxyapatite with controlled macroporosity. A flexion loading case is simulated with and without posterior stabilization. The stresses generated in the implant and the vertebral bodies are calculated for both cases. The implant alone reduces significantly the neutral zone as well as the joint compliance. However, the high stresses generated within the implant prevent its use for a standalone ALIF, as it cannot resist a flexion torque of 10 Nm. Adding a posterior stabilization decreases the neutral zone and joint compliance even further. In this case, the macroporous implant resists the stresses applied by a flexion torque of 10 Nm.

The global objective of this thesis was to develop an alternative for the metallic cage and the bone graft of an ALIF implant. In order to address the relevant issues of this objective, five studies were undertaken:

- An anthropometric study of the L5-S1 segment and the available space for insertion of an ALIF implant under less-invasive conditions (Chapter 2).
- A complete mechanical characterization of two phosphocalcic cements (Chapter 3).
- A new method to manufacture hydroxyapatite scaffolds with controlled porosity (Chapter 4).
- A comparison between an unconstrained and a partially constrained system for *in vitro* biomechanical testing of the L5-S1 functional spinal unit (Chapter 5).
- A numerical study using a finite element model of the L5-S1 functional spinal unit, validated with experimental data (Chapter 6).

The specific objectives of each chapter are recalled and the main results obtained are now summarized.

Chapter 2: Anatomy and anthropometry of the lumbo-sacral segment: an estimation of the available space for the insertion of a fusion cage

One of the purposes of this work was to determine all geometrical parameters that are needed when designing ALIF cages. For a less-invasive surgical procedure, the largest cage for its insertion should have a relative width compared to the endplate width of 66% and a relative depth of 73%, no matter what the sex of the patient is. The implant area which is in contact with the endplate should cover 60% of the total endplate area.

Our study provides the necessary values for the design of an ALIF cage to treat patients with low back pain. Although the number of specimens was low compared to other studies, our data was representative of other studies. It would be necessary in future work to complete these series in order to improve the statistical analysis. In this study, estimated dimensions of an ALIF cage were related to surgeons' know-how.

Chapitre 3: Exhaustive mechanical characterization of brushite and hydroxyapatite cements

Compression, tension and torsion tests together with the use of a conewise linear elasticity model and a Tsai-Wu failure criterion provide an exhaustive characterization of both elastic and failure properties of a brushite and a hydroxyapatite cement. In particular, their

elastic behavior and failure may be simulated by numerical analysis for various physiological loading conditions. Besides, it was confirmed in this study that the hydroxyapatite cement has a higher potential for weight-bearing functions than brushite.

However, as the mechanical properties of these cements degrade over time in a physiological environment, the inclusion of a controlled macroporosity that allows for early colonization by osteoprogenitor cells may be a suitable strategy for specific clinical applications. Promising cements with controlled macroporosity structures shall be characterized by the presented elasticity and failure assessment method in future studies.

Chapter 4: Hydroxyapatite cement scaffolds with controlled macroporosity: fabrication protocol and mechanical properties

Precipitated hydroxyapatite cement scaffolds with macroporosity of controlled size and shape were successfully built using a solid freeform fabrication process. Compression, tension and torsion tests were completed successfully on the precipitated macroporous hydroxyapatite cement samples in moist conditions. Homogenization theory was applied to estimate the elastic properties of the manufactured scaffolds. A good correlation was obtained between experimental and theoretical data.

A new method to manufacture hydroxyapatite scaffolds with controlled porosity and predictable elastic properties was developed. Since precipitated hydroxyapatite cements are biocompatible, biodegradable and osteoconductive, the manufactured scaffolds represent an appropriate biomaterial for bone reconstruction in weight bearing areas dominated by compressive stresses. Further studies will focus on their behavior *in vivo* and at finding new strategies to enhance their tensile and shear strength.

Chapter 5: Compliance of the L5-S1 spinal unit: a comparative study between an unconstrained and a semi-constrained system

A comparison between an unconstrained and a partially constrained system for *in vitro* biomechanical testing of the L5-S1 spinal unit was conducted. The obtained kinematics on both systems were not equivalent, except for the flexion-extension case, where both motions were similar. The directions of coupled motions were similar for both tests, but their magnitudes were smaller in the semi-constrained configuration. The use of a semi-constrained system to characterize lateral bending and axial rotation of the lumbosacral FSU decreased significantly the measured stiffness of the segment.

According to our findings, particular care should be given when quantifying and comparing the compliance of the intact or instrumented spine with experimental set-ups of various degrees of constraints for axial rotation and to an even larger extent for lateral bending. The obtained kinematics on both systems is not equivalent, i.e. the segment does not follow the same pathway to the equilibrium positions, except for the flexion-extension case, where both motions are similar. Furthermore, as *in vivo* boundary conditions are mixed conditions (i.e. torques and forces, rotations and translations are simultaneously imposed to various parts of the segment) that are not well identified, it remains difficult to impose realistic boundary conditions to the segment *in vitro*.

Chapter 6: A finite element model of the L5-S1 functional spinal unit: development and comparison with biomechanical tests *in vitro*

A three-dimensional finite element model of the L5-S1 FSU was developed. Flexion-extension, axial rotation, and lateral bending torques were applied to the specimen. A comparison with the experimental results obtained on the same segment for these three major motions was then conducted.

The compliance of the segment were found to be similar between numerical and experimental results for all major motions. Coupled motions and translations were also similar, even in their amplitude. Most of the ligaments were active in flexion and extension. The role of the facet joints was found to be essential in axial rotation. For the other motions, facet joints did affect the coupled motions in particular cases. However, in flexion-extension and in lateral bending, the flexibility curves and the coupled motions were dominated by the geometry and the constitutive law of the intervertebral disk. This model was validated by experimental data, and can therefore be used to analyze the effect on joint compliance and the tissue stresses of an L5-S1 FSU subjected to various surgical interventions. Improvement of the constitutive law of the intervertebral disk is necessary to obtain a more accurate model.

In order to address the global hypothesis of this thesis, the validated finite element model of the L5-S1 functional spinal unit (presented in chapter 6 and validated with results of chapter 5) was used with an implant made of macroporous hydroxyapatite inserted between the two endplates.

This implant (Figure 1) was designed according to the results obtained in chapter 2 (anthropometry). It had a relative width compared to the endplate width of 66% and a relative

depth of 73%. The implant area which is in contact with the endplate covers 60% of the total endplate area.

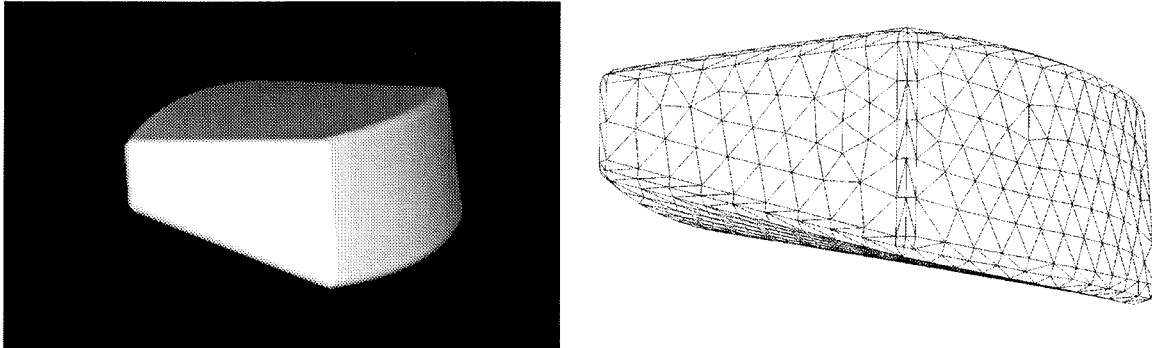


Figure 1: Custom anterior L5-S1 interbody fusion implant. Design and finite element mesh (3500 linear elements).

The constitutive laws of the different tissues used in this model are the same as those used in chapter 6. The implant is made of a hydroxyapatite scaffold. Thus, material properties of such scaffold presented in chapter 4 were used as material properties of this modeled implant. Contact between the two endplates and the implant was tied.

For the first numerical analysis, a flexion torque (along the transversal axe) was applied with the macroporous hydroxyapatite implant inserted with an ALIF approach. An alternative of this anterior approach would be to add a posterior stabilization to the segment (Chapter 1). For this second numerical analysis, the posterior stabilization was simulated by locking the two facet joint contact zones together. These two numerical models intended to examine the effect of this implant (and the implant + posterior stabilization) on the compliance of the L5-S1 segment and to estimate the stresses in the implant and vertebral bodies for a “standard” 10 Nm applied torque in the unconstrained configuration (see chapter 5 and 6 for further explanations).

The obtained compliance curves are shown on Figure 2 where main motions of the “intact” segment, segment with the new ALIF implant and segment with the new ALIF implant and a posterior stabilization are plotted. Principal stresses occurring in the hydroxyapatite implant are presented in Figure 3 for a two-dimensional stress state, with and without posterior stabilization. They are compared to the Tsai-Wu failure criterion of the macroporous hydroxyapatite scaffold (see chapter 3 for the criterion and chapter 4 for experimental data used with this criterion). Histograms of the Tsai-Wu function values for all elements in the implant, with and without the posterior stabilization, are presented in Figure 4. If the Tsai-Wu function value is larger than one for an element, it means that too much stress is applied to it, and thus that it will break. Finally, a three-dimensional view of the obtained Von Mises equivalent stress distribution in the implant is shown on Figure 5 for both cases.

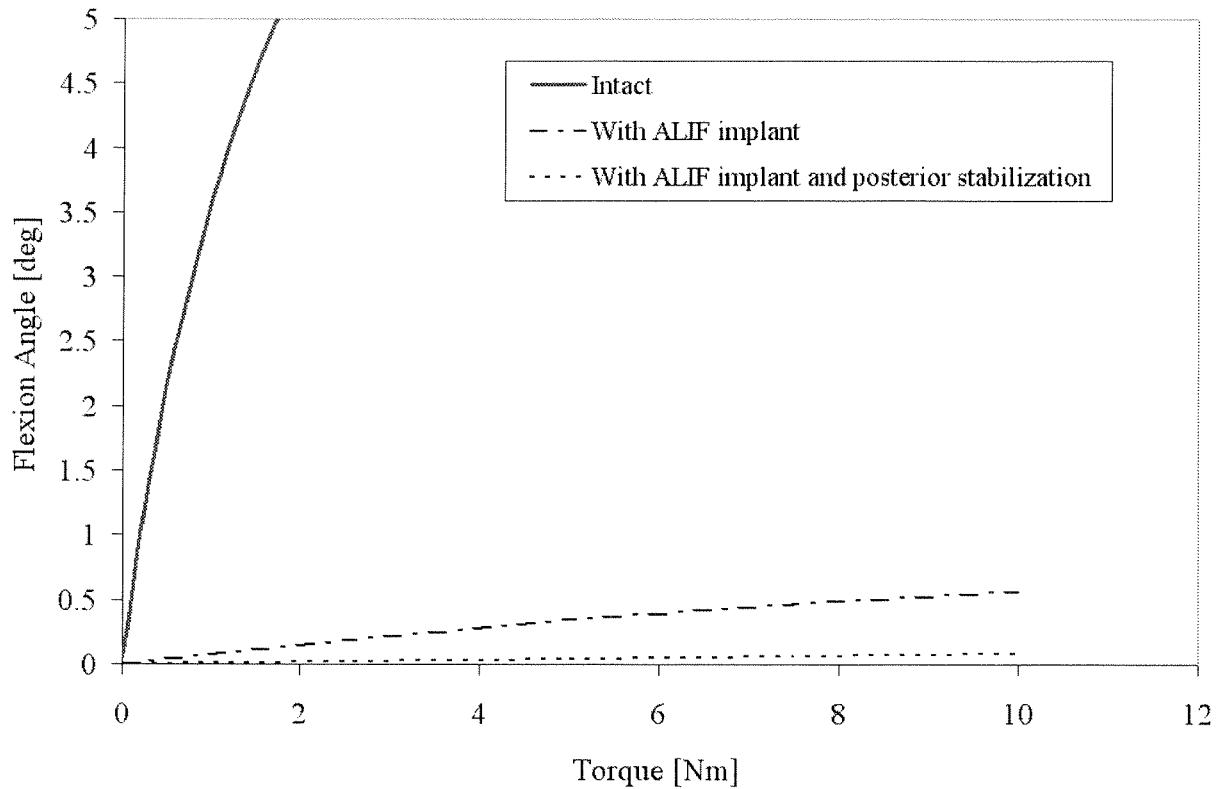


Figure 2 : Flexion of the L5-S1 segment, intact, with the ALIF implant, and with the ALIF implant and a posterior stabilization.

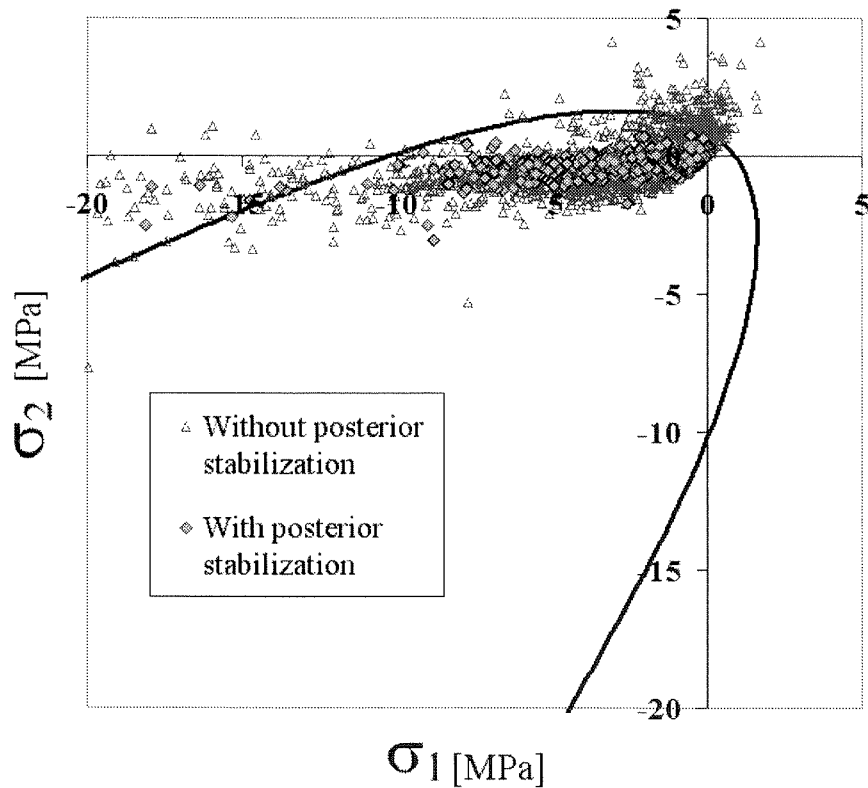


Figure 3 : Principal stresses in the implant, with and without posterior stabilization for a 10 Nm flexion torque. Each point corresponds to an element of the discretized implant. The black curve is the Tsai-Wu criterion of the macroporous hydroxyapatite scaffold for a two-dimensional stress state.

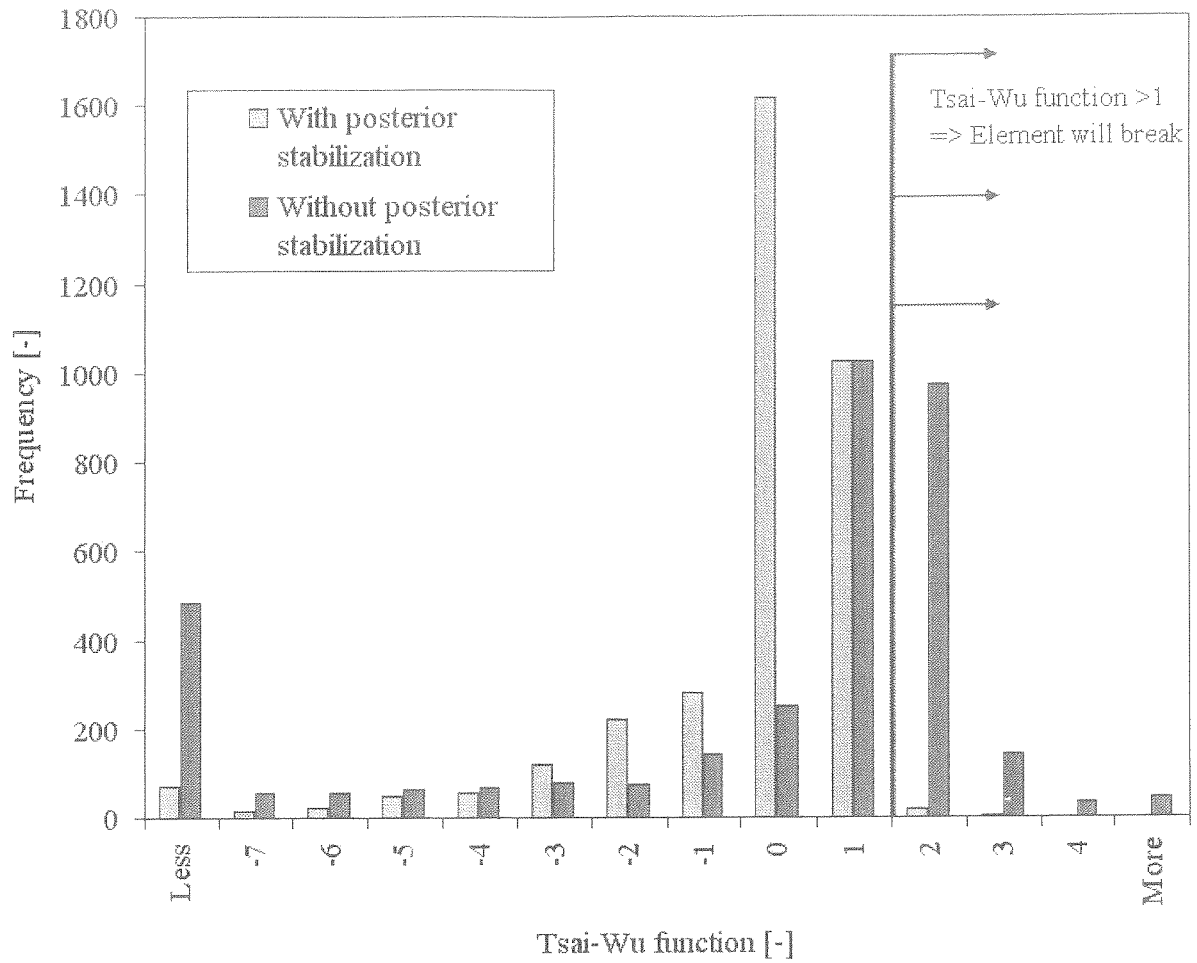


Figure 4 : Histograms of the Tsai-Wu function values for all elements in the implant, with and without the posterior stabilization for a 10 Nm flexion torque. If the Tsai-Wu function value is larger than one for an element, it means that too much stress is applied to it, and thus that it will break.

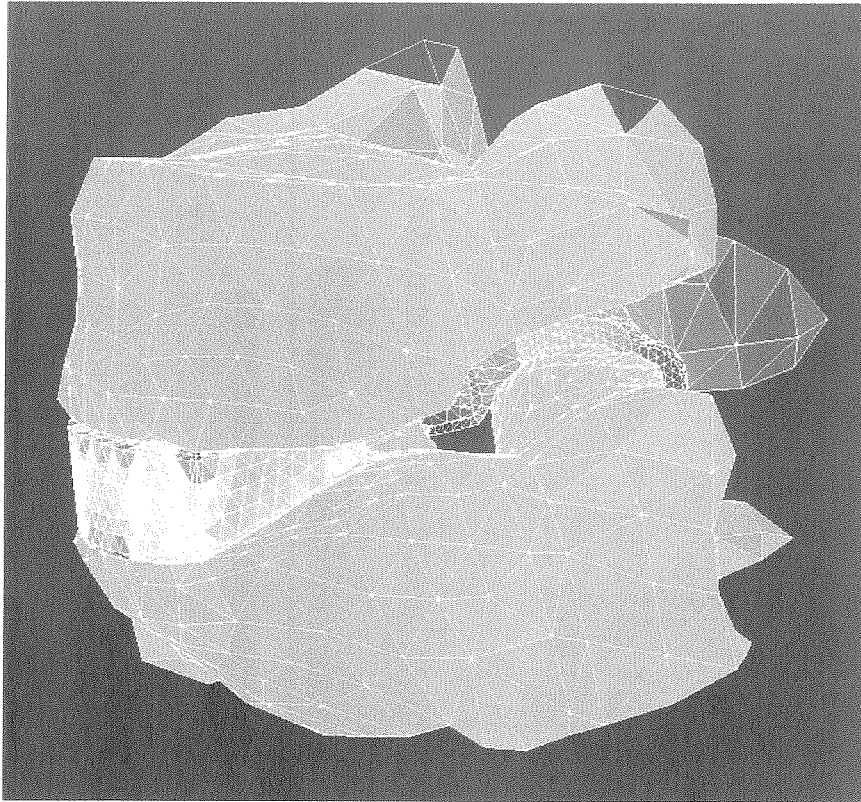
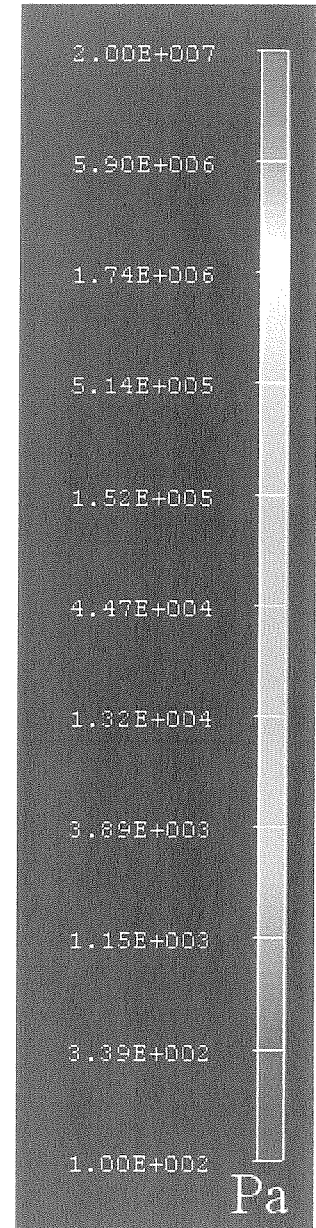
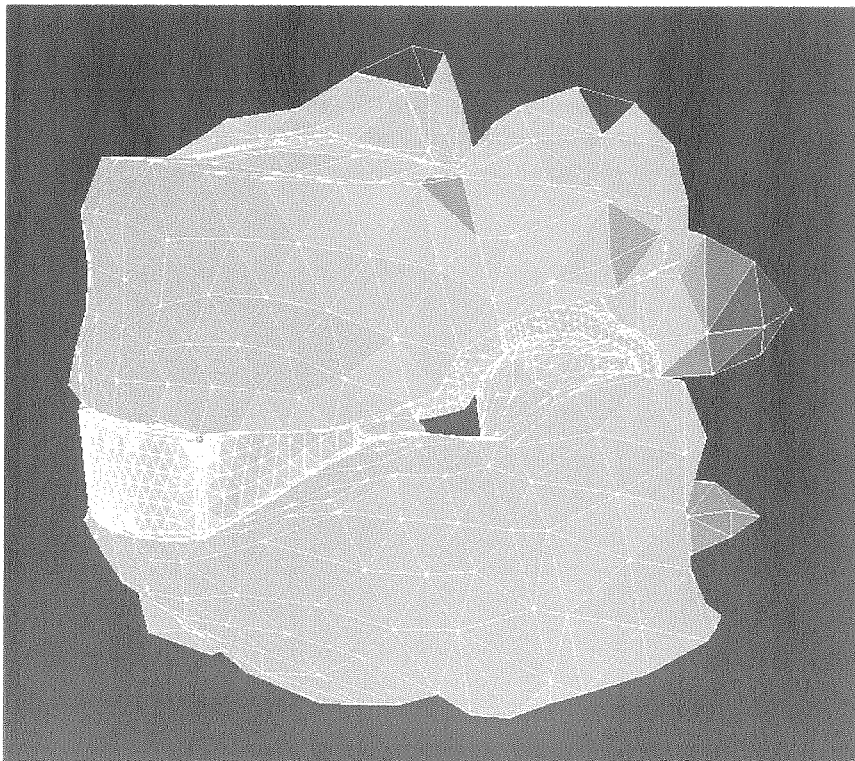
ALIF implant*ALIF implant and posterior stabilization*

Figure 5: Von Mises stresses distribution in the L5-S1 segment, with an ALIF with and without posterior stabilization.

The implant significantly reduces the neutral zone of the segment and its compliance (Figure 2). The ZYX Cardan rotation angle is decreased by a factor of twenty. However, there is still a 0.56° total ZYX Cardan rotation between the two vertebrae. 26% of the implant elements are submitted to multiaxial stresses larger than the hydroxyapatite scaffold multiaxial strength (Figure 3 and Figure 4). Most of them are concentrated in the anterior zone of the implant (Figure 5). **Therefore, this macroporous hydroxyapatite implant alone will not resist a flexion torque of 10 Nm applied to the L5-S1 FSU.** Since two of our specimens broke during the in-vitro tests at 10 Nm, this torque seems to be a higher boundary of torque that could be *felt* by the L5-S1 segment *in vivo*. The maximum Von Mises equivalent stress in the cancellous bone structure is 0.7 MPa, which is approximately ten times lower than the ultimate strength of this tissue (see Chapter 4 for references). Thus, no failure will occur in the L5-S1 cancellous bone.

Considering the ALIF implant together with a posterior stabilization, the decrease of the neutral zone and the compliance is even sharper. Indeed, the ZYX Cardan rotation angle decreased to 0.08° (Figure 2), which is seven times lower than the angle obtained with only the implant and hundred-forty times lower than the angle obtained on the “intact” functional spinal unit. The multiaxial stresses inside the implant are also lowered. With the posterior stabilization, only 0.7% of the implant elements are submitted to multiaxial stresses larger than the hydroxyapatite scaffold multiaxial strength (Figure 3 and Figure 4). They are all located in the anterior part of the junction between the implant and the two endplates. **Therefore, this macroporous hydroxyapatite implant with a posterior stabilization will resist a flexion torque of 10 Nm applied to the L5-S1 FSU.** The maximum Von Mises equivalent stress in the cancellous bone structure is 0.2 MPa, which is approximately thirty times lower than the ultimate strength of this structure (see Chapter 4). Thus, no failure will occur in the L5-S1 cancellous bone.

This analysis represents an attempt to quantify the stress distribution in the implant with or without a posterior stabilization for a rather extreme flexion torque of 10 Nm. Some limitations of this evaluation can be pointed out. Boundary conditions applied to the model correspond to the *in vitro* situation of the specimen tested in the laboratory. No axial load and no muscle forces were used in this model. Furthermore, the tests were quasi-static, which is obviously not the case *in vivo*, and the individual segment used is not necessarily representative of all L5-S1 FSUs. The contact between the implant and the subchondral bone was idealized; a perfect anchorage of the implant in the subchondral endplate was assumed, which is probably not the case after its surgical insertion. The choice of the posterior

stabilization was also idealized. The facet joints contact zones were locked together, assuming a *perfect* posterior stabilization. Furthermore, increase of the local stresses in the posterior elements due to the insertion of screws in the facet joints were not computed with our model.

Is this implant really suited for an ALIF procedure? The macroporous hydroxyapatite implant alone will not support the applied stresses, because the tensile mechanical strength of this scaffold is rather low. However, if a posterior stabilization is added, the implant will be strong enough to support the submitted stresses. In a physiological environment, fatigue and resorption of the hydroxyapatite macroporous scaffold phenomena are expected to be compensated by bone formation. *In vivo* studies will have to be conducted in order to measure the hydroxyapatite scaffold resorption rate and fatigue behavior in a physiological environment, as well as to determine the rate of bone formation.

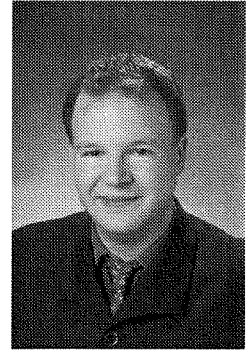
We demonstrated in this work the possibility to manufacture hydroxyapatite scaffold with controlled macroporosity. The outer design of the implant, as well as the inner distribution and size of the macroporosity, can be selected. Thus, implants for numerous applications in orthopaedic or maxillo-facial surgery could be designed and manufactured with the proposed technique. However, in order to use such implants as a standalone ALIF solution, the biomaterial must be improved. A potential solution would be to add fibers (like for instance collagen fibers in bone) to this material in order to improve its tensile strength.

Based on the present thesis, two alternatives to current ALIF procedures can be proposed. First, this macroporous scaffold can be used as an ALIF implant, in conjunction with a posterior stabilization. The main advantages compared to current solutions are: a) no more bone graft is necessary and b) no more metal is inserted anteriorly. Second, this macroporous scaffold can be used as a bone graft material, which could be inserted in cages with controlled elasticity. As the elasticity of these macroporous scaffolds can also be controlled, bone formation could be enhanced. Then the main advantage compared to current solutions is to avoid harvesting of the bone graft. These two options can be proposed today as an alternative to current ALIF, waiting for the ideal replacement of the complete intervertebral disk, preserving segment mobility and therefore the adjacent segments. As a next step, these alternatives based on biomaterial and biomechanical arguments will have to be evaluated on biological grounds using an animal model.

Eric CHARRIERE

Biomedical & Materials Science EPF Engineer

Les Bosquets de Paudille 5
1803 Chardonne
076/389'56'54
Swiss, 29 years old
eric.charriere@urbanet.ch



Education

- Since 1998** **PhD Student, Mechanical Department, Swiss Federal Institute of Technology (EPFL, Lausanne) and “Hôpital Orthopédique de la Suisse Romande” : A calcium phosphate implant with controlled macroporosity for anterior L5-S1 interbody fusion.**
- 1997** Master Diploma in **Biomedical Engineering** at the EPFL and University of Lausanne
- 1997** Diploma in **Materials Science**, EPFL
- 1992** Scientist General Certificate of Education, Bulle

Award

- 2000** S.L. Koch award for the paper with the greatest future clinical application to the practice of hand surgery (American Society of Surgery of the Hand annual meeting, Seattle)

Publications

JOURNAL ARTICLES

- 1. Charrière E., Lemaître J., Zysset P.K.**
Design and manufacturing of Hap cement scaffolds with controlled porosity: prediction of elastic properties and fabrication protocol.
Submitted to Biomaterials.
- 2. Charrière E., Beutler T., Caride M., Mordasini P., Orr T.E., Zysset P.K.**
Compliance of the L5-S1 spinal unit: a comparative study between an unconstrained and a semi-constrained system.
Submitted to Spine.
- 3. Charrière E., Terrazzoni S., Pittet C., Mordasini P., Dutoit M., Lemaître J., Zysset P.K.**
Mechanical characterization of brushite and hydroxyapatite cements.
Biomaterials 2001;22(21):2937-2945.

CONFERENCE PROCEEDINGS AND/OR ABSTRACTS

1. **Kombot C., Siegriest O., Caride M., Charrière E., Zysset Ph.**
Reconstruction du ligament croisé antérieur : Etude biomécanique de la fixation d'un tendon dans un tunnel osseux par vis d'interférence biorésorbable
61^{ème} congrès annuel de la Société Suisse d'Orthopédie, Lugano, Suisse, 23-25 août 2001, IR 16 (oral presentation).
2. **Charrière E., Beutler T., Caride M., Mordasini P., Dutoit M., Orr T.E., Zysset P.K.**
Mobility of the L5-S1 spinal unit : a comparative study between an unconstrained and a semi-constrained system
47th annual meeting Orthopaedic Research Society, San Francisco, February 25-28 2001 (poster).
3. **Papaloïzos M., Cuénod Ph., Charrière E.**
Etude expérimentale de la résistance mécanique de deux autogreffes du poignet pour le remplacement de la composante dorsale du ligament scapholunaire
Congrès Annuel de la Société Suisse de la Main, Lausanne, Suisse, 27-28 octobre 2000 (oral presentation), O 38.
4. **Charrière E., Terrazzoni S., Pittet C., Mordasini P., Dutoit M., Lemaître J., Zysset P.K.**
Mechanical characterization of brushite and hydroxyapatite cements
10th annual meeting European Orthopedic Research Society, Wiesbaden, Germany, October 12-15 2000 (Poster), P 18.
5. **Charrière E., Terrazzoni S., Pittet C., Mordasini P., Dutoit M., Lemaître J., Zysset P.K.**
Exhaustive mechanical characterization of brushite and hydroxyapatite cements
International Workshop on Bone Substitutes, Davos, Switzerland, October 8-10 2000 (Poster), P8.
6. **Ph. Mordasini, E. Charrière, M. Caride, T. Beutler, M. Dutoit, T.E. Orr, Ph. Zysset**
Measure of L5-S1 compliance in vitro: direct comparison between an unconstrained and a partially constrained testing system
60^{ème} congrès annuel de la Société Suisse d'Orthopédie, Davos, Switzerland, September 2000 (oral presentation), IR 21.
7. **Papaloïzos M.Y., Charrière E., Cuenod Ph.**
A mechanical comparison of bone-ligament-bone autografts from the wrist for replacement of the dorsal component of the scapholunate ligament
7th congress of the Federation of the European Societies for Surgery of the Hand, Barcelona, Spain, June 21-24 2000 (oral presentation), O70.
8. **Cuenod Ph., Charrière E., Papaloïzos M.Y.**
A biomechanical comparison of bone-ligament-bone autografts from the wrist for replacement of the dorsal component of the scapholunate ligament
American Society for Surgery of the Hand (annual meeting), Seattle, USA, October 5-7 2000 (oral presentation), O#36a.

9. **Charrière E., Terrazzoni S., Pittet C., Lemaître J., Zysset P.K.**
Mechanical characterization of brushite and hydroxyapatite cements
59^{ème} congrès annuel de la Société Suisse d'Orthopédie, Winterthur, Switzerland, September 1999 (oral presentation).
10. **Charrière E., Zysset P.K.**
Mechanical characterization of biocements
9th European Meeting on Injectable Bone and Joint Substitution Materials, EPFL, Switzerland, March 1999. (Poster).
11. **Charrière E., Rakotomanana L.R., Rubin P.J., Leyvraz P.-F.**
Influence of stem surface roughness on the wear debris generation after cemented hip arthroplasty
Third World Congress of Biomechanics, Sapporo, Japan, August 1998 (oral presentation).
12. **Charrière E., Rakotomanana L.R., Rubin P.J., Leyvraz P.-F.**
Cemented femoral stem after THR: Influence of stress and micromotions on the wear rate and on the deterioration of the stem surface topography
8th annual meeting Eur Orthop Res Soc, Amsterdam 1998 (oral presentation).
13. **Charrière E., Rakotomanana L.R., Rubin P.J., Leyvraz P.-F.**
Wear rate at the cemented bone-implant interfaces: influence of stress, micromotions and stem surface design
3rd combined meeting of the Orthop Res Soc, Hamamatsu, Japan 1998 (oral presentation).
14. **Wojcik Paul T., Charrière E., Orazem Mark E.**
Experimental study of the erosion-corrosion of copper and copper-nickel alloys at the corrosion potential and at anodic potentials
Tri-Service conference on corrosion, Wrightsville Beach, North Carolina, USA 1997.

